Experimental Investigations on the Influence of the Photocathode Laser Pulse Parameters on the Electron Bunch Quality in an RF - Photoelectron Source

Dissertation
zur Erlangung des Doktorgrades
des Departments Physik
der Universität Hamburg

vorgelegt von
Marc Hänel
aus Cottbus

Hamburg
2010

Gutachter der Dissertation:	Prof. Dr. rer. nat. Shaukat Khan Prof. Dr. rer. nat. Jörg Roßbach
Gutachter der Disputation:	Prof. Dr. rer. nat. Shaukat Khan PD Dr. rer. nat. Bernhard Schmidt
Datum der Disputation:	22. Juni 2010
Vorsitzender des Prüfungsausschusses:	Dr. rer. nat. Georg Steinbrück
Vorsitzender des Promotionsausschusses:	Prof. Dr. rer. nat. Jochen Bartels
Leiterin des Departments Physik:	Prof. Dr. rer. nat. Daniela Pfannkuche
Dekan der Fakultät für Mathematik, Informatik und Naturwissenschaften:	Prof. Dr. rer. nat. Heinrich Graener

Kurzdarstellung

Freie Elektronen Laser die nach dem SASE Prinzip arbeiten, wie der European XFEL, benötigen Elektronenpakete mit Spitzenstromstärken von mehreren Kiloampère und geringer transversaler Emittanz. Während die hohen Spitzenströme durch longitudinale Komprimierung der Elektronenpakete erreicht werden kann, muss die transversale Emittanz bereits an der Elektronenquelle Werte von weniger als 1 mm mrad aufweisen. Die Entwicklung von Elektronenquellen, welche diese Spezifikationen erfüllen, ist die Aufgabe des Photoinjektor Teststandes bei DESY in Zeuthen (PITZ).
Kern eines Photoinjektors ist die Elektronenkanone in welcher die Elektronenpakete erzeugt werden und die erste Beschleunigung stattfindet. Die Extraktion der Elektronen von der Katode erfolgt mittels des äußeren lichtelektrischen Effekts, wofür ein Lasersystem benötigt wird, welches speziellen Anforderungen genügen muss. Im ersten Teil dieser Arbeit wird untersucht, ob das Lasersystem und die Laserstrahlführung diese Spezifikationen erfüllen. Im zweiten Teil der Arbeit wird anhand von Simulationen und Experimenten untersucht, welchen Einfluß die zeitlichen und räumlichen Eigenschaften der Laserpulse auf die Qualität der damit erzeugten Elektronenpakete haben. Diese Einflussnahme ist möglich, da die Reaktionszeit der Cs_2Te Katode klein ist im Vergleich zur Dauer der Laserpulse. Davon ausgehend werden Verbesserungsvorschläge und Toleranzen definiert.

Abstract

Free Electron Lasers based on the SASE principle like the European XFEL require electron bunches having peak currents of several kiloamperes as well as very low transverse emittance. While high peak currents can be generated using longitudinal bunch compression techniques, the transverse emittance must have values as low as 1 mm mrad already at the source. The development of electron sources fulfilling these demanding specifications is the goal of the Photo Injector Test Facility (PITZ) in DESY, Zeuthen site.
The key component of a photoinjector is the electron gun cavity where the electrons bunches are generated and immediately accelerated. The extraction of the electrons is based on the photoelectric effect of the cathode which requires a laser system having special capabilities. In the first part of the thesis, measurements are presented which were performed to investigate whether the laser and the laser transport system fulfill these requirements. The second part of the thesis is dedicated to simulations as well as experimental studies on the impact of the temporal and spatial parameters of the laser pulses on the electron bunch quality. This influence is possible because the response time of the Cs_2Te photocathode is short compared to the laser pulse duration. Based on these investigations, suggestions for improvements are given and tolerances for the laser pulse properties are defined.

For my family, Jana and Sontje
Thank you for being part of my life

Contents

Acronyms

ADC	Analog-Digital-Converter
BBO	β-BaB_2O_4, beta-Barium Borate
LBO	LiB_3O_5, Lithium triborate
Nd:YLF	Nd^{3+}:$YLiF_4$, Neodymium doped Yttrium Lithium Fluoride
Yb:KGW	Yb^{3+}:$KGd(WO_4)_2$, Ytterbium doped Potassium Gadolinium Tungstate
Yb:YAG	Yb^{3+}:$Y_3Al_5O_{12}$, Ytterbium doped Yttrium Aluminium Garnet
cw	continuous wave
BSA	Beam Shaping Aperture
OSS	Optical Sampling System
DFG	Difference Frequency Generation
FROG	Frequency Resolved Optical Gating
SHG	Second Harmonic Generation
GRENOUILLE	Grating Eliminated No-nonsense Observation of Ultrafast Incident Laser Light E-fields
TG	Transient Grating

Chapter 1

Introduction

One of the most important tools in natural science research is light. It is used to illuminate objects, investigate materials by measuring their response to light exposure or to intentionally modify matter.
In the early 20^{th} century Albert Einstein proposed the principle of Light Amplification by Stimulated Emission of Radiation (LASER). It was based on the rate equations of photon absorption as well as spontaneous and stimulated emission [Eins]. Desirable properties of the light produced by the proposed sources led to continuous efforts until the year 1960, when Maiman et al. realized the first laser system based on ruby [Maim]. Shortly afterwards, the first nonlinear optical effect (frequency doubling in quartz) could be observed in 1961, thanks to the high intensity of the laser light [Fran]. Ever since, the frontiers of the available laser pulse properties were pushed forward. Nowadays, it is possible to generate light pulses with durations of less than one hundred attoseconds using state-of-the-art laser systems [Goul]. The available wavelengths range from the infrared up to the soft x-ray region. However, hard x-ray radiation is not yet accessible by conventional laser systems.
In the meantime, an alternative way of generating coherent short light pulses emerged. It is based on the idea, that the radiating electrons do not necessarily need to be bound to a nucleus as it is the case for conventional lasers. Instead, the electrons are emitted from a source and accelerated to ultra-relativistic velocities. Subsequently, they pass a magnetic structure with an periodic magnetic field perpendicular to the moving direction of the electrons[1], called undulator (shown in figure 1.1). Due to the Lorentz force, the electrons move on a sinusoidal trajectory and start to emit electromagnetic radiation in the forward direction. This process is called undulator radiation and the emitted wavelength is given by [FEL]

[1]The distance between two pole faces having the same direction of the magnetic field is called undulator period.

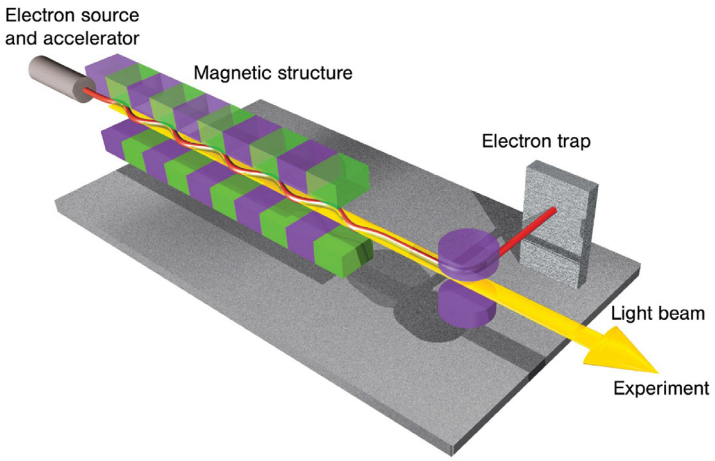

Figure 1.1: *Sketch of the electrons (red) passing the undulator and creating light (yellow) due to the interaction with the magnetic field. Image taken from XFEL homepage: http://www.xfel.eu*

$$\lambda_{und} = \frac{\lambda_u}{2\gamma^2} \cdot \left(1 + \frac{K^2}{2}\right) \quad \text{with} \quad K = \frac{\lambda_u e \tilde{B}}{2\pi m_e c^2}. \tag{1.1}$$

Here, λ_u is the undulator period, $\gamma = (1 - v^2/c^2)^{-1/2}$ is the relativistic Lorentz factor and K is the undulator parameter with e being the electron charge, m_e the electron rest mass and c the speed of light in vacuum. Finally, $\tilde{B}$ is the on axis peak magnetic field which reads for planar sinusoidal undulators $\tilde{B} = B_0/\cosh(\pi \frac{g_u}{\lambda_u})$ with B_0 being the magnetic flux density in the middle of the pole face and g_u the magnet gap height. It can be seen from this equation that the emitted radiation wavelength can be varied by changing either the electron energy (and therefore γ) or the undulator gap height. The second approach has the advantage that an adjustment of the electron optics upstream of the undulator is not required.
In a special case the electrons interact with already existing, co-propagating light of wavelength λ_{und}. Depending on their mutual phase relation, electrons can transfer energy to the light wave or they receive energy. For an electron bunch which is longer than the wavelength of the light, this leads to a longitudinal electron density modulation. The generation of the modulation is called micro-bunching and the spatial separation of the micro-bunches corresponds to the wavelength of the light. For that reason the light amplification is coherent and the gain no longer scales with the number of electrons N_e, as it is the case for the undulator radiation, but with N_e^2 [FEL]. This principle is called *F*ree *E*lectron *L*aser (FEL). The wavelength of the emitted radiation is the same as for the undulator radiation given by equation 1.1.
When the FEL produces x-ray radiation, it is not possible to amplify the generated light

in an optical resonator, because the required optical elements, particularly mirrors with high reflectivity, are not available. Hence, the light must be amplified in a single pass through the undulator. In this case the generation of the light can be subdivided into three steps [FEL]. At start-up, the light is created from shot noise. Afterwards, the electrons resonantly interact with the light leading to an exponential increase of the light intensity. Finally the FEL amplification process saturates. The onset of saturation is the optimum operating point of an FEL. After traveling through the undulator, electron bunches are sent to a beam dump and the light can be delivered to the experimental stations (see figure 1.1). This process of light generation is called Self-Amplified Spontaneous Emission (SASE). The SASE light pulses possess very special properties such as pulse durations in the femtosecond range, high intensities and a high degree of transverse coherence [FEL, Sald02]. The smallest wavelength demonstrated so far is 0.15 nm [SLAC] while peak brilliances larger than $10^{29} \frac{\text{photons}}{\text{s mrad}^2\,\text{mm}^2\,0.1\%\text{BW}}$ [FLASH] for the fundamental wavelength were obtained at FLASH. Future FELs like the XFEL will provide light pulses of even higher quality (see table 1.1).
To achieve these properties, the requirements on the electron bunch quality are very demanding. The minimum achievable wavelength, for example, is proportional to the geometric transverse emittance ε (see chapter 6.1 for the definition of ε) and the energy spread ΔE of the electron bunch [Ros01]

$$\lambda_{min} \cong 18\pi\varepsilon\frac{\Delta E}{E} \cdot \sqrt{\frac{\gamma I_A}{I_p}\frac{1+K^2}{K^2}}. \tag{1.2}$$

In this equation, E is the mean energy of the electron bunch, I_p is the peak current and $I_A = 17\,\text{kA}$ is the Alfvén current. The minimum achievable wavelength scales inversely proportional to the peak current. Conversely, a higher peak current, meaning a larger charge density, causes an increase of the transverse space charge forces and thus a growth of the transverse emittance, which is disadvantageous in terms of low λ_{min}. These considerations show, that a proper choice of the electron bunch properties is influenced by many interdependencies.
Another parameter which characterizes the performance of an FEL is the required undulator length to achieve gain saturation which occurs at approximately twenty times the power gain length L_g [FEL]. The latter one is defined as the length needed to amplify the radiation power by a factor of e. According to [Ferr02], this length is proportional to

$$L_g \propto \frac{\varepsilon_n \cdot \gamma^{3/2}}{K \cdot \sqrt{2I_p(1+K^2/2)}}. \tag{1.3}$$

A reduction of the gain length is an important cost saver since it determines the required undulator length. Therefore, it is preferential to have electron bunches with a low transverse emittance. In table 1.1, the operating parameters are summarized for the currently

Parameter	FLASH (run 2007-2009)	European XFEL
Electron bunch properties		
bunch charge	1 nC	1 nC
energy at undulator	1 GeV	17.5 GeV
peak current	1-2 kA	5 kA
required transv. norm. emittance at undulator	2.0 mm mrad (proj.)	1.4 mm mrad (slice)
Undulator properties		
total undulator length	30 m	165 m
undulator period λ_{und}	27.3 mm	35.6 mm
undulator gap g_{und}	12 mm	10 mm
peak magnetic field	0.47 T	1.0 T
FEL radiation properties		
wavelength range	6.8 - 47 nm	down to 0.1 nm
pulse duration	10 - 70 fs	100 fs
peak power	1 - 5 GW	20 GW
peak brilliance in $\frac{\text{photons}}{\text{s mm}^2\,\text{mrad}^2\,0.1\%\text{BW}}$	10^{29} – 10^{30}	$5.0 \cdot 10^{33}$

Table 1.1: *Operating parameters of FLASH and the future European XFEL [FLASH, XTDR]. Note that the XFEL will have several undulator beamlines. The numbers given here correspond to the minimal achievable wavelength (at SASE1 beamline).*

existing FEL FLASH (*F*reie Electronen *Las*er in *H*amburg) and the future European XFEL (*X*-ray *F*ree *E*lectron *L*aser), both at DESY in Hamburg.
For the successful operation of the European XFEL, a normalized transverse slice emittance of 1.4 mm mrad at the undulator entrance is required [XFEL]. Because the transverse emittance can only degrade during the transport from the electron source to the undulator, the injector part[2] of the accelerator must provide electron bunches with a normalized projected transverse emittance of equal or better than 0.9 mm mrad [XTDR]. The *P*hoto *I*njector *T*est Facility at DESY, *Z*euthen site (PITZ) was established to develop and optimize electron sources to meet the requirements for the future European XFEL [PITZ01].

Part of the optimization of the electron source are investigations of the requirements for the photocathode laser systems, which are developed and built by the collaboration partner Max Born Institute Berlin (MBI). The pulses produced by the laser system are used to extract the electrons from a Cesium Telluride photocathode via the photoelectric effect. Since the response time of the photocathode is believed to be short compared to

[2]The injector is the combination of electron source and first accelerating module.

the laser pulse duration [Suber], the temporal laser pulse profile has a direct impact on the longitudinal electron bunch properties. The same is true for the transverse shape of the laser pulses, which is translated to the initial transverse charge density distribution of the electron bunch.
In this work, the relations between the photocathode laser pulse parameters and the resulting electron bunch properties are investigated experimentally. After an introduction to the PITZ setup, the laser system, the laser transport system (laser beamline) and the available laser pulse diagnostics are presented. This is followed in chapter 4 by the experimental characterization of the emitted laser pulses as well as the laser beam transport system. Since a large part of the transverse emittance budget originates from the generation of the electron bunch, the process of electron emission from a photocathode is introduced in detail in chapter 5. This is followed in chapter 6 by the presentation of the beam dynamics which takes place after the emission.In chapter 7, the relations between laser pulse parameters and the electron bunch properties will be investigated by simulations and compared with measurements.

Chapter 2

PITZ - an overview

The Photoinjector Test Facility at DESY in Zeuthen (PITZ) is a test bench for the development and optimization of photo-injector components which are planned to be installed at FLASH and the future European XFEL. The main goal is to produce electron bunches with 1 nC charge having a normalized projected transverse emittance of not more than $\varepsilon_n = 0.9\,\text{mm·mrad}$ at the injector output. All major components which have an influence on the transverse emittance like the gun cavity or the laser system as well as the available diagnostics are continuously improved and investigated.
In the following sub-chapters, the machine setup which has been used for the experimental investigations is introduced. At first, the sub-components associated with the acceleration of the electron bunches will be described. These are the electron gun and the booster cavity together with the solenoid magnets which are used for focusing and compensation of the space charge induced emittance growth. Secondly, the available electron bunch diagnostics will be summarized.

2.1 Electron bunch acceleration and focusing

At PITZ, two accelerating RF cavities are used, both operated at a frequency of 1.3 GHz (L-band). The electron gun cavity is a 1.6-cell copper cavity, which has a field balance[1] of 1.05 (gun 4.2) and a maximum electric field[2] at the cathode of about 60 MV/m. The cathode material is Cs_2Te grown as a thin layer on a Molybdenium plug that can be inserted from the back of the electron gun cavity. In figure 2.1, the gun cavity including the solenoids is depicted. The maximum mean momentum after the gun is about 6.8 MeV/c [Roen].

[1]The field balance is defined as the ratio of the maximum electric field amplitude in the half-cell compared to the full cell, see also Fig.2.2 (blue curve)

[2]The electric field strength is defined as the local gradient of the electric potential $\vec{E}(x,y,z) = \text{grad}\, U(x,y,z)$ and the term *gradient* is used synonymously

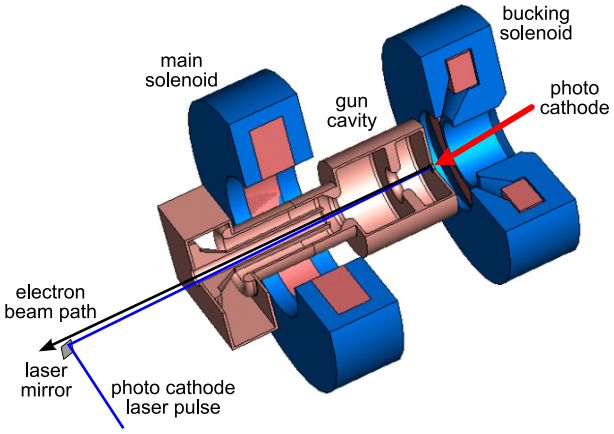

Figure 2.1: *Sketch of the gun cavity including the coaxial coupler and the solenoids.*

The center of the main solenoid magnet is located 27.6 cm downstream of the cathode and is used to focus the electron beam and to allow for an emittance compensation technique, which will be described in more detail in chapter 6.3. An additional bucking solenoid behind the gun is responsible for compensating the magnetic field of the main solenoid at the position of the cathode. This assures that the electron bunches leaving the main solenoid field do not have a residual angular momentum which would lead to an unwanted coupling between x- and y- phase spaces [Milt].

For further acceleration, a TESLA-type booster cavity is used which is a nine-cell copper structure operated in π-mode [Oppe]. The final momentum of the electrons behind the

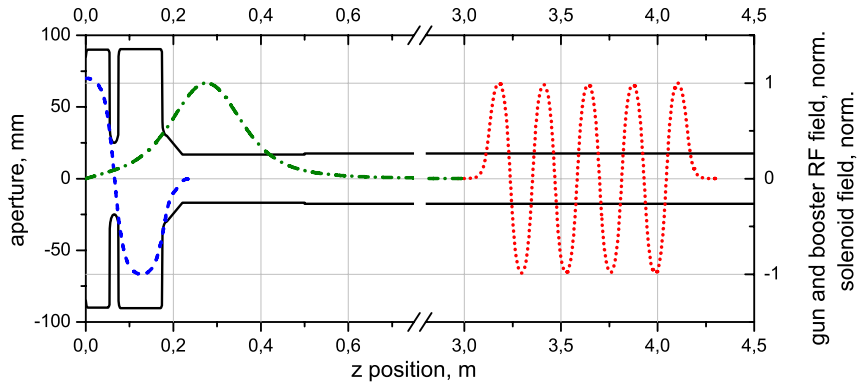

Figure 2.2: *Field geometry in the PITZ beamline. The black line represents the free aperture, the blue, dashed and the red, dotted lines show the RF field distribution of the gun and the booster, respectively. The green, dash-dotted line indicates the solenoid field strength B_z (main and bucking solenoid fields are already superimposed).*

booster cavity can be up to 14.7 MeV/c. The distribution of the electric and magnetic fields are shown in figure 2.2, where the field plots are normalized to unity. Typical run conditions are 60 MV/m as the maximal RF field amplitude on the photocathode, 14 MV/m as the maximum booster gradient and a peak solenoid strength of 230 mT.

2.2 Electron bunch diagnostics

The electron bunches can be characterized in many ways: their charge, the transverse shape and position, the momentum distribution, the longitudinal bunch profile, the longitudinal phase space distribution and finally the transverse phase space distributions in x- and y-direction. The following sub-chapters provide an overview of the techniques used at PITZ for measuring these properties.

2.2.1 Charge

Two different devices are available for measuring the charge of the electron bunches. Firstly, Integrating Current Transformers (ICTs, produced and calibrated by Bergoz [Berg]) are used. These devices can be viewed as coils around the beam pipe. Electron bunches passing such a coil induce a voltage in the windings. Integrating that signal with an oscilloscope and taking into account the calibration factor of 0.8 C/Vs allows to compute the bunch charge. This device is appropriate for the measurement of charge levels larger than 100 pC and is specially suited for the 1 nC regime.
For smaller charges, the Faraday cup (FC) is used, which acts as a charge collector when it is inserted in the beam path. The charge flow, i.e. the current, is observed with an oscilloscope and the total charge can be determined by integrating the signal and scaling it with a calibration factor of 0.02 C/Vs. There is no principle limitation to small charge levels when using a Faraday cup, but the advantage of an ICT is the non-destructive measurement.

2.2.2 Transverse shape and position

The transverse charge distribution as well as the position of the beam can be measured using a view screen together with a camera. At PITZ, screens coated with Cerium doped YAG[3] powder are used which produce broadband light in the visible spectrum. The light intensity is proportional to the number of the electrons and scales with their energy [Spes01]. Another type of screen utilizes optical transition radiation (OTR screens) which occurs when high-energy electrons cross the boundary of two materials having different indices of refraction.
To further detect the absolute position of the electron beam along the beamline, five

[3]YAG = Yttrium Aluminium Garnet

button-type beam position monitors (BPM) are installed at different locations. Furthermore, wire scanners (WS) are employed, where a thin wire is moved transversely through the electron beam. Electrons hitting the wire create showers of gamma quanta which generate light in scintillator plates. The light is detected using photomultiplier tubes (PMT). The integrated PMT-signals vs. wire position yield the projection of the beam shape perpendicular to the wire's moving direction in x and y.

2.2.3 Longitudinal phase space distribution and its projections

The momentum distribution of the electron bunches can be measured using spectrometer dipole magnets. The radius of the deflection curve of a single electron depends on its momentum via $r(p) = \frac{p}{B \cdot e}$, where r is the radius, p the particle momentum, B the magnetic field and e is the elementary charge. Therefore, the beam momentum distribution can be observed on a screen after the dipole and together with the magnetic field these images allow to compute the mean momentum as well as the momentum spread.
The first spectrometer dipole is placed behind the electron gun cavity to measure the beam properties in the low-energy section. This dipole has a nominal deflection angle of 60 degrees and is able to measure beam momenta of up to 8.8 MeV/c, which is sufficient since the maximum of the beam momentum from the gun operated at 60 MV/m is approx. 6.95 MeV/c [Roen].
The second dipole is located after the booster cavity. It is a 180 degrees dipole that was designed to measure momenta of up to 40 MeV/c which is needed for future upgrades of the machine. This dipole also serves as part of a setup to measure the transverse slice emittance [Ivan02].
The resolution of both systems depends on the initial beam parameters, particularly on the quality of the focusing. Under standard conditions, the momentum resolution of the low-energy dispersive arm is about 6 keV/c and that of the high-energy dispersive arm is about 8 keV/c [Roen]. A third dipole is situated at the end of the beamline, but will not be discussed here, because it was not used for the measurements.
To measure the longitudinal bunch profile, two screen stations in the straight section (before and after the booster) are equipped with Čerenkov-radiators (Silica Aerogel) and OTR-screens. The electron bunches passing those radiators create a light pulse whose temporal intensity distribution corresponds to the longitudinal electron bunch distribution. The generated light distribution is imaged onto a streak camera and can be measured with a temporal resolution of the whole system of about 4 ps [Roen] (the streak camera itself has a temporal resolution of about 2 ps).
Finally, these radiators can be inserted in the dispersive sections where the electrons are sorted after their momenta. The generated light distribution is transported and imaged onto the entrance slit of a streak camera. The streak camera adds temporal information to the momentum distribution resulting in the longitudinal phase space distribution in $\{t,p_z\}$-space.

2.2.4 Transverse phase space distribution

The transverse emittance of an electron bunch corresponds to the area of the electron beam's transverse phase space distribution. At PITZ, the transverse emittance is measured using the single-slit scan technique [Stay]. For this purpose, three EMSY[4] - stations are installed at different locations in the beamline. Each of these stations contains a YAG-screen for the observation of the electron beam size as well as slits in the horizontal and vertical direction having openings of 10 μm and 50 μm. Moving the slits into the beam path causes all electrons which are not inside the slit acceptance to be scattered by the tungsten bulk material. The transmitted parts of the beam are called beamlets and due to their small charge the space charge forces can be neglected. These beamlets are observed on a screen (see figure 2.3) and their intrinsic divergence can be determined from their beam size perpendicular to the slit orientation divided by the drift length between slit and screen.
In addition, taking into account the slit position and the divergence of the whole beamlet for each measurement point during the scan, one is able to reconstruct the transverse trace space[5]. This allows to compute the transverse emittance according to Equation 6.7. The transverse emittance measurement setup was designed to have a systematic error of less than 10 % for a broad range of electron beam parameters.
More information about the transverse phase space and the measurement of the transverse emittance can be found in chapter 6.1 and in [Stay].

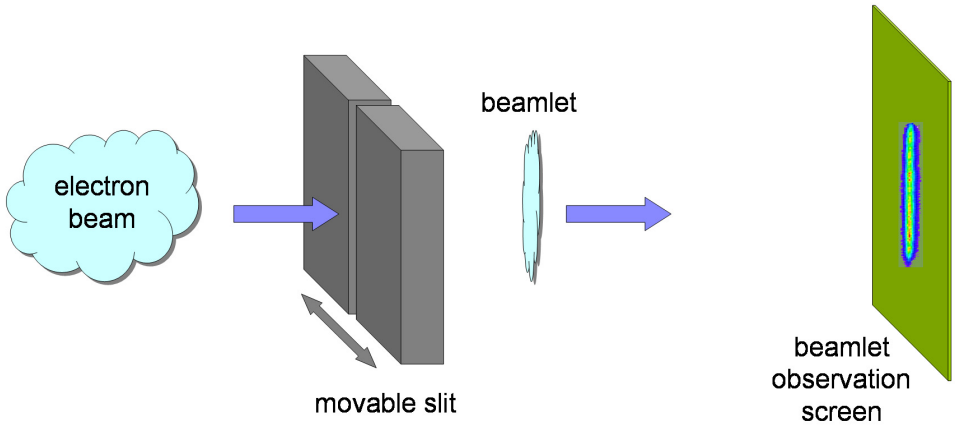

Figure 2.3: *Illustration of the slit scan technique. Only a tiny fraction of the original electron bunch can pass the slit and is recorded by a screen further downstream.*

[4]EMSY = Emittance Measurement SYstem

[5]While the coordinates of the transverse phase space are x and p_x, the transverse trace space has x and $x' = p_x/p_z$ as coordinates.

Chapter 3

Laser system and laser pulse diagnostics

In this chapter the laser system at PITZ which was developed and built by the Max Born Institute Berlin (MBI) will be described at first. Afterwards, the laser transport to the photocathode is introduced and finally the available laser pulse diagnostics in the laser hut as well as in the accelerator tunnel is presented.

3.1 Requirements for the laser system

The laser system must be able to produce a variable number of laser pulses arranged in trains. The pulse spacing within the trains is 1 μs, while the trains have a repetition rate of 10 Hz with 800 pulses per train at maximum. Since the European XFEL will incorporate superconducting accelerator technology, the acceleration of this large number of electron bunches is possible. The laser pulses must have a wavelength around 261 nm (see chapter 5.1) to efficiently extract electrons from the photocathode material (Cs_2Te) and the number of photons must be sufficient to reach a charge level of at least 1 nC.
Because the electron bunch properties strongly depend on the temporal shape of the laser pulse, the optimum conditions of about 20 ps long (FWHM[1]) flat-top profile and rise and fall times as short as possible must be carefully fulfilled. The transverse shape should be a circular flat-top which is not generated in the laser system but in the laser beamline by cutting the magnified beam leaving only the central part using a circular aperture. The energy loss can be up to 80 % in this case which puts even higher demands on the initial laser pulse energy. The reasons for these requirements will be given in section 6.2.
Another important issue is the timing stability of the laser system. The total rms[2] timing jitter between the RF in the gun cavity and the laser pulses must be better than 200 fs [XTDR]. The reason for this stringent requirement is the dependence of the electron bunch properties, like mean momentum and momentum spread, on the RF phase at emission.

[1] FWHM = Full Width at Half Maximum
[2] rms = root mean square

3.2 The laser systems used at PITZ

In the past years, two different laser systems were in use at PITZ, both developed and built by the MBI Berlin. The first one was able to produce pulses with a flat-top temporal profile, a duration of about 20 ps (FWHM) and rise and fall times of the order of 6-7 ps. The laser material used in the oscillator and in the subsequent amplification stages (Nd:YLF) of this laser system did not provide sufficient bandwidth to allow for shorter rise and fall times [Will02].
The successor of that laser system utilizes Yb:KGW as active medium which allows to produce pulses of less than 1 ps duration (FWHM) by the oscillator. In the subsequent amplification stages utilizing Yb:YAG as active medium, the bandwidth is being narrowed so that the final, already shaped pulses have rise and fall times of the order of 2 ps while the total duration can be up to 24 ps (FWHM).
The second laser system was used for the experimental investigations of the work and will be described in detail in the following sections.
In figure 3.1, the overall laser system layout is shown. The laser oscillator provides short laser pulses which are synchronized to the RF master oscillator of the facility. In contrast to all other components of the laser system, the oscillator is working in cw mode, which means that the pulses are continuously emitted at a repetition rate of 54 MHz. After the oscillator, two Faraday isolators (dark cyan) protect the oscillator from parasitic pulses traveling back into the resonator. The next element of the laser system is a Pockels cell[3] which is used to reduce the repetition rate of the pulse train to 1 MHz by turning the polarization of every 54^{th} pulse by 90 degrees. The subsequent wedged birefringent crystal[4] separates both polarizations. The 1 MHz pulse train is sent to the pulse shaper while all other pulses are directed to the regenerative amplifier of the optical sampling system which is described in subsection 3.2.5. The pulse shaper is responsible for the generation of the 24 ps long pulses. Afterwards, the pulses are further amplified in the regenerative amplifier as well as in the double-pass and booster amplifier. Finally, the wavelength of the infrared pulses are converted to the ultraviolet in two steps. The LBO crystal converts the initial wavelength of 1030 nm to 515 nm while the subsequent BBO crystal converts the 515 nm to the final 257.5 nm. To be able to tune the intensity of the laser, a half-wave plate[5] is used to rotate the polarization of the laser pulse and the subsequent birefringent crystal separates both polarizations. Pulses with one polarization state are sent to the photocathode while those of the other are dumped.

[3] A Pockels cell is a device which utilizes the so-called electro-optical effect to rotate the polarization of a traversing laser pulse depending on the applied voltage (usually in the range of kV)

[4] Birefringent crystals have an index of refraction which depends on the orientation of the electric field vector of the incoming light wave in comparison to the crystal axes

[5] A half-wave plate is a birefringent material, which is able to rotate the polarization of an incoming beam. The amount by which the polarization is turned can be controlled by the rotation of the plate around the axis of the laser beam.

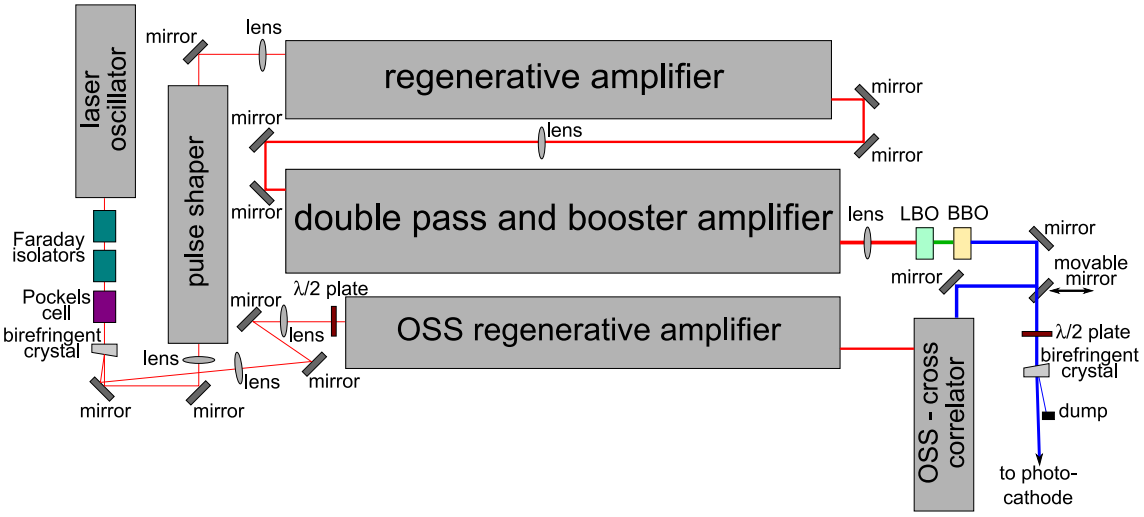

Figure 3.1: *Sketch of the overall laser system setup. (design and construction by MBI Berlin)*

3.2.1 The laser oscillator

The Yb:KGW-oscillator produces short pulses with sub-picosecond duration, a wavelength of about 1032 nm and a repetition rate of 54 MHz. The laser is passively mode-locked[6] by using a semiconductor saturable absorber mirror (SESAM). This mirror is coated with a semiconductor material which in the first place absorbs the laser light. High laser pulse intensities saturate this absorption and therefore the coating becomes almost transparent, which leads to a favoring of short pulses with high intensities. GTI[7] mirrors compensate the stretching the laser pulses experience due to normal dispersion and self-phase modulation in the Yb:KGW crystal.
Once the oscillator is in a state of being mode-locked it will be synchronized and locked to the master oscillator reference. This is done by frequency mixing of the oscillator output signal detected by a fast photo diode and the master oscillator frequency of 1.3 GHz resulting in a signal which can be used to adjust the pulse repetition rate as well as the temporal offset between laser pulse and master oscillator by means of two piezo actuators. The energy of the output pulses is approx. 2 nJ.

[6]Mode-locking: Lasers which produce short pulses need a sufficiently large spectral bandwidth. At start-up all frequency components (or longitudinal modes) present in the laser resonator start from noise and have random phase relations which in sum give low intensity. Fixing (or locking) all modes to a defined phase relation results in individual pulses with short duration and high intensity.

[7]GTI = Gires-Tournois Interferometer, a device which is composed of a partially followed by a fully reflecting mirror. A laser pulse impinging on the GTI acquires a wavelength-dependent phase delay which can be adjusted to counteract the dispersion-induced stretching of the pulse inside the laser medium.

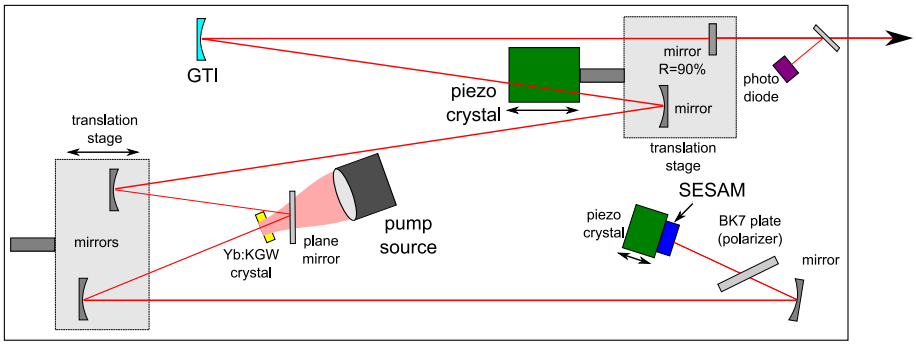

Figure 3.2: *Sketch of the laser oscillator (not to scale). The translation stage on the lower left side provides the possibility to pre-tune the oscillator length so that the correct resonator length is within the range of the piezo actuators. Exemplary, one GTI is shown in this sketch. (design and construction by MBI Berlin)*

3.2.2 The laser pulse shaper

The laser pulse shaper is used to convert the short Gaussian pulses produced by the oscillator into a temporal flat-top shape. In the current state[8], it is composed of thirteen subsequent Yttriumvanadate (YVO_4) crystals having identical dimensions. Each of them is temperature controlled and can be rotated around the axis of the traversing laser beam (see figure 3.3).

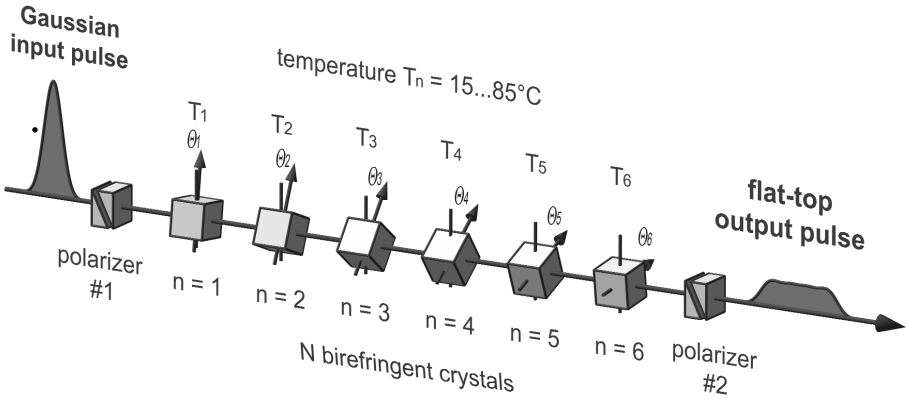

Figure 3.3: *Image of the pulse shaper setup. In this example, the number of birefringent crystals is n=6. For each crystal the rotation angle Θ_i and the temperature T_i can be adjusted to define the output pulse shape. (image courtesy of I. Will, MBI Berlin)*

[8]It can be extended to more crystals to produce longer pulses.

YVO_4 is a birefringent material and therefore has two perpendicular optical axes (ordinary and extraordinary axis). Each of them has its own refractive index ($n_o(\lambda)$ and $n_e(\lambda)$) with the corresponding difference in the propagation speed of light. The optical properties of these crystals depend on the direction of the electric field vector of the light with respect to the optical axes. Upon entering the first crystal, the laser pulse is split into two replicas whose intensities are proportional to the projections of the polarization vector onto the ordinary and extraordinary optical axis, respectively. Since the refractive indices are different, the passage time of both copies differ. At the exit of the crystal, this results in two pulses of perpendicular polarization. Their temporal separation is given by $\Delta t = L \cdot \left(\frac{1}{v_o} - \frac{1}{v_e}\right)$, with L being the crystal thickness and v_o and v_e the group velocities on the ordinary and extraordinary axes, respectively. The phase delay $\Delta\varphi$ between these pulses can be tuned precisely by changing the crystal temperature and thus its length.
These two pulses enter the next crystal and are again split into two copies. After passing the crystal, the acquired delay between both double-pulses equals the temporal pulse separation within the double-pulse $\Delta t_{double} = \Delta t$ since the thickness of the crystals is the same. For this reason, the central two sub-pulses overlap precisely and the total number of temporally separated (but overlapping) sub-pulses is three. Repeating this principle in total thirteen times and finally applying a polarizer results in a linearly polarized, approximately 24 ps long flat-top pulse consisting of fourteen sub-pulses provided that the rotation angles and temperatures are correctly chosen (see figure 3.4).
The principle of this pulse shaper is based on a Šolc fan filter [Šolc]. For more information about birefringent filter networks in general see [Wolf]. Specific information about the pulse shaper installed at PITZ can be found in [Will01].

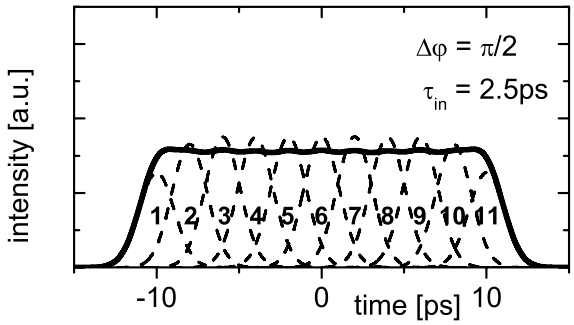

Figure 3.4: *Simulated formation of a temporally flat-top laser pulse by coherent stacking of short Gaussian pulses (2.5 ps FWHM). In this example, ten crystals were used which results in eleven replicas of the incoming laser pulse. Here, the assumed phase delay between the pulses traveling on both optical axes is $\Delta\varphi = \pi/2$. (image courtesy of I. Will, MBI Berlin)*

By completely removing the pulse shaper, the laser system can produce UV output pulses with a Gaussian temporal shape having a duration of approx. 2 ps (FWHM).

3.2.3 The regenerative amplifier

After passing the pulse shaper, the laser pulses are amplified by means of a regenerative amplifier. The layout of the regenerative amplifier is depicted in figure 3.5. The incoming laser beam is reflected by a mirror and subsequently transmitted through a wedged polarizer (birefringent crystal) and the switch-in Pockels cell. While the laser pulse is reflected at the mirror, this Pockels cell switches and turns the laser pulse polarization by 90 degrees. This causes the birefringent crystal to refract the pulse to a different direction. Now the pulse is switched into the resonator. It travels back and forth between the mirrors behind the Pockels cells and is amplified by the pumped Yb:YAG crystal. During fifteen round trips, the laser pulse is amplified by a factor of 10^6. Finally, the switch-out Pockels cell releases the laser pulse.
It is possible to insert an additional Lyot filter [Lyot] in the resonator part of the regenerative amplifier to reduce the spectral bandwidth of the laser pulse. This results in a smoother flat-top plateau in the temporal laser distribution and slightly longer rise and fall times [Will01]. Without inserted pulse shaper, the insertion of Lyot filters leads to a stretching of the Gaussian UV pulse. Pulse durations of up to 12 ps (FWHM) with a small spectral bandwidth have been demonstrated.
The used laser material (Yb:YAG) amplifies at a wavelength of about 1030 nm. Therefore, this wavelength is selected as new center wavelength which is possible since the spectrum emitted by the oscillator is sufficiently broad.

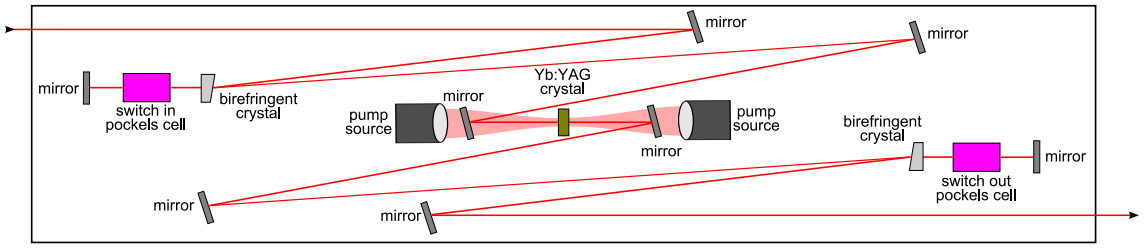

Figure 3.5: *Sketch of the regenerative amplifier. (design and construction by MBI Berlin)*

3.2.4 Double-pass and booster amplifier

The final amplifiers of the laser system are used to boost the single-pulse energy to the desired level. The layout is shown in figure 3.6. The pulses from the regenerative amplifier enter at the upper left corner and travel to the right. Since the pulses are reflected back

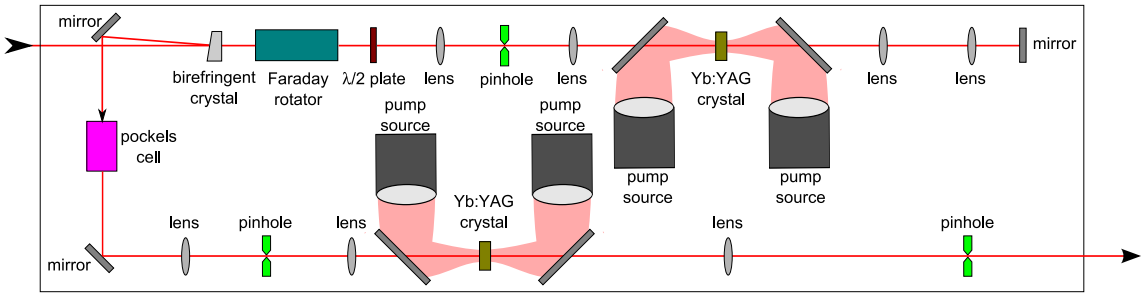

Figure 3.6: *Sketch of the double pass (upper part) and booster amplifier (lower part). (design and construction by MBI Berlin)*

by the mirror in the upper right corner, the Yb:YAG crystal is passed twice and the birefringent wedged crystal refracts the amplified pulses towards the lower part of the amplifier. There, a Pockels cell selects the desired number of final laser pulses. These pulses are amplified once more in the booster stage to reach the final pulse energy of approximately 100 μJ.
The refraction of the returning laser pulse towards the lower branch requires, that the polarization of the pulse has turned by 90 degrees. This can be accomplished by combining a Faraday rotator and a half-wave plate. Both elements turn the polarization of the traversing laser beam. But when these elements are passed in the reverse direction, half-wave plates restore the initial polarization whereas the Faraday rotators increase the angle of rotation again by the same amount. In the case of this amplifier it means, that the polarization of the pulses (entering in the upper left corner) is first rotated in the Faraday rotator by 45 degrees which is immediately corrected by the subsequent half-wave plate. When returning, the half-wave plate turns the polarization back to 45 degrees and the Faraday rotator increases it to 90 degrees in total.

3.2.5 The optical sampling system (OSS)

The optical sampling system is part of the whole laser system and can be used on demand to measure the temporal profile of the UV laser pulses. It is based on the principle of a cross correlator - within one pulse train, short probe laser pulses are temporally scanned over the UV laser pulses by linearly changing the relative timing between them. The nonlinear difference frequency generation (DFG)[Boyd] is used to provide an optical effect which occurs only in case both pulses overlap in space and time and whose signal strength is proportional to the intensity of both pulses. Therefore, the recorded DFG-signal vs. the relative delay represents the convolution of the temporal shape of the UV pulses with the infrared probe pulses. Since this is a multi-shot technique, it must be guaranteed that all pulses are identical in shape and intensity. In figure 3.7, the layout of the optical

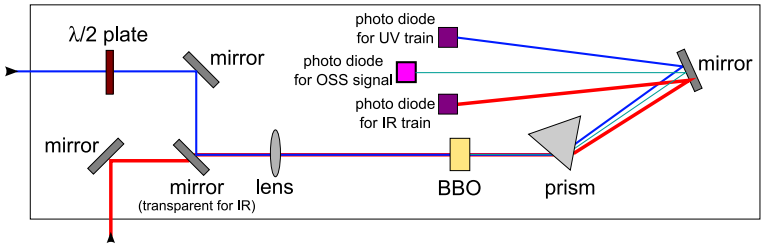

Figure 3.7: *Sketch of the OSS cross correlator. The UV pulse train (upper left) and the IR pulse train (lower left) are spatially overlapped and focused into the BBO crystal. This crystal generates a signal at the difference frequency (λ=343 nm) when both pulses are overlapping in time. A prism separates the three wavelengths so that they can be detected individually. (design and construction by MBI Berlin)*

cross correlator is shown. The UV and probe pulses are spatially overlapped in a thin BBO crystal which generates the difference frequency signal at a wavelength of about 343 nm. The short probe pulses used for the sampling stem from the laser oscillator and are amplified in an additional regenerative amplifier. The generated pulses have a duration of about 1 ps and a wavelength of about 1032 nm. In figure 3.8, the regenerative amplifier used for the OSS measurements is shown. As described in chapter 3.2, only every 54^{th} pulse of the oscillator is used in the main laser system. All other pulses are directed to the OSS regenerative amplifier, which, when turned on, picks out one of the remaining 53 pulses by means of a Pockels cell and amplifies it. The general layout of the regenerative amplifier is very similar to the one of the main laser system described previously. The difference is that the amplifier needs to support a larger bandwidth to produce short probe pulses. Therefore, Yb:KGW was chosen as the laser medium. Since this is the same material as in the laser oscillator, the center wavelength remains at 1032 nm.

At one end of the regenerative amplifier, the fixed mirror has been replaced by an oscillating mirror which shortens the resonator length during one scan. Therefore each pulse of the IR laser pulse train acquires a different temporal delay with respect to the

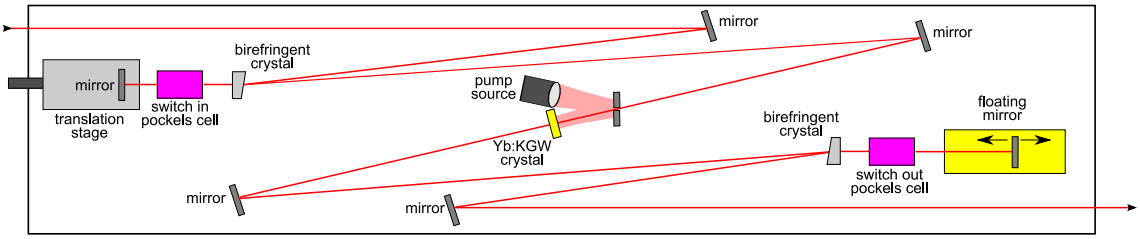

Figure 3.8: *Sketch of the regenerative amplifier used for the Optical Sampling System. (design and construction by MBI Berlin)*

pulses of the UV train. After one scan the original position of the oscillating mirror is restored. The translation stage on the left hand side in figure 3.8 allows a pre-adjustment of the resonator length to provide a temporal overlap of the IR and UV pulses within the scan range.

3.3 The laser beamline

In this sub-chapter, the laser beamline which is responsible for the transport of the laser light to the photocathode is described. It was designed to produce laser pulses with a transverse shape close to a circular flat-top at the position of the photocathode. Therefore, the laser beamline is split into two parts. The first part realizes an imaging of the laser pulses from the laser system onto the Beam Shaping Aperture (BSA) with a proper magnification. The BSA cuts out the central part of the magnified transverse distribution and the second part of the laser transport system provides an imaging onto the photocathode with unit magnification. The transverse laser spot size can be varied by choosing BSAs with different diameters.

3.3.1 Imaging on the Beam Shaping Aperture

The laser system was designed such that the object plane is located between the frequency conversion crystals (see figure 3.1). The image plane is at the position of the BSA in the tunnel. The total distance amounts to 13.0 m. The first part of the laser beamline is installed on the laser table and easily accessible while subsequently the laser beam has to be transported vertically to the level of the accelerator tunnel. Finally, it traverses a small hole in the tunnel wall which has a thickness of about 2 m for radiation safety reasons. Optical elements can be placed on the laser table and on a rail which is installed in the vertical shaft. The magnification of that imaging system is a compromise between two considerations. The transverse laser profile, which is emitted from the laser system, is close to a Gaussian distribution. For that reason, cutting the tails of that distribution by the BSA, leaves a transverse profile which has a maximum in the center. The intensity difference between center and edge of the transverse distribution is smaller for larger magnifications.

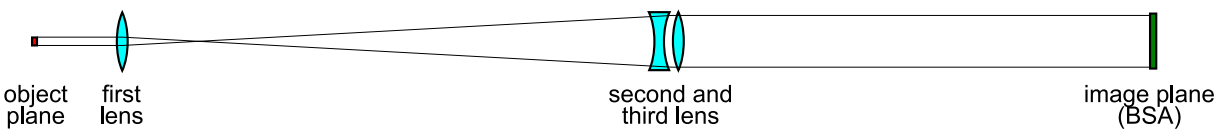

Figure 3.9: *Sketch of the laser beam transport system from the object plane of the laser to the Beam Shaping Aperture including rays which indicate the magnification.*

On the other hand, a large magnification means that more laser pulse energy is lost at the BSA.
The initial beam size at the object plane was measured to be $x_{rms} = 107\,\mu$m and $y_{rms} = 95\,\mu$m (measured as rms-value of small cuts through the center of the transverse distribution). The reason for the asymmetry is the different angular acceptance of the frequency conversion process in the BBO crystal for both planes[9].
As a compromise between all given constraints, it was decided to use a Kepler-like telescope consisting of three lenses. The last two lenses are combined to produce an element of arbitrary focal length [Hafer](see figure 3.9). The overall magnification for this setup is about 6.5.

3.3.2 Imaging onto the photocathode

This imaging scheme was proposed by I. Will (MBI Berlin) and was designed to provide unit magnification and a large depth of focus to be tolerant against small misalignments. It consists of four lenses installed on a rail in the tunnel. The general layout is depicted in figure 3.10.

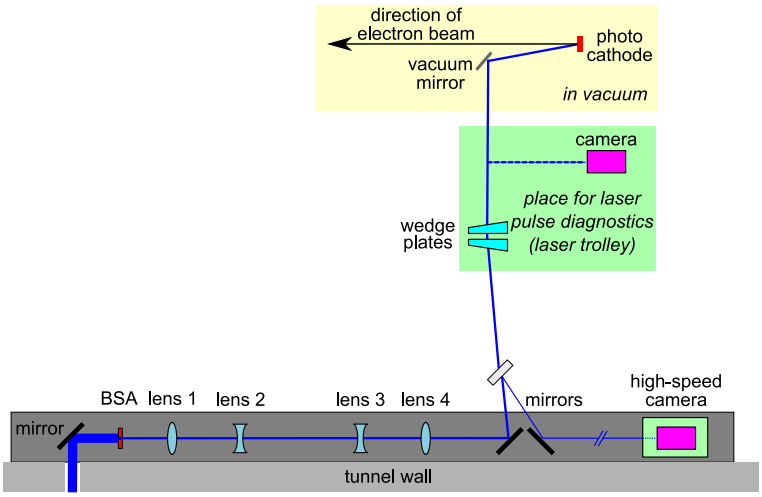

Figure 3.10: *Sketch of the optical layout in the tunnel for imaging from the Beam Shaping Aperture to the photocathode (image not to scale). The laser pulse diagnostics (green areas) will be described in section 3.4. The optical path lengths to the displayed cameras equal the one to the photocathode.*

[9]The efficiency of the frequency doubling in a crystal depends on the direction of the laser pulse with respect to the optical axes. Since convergent or divergent laser pulses have a direction which depends on the transverse position inside the laser pulse, also the efficiency becomes position dependent. In the case of the used BBO crystal the position dependence is more pronounced for the vertical axis.

To fine-tune the imaging, one can use the cameras in the laser diagnostics section (laser trolley, see figure 3.10, green area) which are placed such that the laser beam has the same optical path length to the cameras as to the photocathode (see chapter 3.4).
In order to change the laser beam position on the photocathode, there are two main options. One of them is to use the last mirror on the rail whose tilts around two orthogonal axes can be remotely controlled. The other option is the usage of two wedge plates installed on the laser trolley. Each of these wedge plates is changing the direction of the laser beam by a constant angle. Rotating both wedge plates independently around the direction of the laser beam allows to steer the beam very precisely. More information about this so-called Risley prism pair can be found in [Yang].
These two beam steering methods are necessary to change position and direction of the laser beam and thus align the laser onto the photocathode. The tolerances against misalignments of the optical imaging were calculated using the ABCD-transfer matrix formalism for ray optics [Hodg]. Since all lenses have large focal lengths, using the paraxial approximation of this formalism is justified. Assuming that the imaging distance from the BSA to the photocathode is different from 6750 mm, it was computed by which amount each lens has to be moved individually in order to move the image plane to the new photocathode position. In addition, the resulting change of the magnification was derived (see figure 3.11).

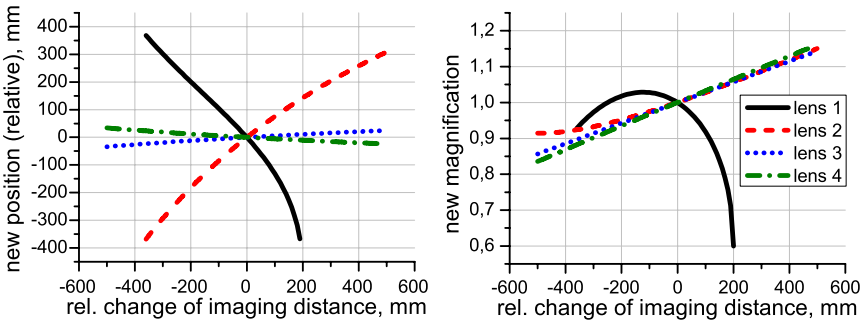

Figure 3.11: *The left part of the figure shows by which amount each lens has to be moved in order to correct for a changed imaging distance. The right part shows the corresponding change of the magnification.*

From these calculations one can conclude that the change of the imaging distance is smallest when the first or the second lens are displaced but of these two only the second lens shows a small variation of the magnification. Therefore, the second lens should be used to fine-tune the imaging.
In addition, measurements of the transverse laser profile at different positions before and behind the imaging plane were performed. The camera used for these measurements was

of type Jai Pulnix TM-2040GE (UV-capable). The results of these measurements can be seen in figure 3.12.
At the design position, an image of the laser light transmitted through the BSA hole can be detected. At other positions, diffraction patterns appear as a fringe structure imposed on the actual transverse distribution. For larger distances to the image plane, the number of fringes is reduced but the modulation depth increases. In addition, the steepness of the edges is reduced.

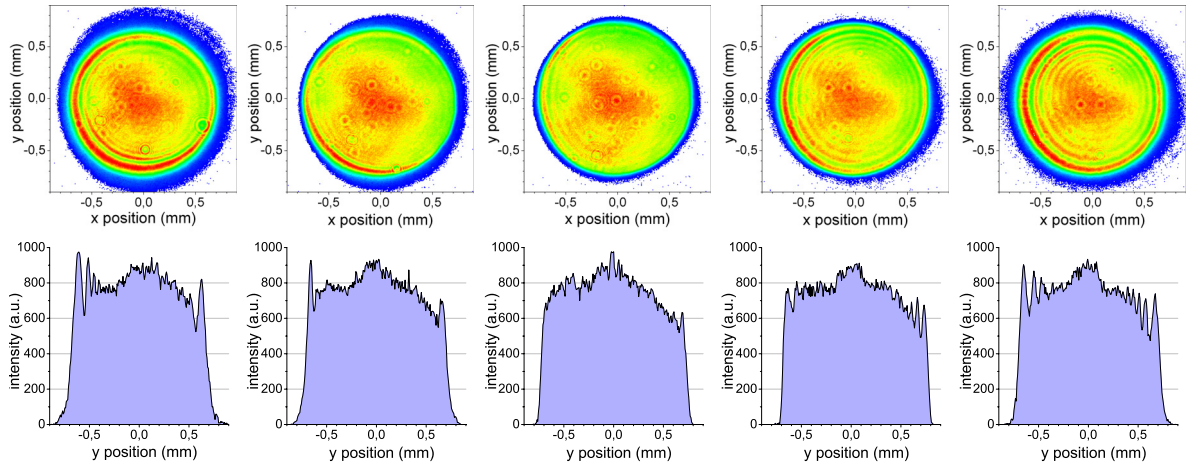

Figure 3.12: *These images show the transverse laser pulse distributions (upper) and centered vertical cuts (lower) at different positions around the nominal imaging plane. From left to right, the distances to the nominal imaging plane are -5.0 cm, -2.5 cm, 0 cm, +2.5 cm and +5.0 cm. The transverse axes range from -0.9 mm to +0.9 mm. The BSA had a diameter of 1.5 mm. The very small circular imperfections visible on some graphs result from dust on the entrance optics of the camera. The complete set of measurements ranging from -20.0 cm to +20.0 cm can be found in Appendix A.*

3.4 Laser pulse diagnostics

It is of particular interest to monitor all laser pulse properties which can have an impact on the electron bunch characteristics, i.e. the temporal and the transverse shape, the laser pulse energy and its stability as well as the laser pulse position and its stability. For each of these properties one or more measurement devices are installed which will be described in the following sub-chapters.

3.4.1 Temporal laser pulse shape

In this section, the devices for measuring the temporal laser profile are presented. Since they were very important for many measurements presented in this thesis, they are described in more detail than the measurement techniques for other laser pulse properties. While in section 3.2.5 the physical layout of the OSS was introduced, the first part of this section is dedicated to the investigation of its measurement precision. Afterwards, the streak camera Hamamatsu FESCA200 (C6138) will be introduced. It was borrowed from DESY Hamburg for dedicated measurements.

The Optical Sampling System

The Optical Sampling System (OSS), which was described in chapter 3.2.5, is based on an optical cross-correlation of the UV pulse with a sub-picosecond infrared pulse. The latter is temporally scanned over the UV pulse and the nonlinear process of difference frequency generation (DFG) between both spatially overlapping pulses results in a cross-correlation signal which corresponds to the temporal intensity shape of the UV pulse provided that the IR probe pulse has a much shorter duration. In the ideal case, the cross correlation signal has the mathematical form

$$I_{DFG}(\tau) = \int_{-\infty}^{\infty} \chi \cdot I_{IR}(t-\tau) \cdot I_{UV}(t)\,\mathrm{d}t. \tag{3.1}$$

In this equation, t is the time, τ is the relative delay between both pulses, I_{IR} and I_{UV} denote the time-dependent intensities and χ is a scaling factor[10].
This equation already shows the main disadvantage of this method. It implicitly assumes that during one scan the temporal shape of the UV flat-top pulses $I_{UV}(t)$ and the short probe pulses $I_{IR}(t)$ remain the same. In addition, the temporal resolution of such a scheme strongly depends on the duration of the probe pulses. When they are too long, the short temporal features of the UV pulse cannot be resolved. Since it was not possible to measure the duration of the probe pulse directly, the spectral intensity was measured instead and the corresponding bandwidth limited duration was calculated. The width of the spectral distribution was determined[11] to be σ_λ=0.77 nm at λ_0=1031.6 nm. Assuming a Gaussian pulse shape with a constant phase, this corresponds to a minimal duration of about 0.86 ps (FWHM). Taking into account that no optical element is present which compensates the stretching (chirp) of the probe pulse which it acquired during its amplification in the OSS regenerative amplifier, it is likely that its duration exceeds 1 ps (FWHM).

[10] Usually this equation is defined for the electric field vectors of all waves with χ as a tensor of third order, which includes all properties of the material in which this process takes place. In our case, it is sufficient to use this simplified expression because the polarization of all waves remains constant. For more information see for example [Boyd] and [Treb].

[11] Measured using a spectrometer of type Avantes AvaSpec 2048 (on loan from MBI Berlin)

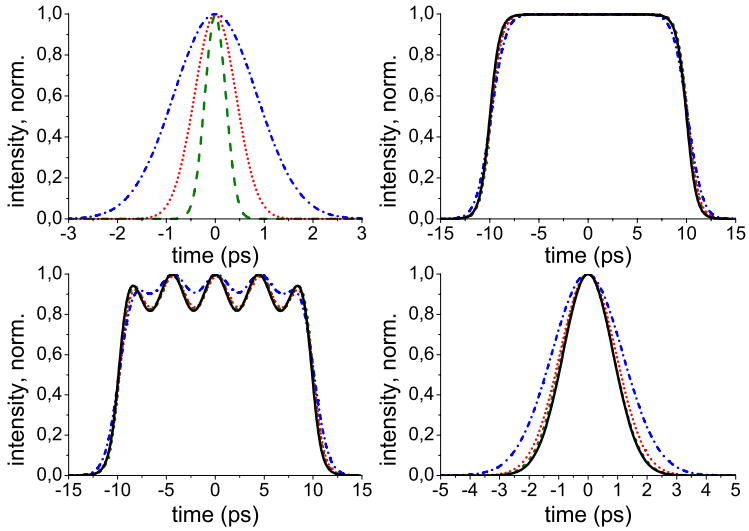

Figure 3.13: *Examples of numerically simulated cross correlation signals. In the upper left graph, the shapes of different probe pulses are shown. Their durations are 0.5 ps (green, dashed), 1.0 ps (red, dotted) and 2.0 ps FWHM (blue, dash-dotted), respectively. The other graphs display different original pulse shapes (20 ps flat-top, 20 ps flat-top with modulations and 2 ps (FWHM) Gaussian) together with their cross correlation signals. The color code in these graphs is equal to the one used in the upper left graph.*

In figure 3.13, the result of a simulation is presented showing how the finite duration of the probe pulses influences the measured temporal laser shape. The durations of the probe pulse were chosen to be 0.5 ps, 1.0 ps and 2.0 ps, respectively, and the cross correlation signals were calculated for three different cases. The first one is the nominal operating case of a 20 ps long flat-top pulse with 2 ps rise and fall times. In the second example some modulations were introduced on the flat-top part of the laser pulse and in the last case the results for a short Gaussian UV pulse with a duration of 2 ps are presented. While the distortion of the simulated temporal shape of the flat-top pulse are in all cases small, a 2 ps long probe pulse leads to an overestimation of the duration of the Gaussian pulse and an underestimation of the modulation depth in the case of the modulated flat-top pulse. These results show, that a probe pulse duration of less than 1 ps is acceptable.
Another peculiarity of the OSS measurements is the fact, that the laser runs in a regime which is very different from typical run conditions. Firstly, to use the OSS, a long pulse train of usually 550 pulses is needed in order to have a sufficient sampling resolution. This puts a larger heat load on the components of the booster amplifier and the frequency conversion crystals leading to a change of the temporal shape while the system approaches its new thermal equilibrium. Another heat-load effect is present in the OSS regenerative

amplifier since it always starts from a cold state when the OSS is switched on. In contrast to the warming-up of the main laser system, this does not lead to a change of the temporal shape of the UV pulses but to a different temporal resolution of the OSS. To quantify these effects, the laser was setup to provide short Gaussian UV laser pulses. This allows to summarize the deteriorating effects in a single quantity. It is the rms laser pulse duration, which was obtained by applying a Gaussian fit to the measured OSS signal. In figure 3.14 (left), the change of the measured rms pulse duration is shown. In this

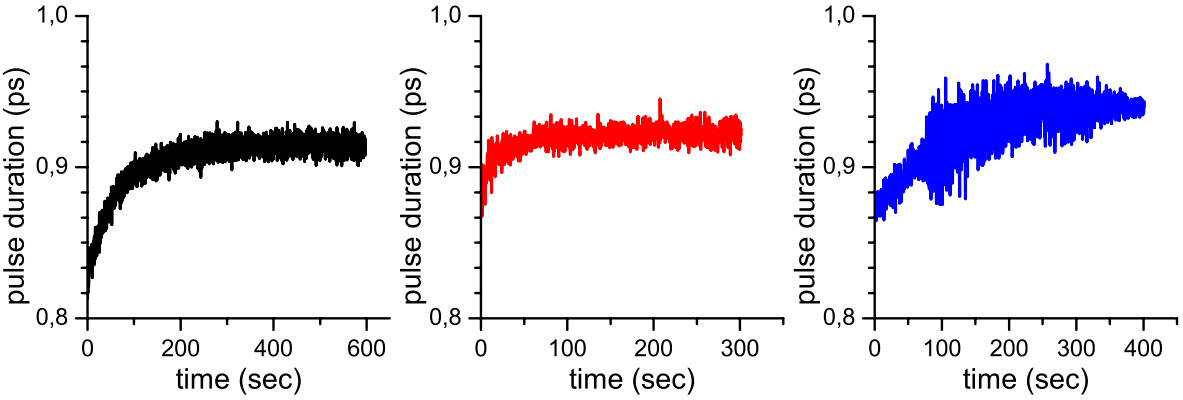

Figure 3.14: *Results from the measurements of the warming up effects present in the OSS. Left: Standard procedure of using the OSS, Center: BBO crystal blocked, Right: OSS regenerative amplifier switched on from cold state.*

case, the regenerative amplifier of the OSS is switched on and immediately afterwards the number of pulses is increased to 550. The pulse duration increases by 9.5 % from 0.82 ps to 0.92 ps. To disentangle the warming up effects caused by different laser components, further measurements were performed. In figure 3.14 (center), the evolution of the pulse duration caused by the warming up of the BBO conversion crystal (responsible for the conversion of the laser pulses from 515 nm to 257.5 nm) is depicted. The OSS regenerative amplifier was switched on and approached its thermal equlibrium while the full UV laser pulse train (550 pulses) was blocked in front of the BBO frequency conversion crystal. The BBO crystal of the frequency conversion stage was unblocked immediately after the measurement was started. The pulse duration changes by about 4.5 % from 0.88 ps to 0.92 ps. The last measurement in figure 3.14 shows the influence of the warming up of the OSS regenerative amplifier. The main laser system including the frequency conversion crystals was running with 550 pulses until it was in thermal equilibrium before the OSS regenerative amplifier was switched on. Here, the influence on the measured pulse duration is stronger than in the case of the BBO crystal. The measured pulse duration changes by about 8 % from 0.87 ps to 0.94 ps. The different final pulse duration in the last case results from the fact that the laser had to be resynchronized between the measurements. This

changed slightly the characteristics of the oscillator pulses and therefore of the emitted UV pulses. Please note that the time constants for the thermalization of the BBO crystal and the OSS regenerative amplifier are much different. The BBO crystal reaches its equilibrium after about one minute while the regenerative amplifier needs about five minutes. To be comparable between different measurements, the operators should wait at least five minutes after the OSS was switched on before measurements are done.
As will be shown in section 4.5, the effect of thermal lensing can cause a change of position and/or size of the laser pulses along the pulse train at the location of the DFG-crystal [Koech]. This results in a varying overlap of the UV and the IR pulses which affects the precision of the OSS measurement.
Finally, the process of difference frequency generation strongly depends on the so-called phase matching condition. This means that the participating light waves need to have the same wavelength-dependent phase velocity which is generally ensured by choosing a proper direction of propagation through the crystal. Slight misalignments can lead to a favoring of the high or low frequency components of the UV pulse and/or the IR pulse which results in a deterioration of the measured temporal laser shape. In the case of collinear beam propagation, this corresponds to a tilt of the DFG crystal around one axis perpendicular to the propagation direction. Studies have been performed to measure this effect. In figure 3.15 the measured temporal shapes for different tilts of the DFG crystal around its optimum (initial) setting are shown. These measurements demonstrate how important a careful alignment of the DFG crystal is. The actual temporal laser pulse shape was not a flat-top in this investigation.

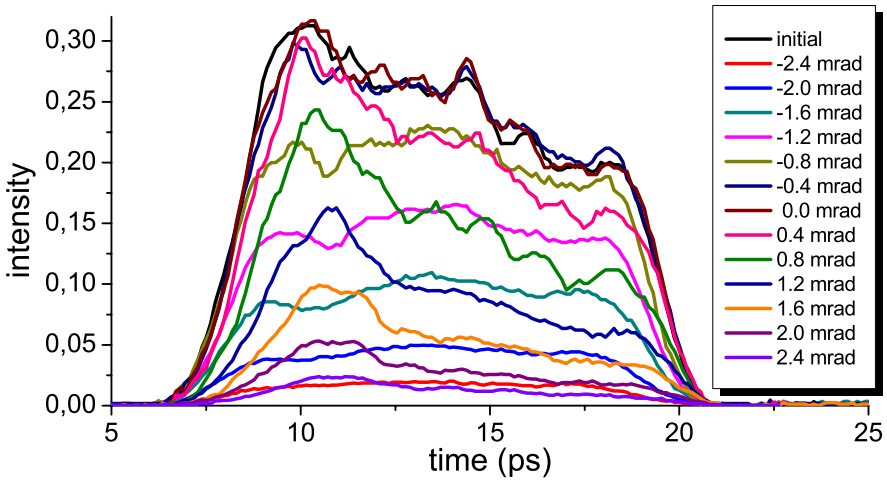

Figure 3.15: *Measured temporal shapes with different tilts of the DFG crystal.*

It must be mentioned, that the Optical Sampling System is the only way to measure the temporal laser pulse profile with a relatively high precision (temporally and in intensity) at the given wavelength and laser pulse energy. The streak camera, which is introduced next, has a comparable temporal precision but the intensity resolution is rather low. FROG techniques [Treb] cannot be used because second order processes as they are used for SHG FROG or GRENOUILLE are not possible at the required wavelength and the limited intensity of the UV pulses does not allow to use third-order nonlinear processes like in TG FROGs.

The streak camera Hamamatsu FESCA200

To have an independent measurement of the temporal laser profile, studies have been performed using a streak camera with an appropriate temporal resolution. The Hamamatsu FESCA200 [Hama01] is the only streak camera offering sub-picosecond resolution in the UV. According to [Tomiz], the temporal resolution was measured to be about 800 fs at a wavelength of 262 nm.

Before introducing the measurements in chapter 4, the working principle of a streak camera will be explained here in brief (see figure 3.16). When a light signal is shone onto the entrance slit of the streak camera, the internal optics (lenses or mirrors) image the slit onto an appropriate photocathode material (depending on the desired wavelength range). The extracted electrons, the number of which is proportional to the light intensity, are immediately accelerated using a high DC voltage of several kV. This strong acceleration is necessary to translate the temporal light distribution into a longitudinal electron density

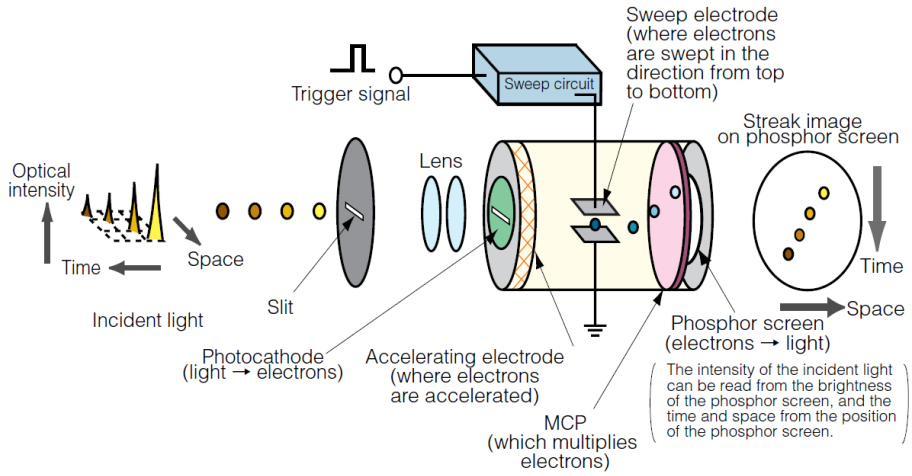

Figure 3.16: *Working principle of a streak camera. Illustration taken from Hamamatsu homepage, http://www.hamamatsu.com*

distribution before the repulsion of the electrons can deteriorate this process and therefore reduce the temporal resolution. In the next step, the electron bunch crosses a rapidly changing electric field perpendicular to the electron direction. During this voltage sweep, the amount of deflection that one electron experiences depends linearly on its longitudinal position in the bunch. Thus, the temporal distribution of the electron bunch is converted into a transverse distribution. In the next step, the electron bunch density (i.e. signal strength) is increased by means of a microchannel plate[12] (MCP). Behind the MCP, the electrons hit a fluorescent screen. Its light distribution is finally imaged onto a CCD[13] camera and can be read out by a personal computer.
The high temporal resolution of this device is accompanied by the drawback that the dynamic range of the FESCA200 is only 1:40 [Hama02]. In addition, this streak camera has an ultra-high sensitivity (single-photon detection is possible) which requires a very strong attenuation of the laser pulses. This leads to the fact that the measured temporal laser shapes are obtained by photon counting which reduces the intensity resolution.

3.4.2 Transverse laser pulse shape

Another important laser pulse property is the transverse shape of the laser pulses impinging on the photocathode. In the PITZ tunnel, two different measurement systems are installed. The first system consists of cameras which are mounted on the laser trolley. Beam splitters can be moved into the laser path reflecting the laser light towards the cameras, which are positioned such that the laser pulses experience the same optical path lengths to the cameras as to the photocathode. Therefore, they are called virtual cathodes (VC). The laser light illuminates directly the CCD chip. The cameras are synchronized to the machine master clock and the transverse laser shape can be measured and processed using an appropriate video software [Weis]. In the run periods before 2007, analog cameras of type JAI M10SX[14] were used primarily but showed many disadvantages. Firstly, the CCD chips were protected by a cover glass, which is not specially suited to transmit UV light. Instead it produced fluorescence light which appears as an additional background to the actual signal[15] (halo around the laser spot in left image of figure 3.17). Moreover, these cameras were equipped with micro lenses which focus the light onto the active area of each pixel[16]. The micro lenses tend to become opaque for UV light (visible light was not affected), since they are made of polymer materials whose chemical bonds are broken under UV light exposure (photo fragmentation). This caused

[12] A microchannel plate is a two-dimensional array of tiny tubes (or channels) each acting as an individual electron multiplier by secondary electron emission. Therefore, a MCP combines the sensitivity of a photomultiplier tube (PMT) with spatial resolution.

[13] CCD = Charge Coupled Device

[14] These cameras have a resolution of 782 x 582 pixels and a pixel size of 8.3 μm x 8.3 μm.

[15] A study of the fluorescence can be found in Appendix B.

[16] This is usually only about 30% of the actual chip size

a rapid and inhomogeneous change of the sensitivity across the CCD chip distorting the measurement of the transverse profile.
For these reasons, another type of camera was installed which is UV capable (JAI Pulnix TM1405-GE OP21-1UV). This camera does not have micro-lenses and the glass cover plate is replaced by a plate made of quartz. In addition, the camera has a higher resolution of 1392 x 1040 pixels and a pixel size of only 4.65 μm x 4.65 μm. No position-dependent degradation of the sensitivity has been observed even after several months of use. Other advantages are that the connection to the control system is done via lossless Gigabit Ethernet connection and the dynamic range is 1:4096 (12 bit) in contrast to the analog camera having 1:256 (8 bit). In figure 3.17, examples are displayed which demonstrate the difference in quality of images taken by both camera types.

Finally, one peculiarity of both camera types must be mentioned. Since the laser light is coherent and the thin protection cover plates have no anti-reflective coating, position-dependent interference patterns can occur which add to the actual transverse shape. For these reasons, it is planned to use cameras without micro lenses and without any cover plate. To protect the CCD chip, a custom made window made of anti-reflectively coated fused silica will be mounted instead. First measurements with such kind of cameras have been done already (see measurement of depth of focus, Appendix A).

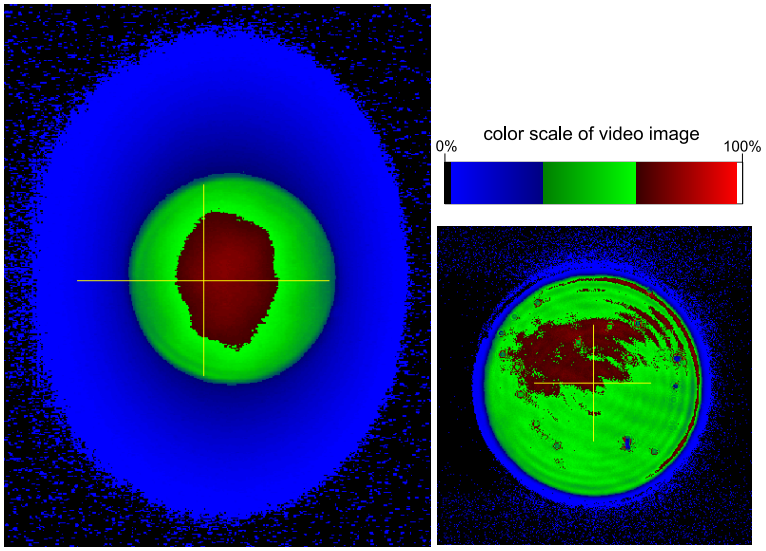

Figure 3.17: *Left: image taken with JAI M10SX, right: image taken with JAI Pulnix TM1405-GE OP21-1UV*

3.4.3 Laser pulse energy

At PITZ, experiments are done which require charge levels differing by many orders of magnitude (sub-pC to some nC). In addition, the quantum efficiency[17] η of the photocathodes can vary between 0.5 % and more then 10 %. This translates to needed laser pulse energies in the range of 50 pJ to 1 μJ. To cover this range, it was decided to use photo multiplier tubes (PMT) having a large dynamic range for the measurement. Nevertheless, a strong attenuation is needed which is accomplished by using four subsequent reflections from quartz surfaces. A fifth reflecting surface can be switched between a fully reflecting mirror or another quartz plate resulting in total attenuation values of approx. $2 \cdot 10^{-6}$ and 10^{-7}, respectively, assuming a reflectivity of 4 % for each quartz surface. The actual value depends on the angle of incidence and the polarization of the light. This assures a proper matching of the laser pulse energies to the linearity range of the PMT. This range is mainly determined by space charge forces of the emitted electrons and the discharge characteristics of the capacitors which stabilize the voltage between the dynodes. To avoid problems with ambient light creating strong background signals, the photocathode material of the PMTs was chosen to be Cs_2Te which is insensitive for wavelengths longer than 300 nm. For a general introduction to PMTs see [Hama03] and for their application at PITZ see [Ivan01]. A sketch of the readout of the PMT signals is shown in figure 3.18. Since the resulting PMT signals yield only relative information, an absolute measurement of the laser pulse energy is needed. For this reason, a calibrated commercial photodiode

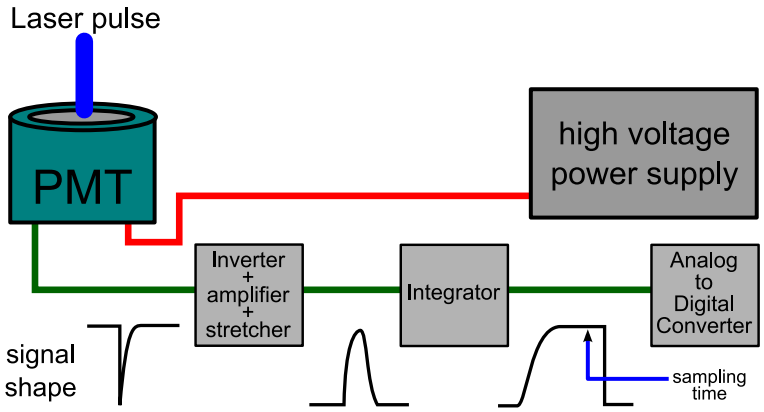

Figure 3.18: *Sketch of the readout electronics for the acquisition of PMT signals. The short signal from the PMT is amplified, stretched and inverted before it is integrated. The ADC timing is chosen to sample the integrated signal on the plateau part (marked with blue arrow).*

[17] Quantum efficiency is the ratio of number of the emitted electrons and the number of incident photons

(Ophir NOVA II with photodiode PD10-pJ SH) was installed in the laser trolley. An attenuated part of the laser pulse can be directed to the photodiode by means of movable mirrors. The diode is capable of measuring single-pulse energies in the range of 50 pJ to 200 nJ.
While the PMT can measure the energy of all pulses, the photodiode is only capable to measure one single pulse per train. The reason is that the maximum pulse repetition rate of the photodiode is 12 kHz which is less than the required 1 MHz.

3.4.4 Laser pulse position

While it is possible to determine the position and the position jitter of the first pulse of each train using the virtual cathodes, this method fails for trains having more pulses since due to the long exposure time of the camera this measurement yields only averaged values. Therefore, another diagnostics device has been introduced. A quadrant diode (QD) consists of four square-shaped photodiodes arranged like the quadrants of a coordinate system (see figure 3.19). The total size of the used QD (Hamamatsu S4349) is 3 mm x 3 mm and the diodes areas are separated by a gap of width $g = 100\,\mu$m. For each pulse impinging on the QD, the voltages generated in each quadrant are read out. Together with the transverse laser pulse shape measured by the virtual cathodes, the actual position of the laser pulse can be retrieved. This method assumes that the transverse shape of the laser pulses does not change along the whole train which is not always justified as discussed chapter 4.5. Furthermore, one has to compensate the differences in sensitivity of the quadrants as well as the gain variations in the readout electronics. The calculation of the position requires some computing power which made it impossible to use it as an online tool.

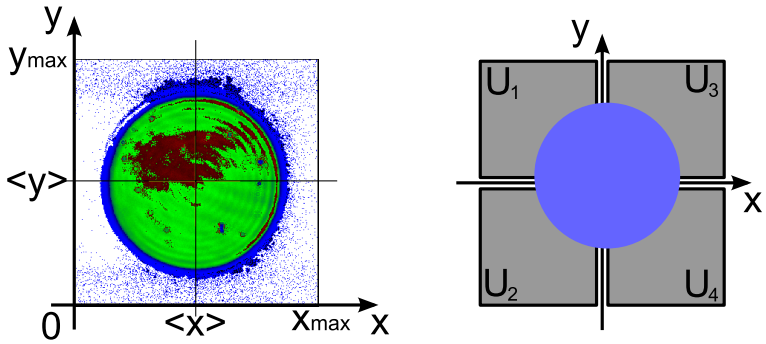

Figure 3.19: *Illustration of the working principle of the quadrant diode. Left: Transverse laser pulse shape measured by a CCD camera incl. its coordinate system. Right: Parts of the laser beam (blue) hitting each quadrant generate voltages according to their respective intensities.*

In figure 3.19 the working principle of the position retrieval algorithm is shown. The laser pulse impinging on the QD, generates voltages in each quadrant ($U_1 ... U_4$). The ratios

$$R_x^{QD} = \frac{(U_3 + U_4) - (U_1 + U_2)}{U_1 + U_2 + U_3 + U_4} \text{ and } R_y^{QD} = \frac{(U_1 + U_3) - (U_2 + U_4)}{U_1 + U_2 + U_3 + U_4} \tag{3.2}$$

give information about the horizontal and vertical position, respectively. When the laser beam is exactly in the center of the QD, both ratios are zero. To relate R_x^{QD} and R_y^{QD} to real positions, they must be compared to the corresponding ratios obtained from the transverse laser profile measured by a CCD camera. With x_{max} and y_{max} being the total number of pixels of the CCD chip in x- and y-direction, respectively, $p(x, y)$ the pixel value at position (x, y) and g the gap width of the QD, the ratio for x-coordinate reads

$$R_x^{CCD}(x_i, y_i) = \frac{\left(\sum_{y \notin \left[y_i - \frac{g}{2}; y_i + \frac{g}{2}\right]}^{y_{max}} \sum_{x=0}^{x_i - \frac{g}{2}} p(x, y) \right) - \left(\sum_{y \notin \left[y_i - \frac{g}{2}; y_i + \frac{g}{2}\right]}^{y_{max}} \sum_{x=x_i + \frac{g}{2}}^{x_{max}} p(x, y) \right)}{\sum_{y \notin \left[y_i - \frac{g}{2}; y_i + \frac{g}{2}\right]}^{y_{max}} \sum_{x \notin \left[x_i - \frac{g}{2}; x_i + \frac{g}{2}\right]}^{x_{max}} p(x, y)}. \tag{3.3}$$

In this formula, it is assumed that the center of the quadrant diode is located at the (camera-) pixel-coordinates (x_i, y_i). Using this together with the corresponding equation for $R_y^{CCD}(x_i, y_i)$, it is possible to retrieve the real pixel-coordinates of the laser spot on the QD by finding x_i and y_i for which

$$R_x^{QD} = R_x^{CCD}(x_i, y_i) \text{ and } R_y^{QD} = R_y^{CCD}(x_i, y_i) \tag{3.4}$$

is true. Finally, the positions are obtained by scaling x_i^{laser} and y_i^{laser} with the pixel size of the used CCD camera. For this reason, the accuracy of the position retrieval is limited to these pixel dimensions.
For more information about the quadrant diode used at PITZ see [Ivan01].

3.4.5 High-speed camera

A new diagnostics tool (PCO dicam pro camera) has been installed and commissioned very recently. A so-called intensified CCD camera is capable of measuring most of the laser pulse properties at the same time for a defined pulse inside the train. In figure 3.20 the basic physical layout of this camera is depicted. The laser light impinging on a photocathode[18] creates electrons which are accelerated towards a multichannel plate

[18]The photocathode material was chosen to be S-20 (Na_2SbK:Ce) for its high sensitivity at the wavelength of the laser

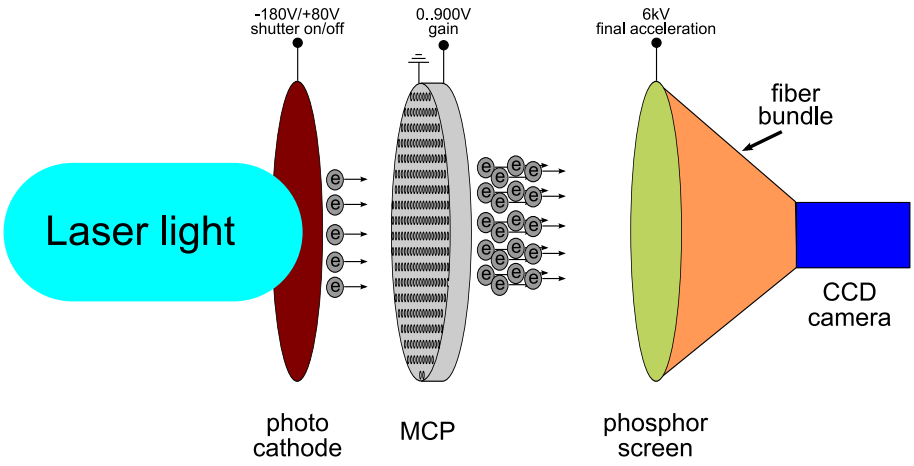

Figure 3.20: *Sketch of the internal setup of the PCO camera.*

(MCP) as long as an accelerating voltage is applied. Switching this voltage is used to provide a fast shutter. The multiplication factor of the MCP can be controlled by varying the voltage across the MCP between 0 and 900 V. In a next step, the generated electrons are further accelerated by a voltage of 6 kV towards a phosphor screen[19] which then emits visible light having an intensity proportional to the electron number. Using a tapered fiber bundle, this light is transported to a CCD chip[20] which records the image. The final effective pixel size is 14.5 μm x 14.5 μm. In contrast to normal CCD cameras, the minimum shutter time is not determined by the readout characteristics of the CCD chip but rather by the switching speed of the voltage between the photocathode and the MCP. In the case of the PCO camera used at PITZ, this time is 30 ns.

Choosing a shutter time shorter than the laser pulse repetition time and setting an appropriate trigger, a particular laser pulse within the pulse train can be picked out. Taking measurements over many laser pulse trains, properties like position and position jitter, beam size and beam size jitter and finally the energy stability by recording the sum of pixels can be calculated for a particular laser pulse in the train.

3.4.6 Diagnostics setup

In the previous sub-chapters, the individual measurement devices were presented which is now followed by an introduction of the actual laser diagnostics setup.
Wherever possible, the diagnostic devices are available in the laser hut as well as in the accelerator tunnel to have a direct comparison between intrinsic pulse properties

[19] The phosphor screen material was chosen to be P-46 (YAG:Ce) because of its short decay time of 200-400 ns (100% - 10%)

[20] This chip has a resolution of 1280 x 1024 and a dynamic range of 1:4096 (12 bits)

originating from the laser and properties which are introduced by the transport to the photocathode, position changes induced by air-flow, for example.
In figure 3.21(a) the diagnostics installation in the laser hut is shown. Here, a part of the laser light is coupled out of the main beamline by means of a wedged quartz plate. The front and the back side of the wedge reflect approx. 4 % of the total laser pulse energy each. These reflections are used for the two separate diagnostics beamline.
The laser pulse energy of every pulse inside a train is measured using a PMT. In addition, a power meter is installed which measures the total output power of the laser. To be within the measurement range of the power meter, some hundred laser pulses are needed. For this reason, individual laser pulse energies cannot be measured.

Furthermore, it is possible to measure the transverse distribution of the laser pulse by means of a CCD camera. An appropriate beamline has been installed to provide imaging of the laser object plane onto a camera with unit magnification (near-field camera). A second camera of the same type measures the corresponding far field distribution of the laser pulse (far-field camera). Finally, a quadrant diode delivers position and position jitter information.
The setup of the laser diagnostics in the accelerator tunnel is depicted in figure 3.21(b). Two cameras (virtual cathodes, VC) are installed for the observation of the transverse laser pulse distribution. VC2 can be used on demand by inserting a movable mirror into the main laser beam path. Therefore, the full laser pulse is reflected to the camera limiting

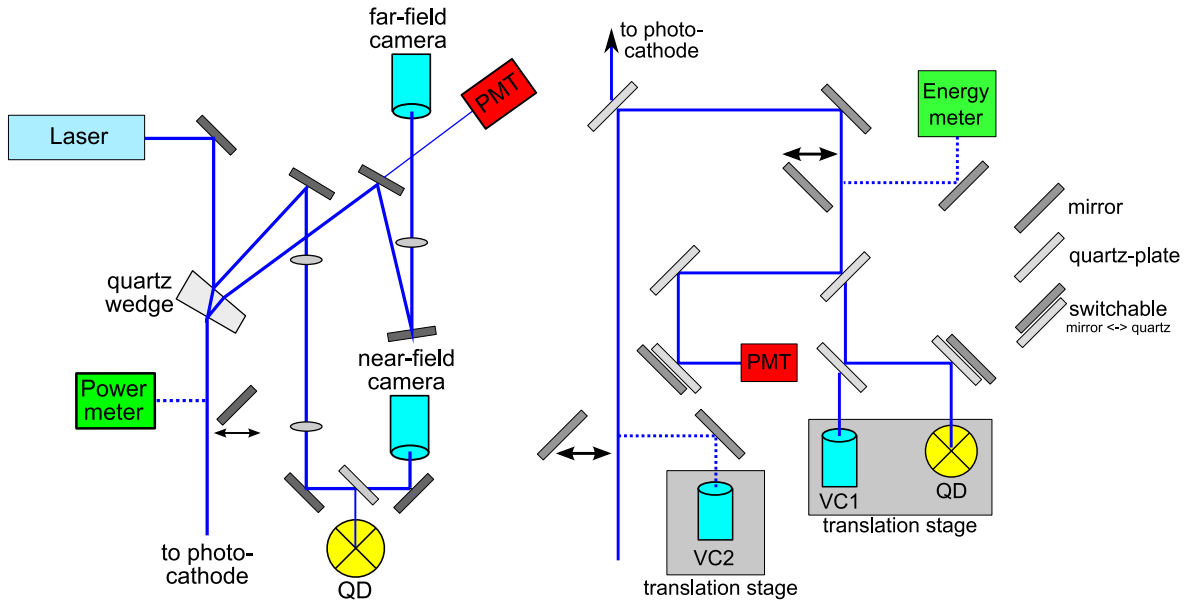

(a) *Diagnostic devices in the laser hut.* (b) *Diagnostic devices in the tunnel*

Figure 3.21: *Sketches of the diagnostics beamlines (not to scale).*

its use to the low-intensity regime. In contrast, VC1 is illuminated by the permanent reflection from a fixed quartz-plate (see figure 3.21(b), top left). Since the reflection coefficient is of the order of a few percent, this camera is used in the high laser intensity regime only. A PMT and a quadrant diode are used to measure the energy and the position of the laser pulses. To yield an absolute information about the laser pulse energy, a calibrated, commercially available photo diode can be used on demand by inserting a mirror. The complex combinations of reflections from mirrors and quartz-plates shown in figure 3.21(b) is necessary to match the laser pulse energy to the measurement ranges of the diagnostic devices. Finally, it is possible to change the position of the laser spot on the cameras and the quadrant diode without changing the position of the laser on the photocathode by means of translation stages.
At last, the high-speed camera, introduced in subsection 3.4.5, is also installed in the accelerator tunnel but not shown in figure 3.21. It is placed at an image plane position behind the last mirror of the optics beamline in the tunnel, see figure 3.10.

3.5 Summary

In this chapter, the laser, the laser beamline and the available laser pulse diagnostics were introduced. The installed diagnostics allows to observe all relevant laser pulse properties, i.e. the laser pulse energy, the temporal and transverse shape as well as the position. Recording the pulse energy and position is possible for each pulse within a train using a photomultiplier tube and a quadrant diode. For the measurement of the temporal shape using the OSS some hundred pulses are needed, whereas the transverse shape is usually measured for the first pulse in a train only using CCD cameras. Finally, the high-speed camera allows to do dedicated investigations on a chosen pulse within a train using an appropriate trigger and a shutter time shorter than the temporal spacing of the laser pulses. This shows that plenty of information about the laser pulses generating the electron bunches is gathered but a full characterization of each pulse within a train is not yet possible.
In the next chapter, dedicated measurements will be presented to characterize the laser and the laser beamline using the diagnostic tools that were introduced here.

Chapter 4

Measurement of laser pulse properties

In this chapter, dedicated measurements will be presented which were performed to characterize the laser and the laser beamline. These are firstly, a comparative study of the temporal shape measured by the Optical Sampling System and the Hamamatsu FESCA200 streak camera. Secondly, the streak camera was used to study the influence of the complete laser beamline up to the photocathode on the temporal laser pulse shape. For this purpose, the streak camera measurements took place in the tunnel at the (virtual) position of the photocathode and immediately afterwards in the laser hut. The next investigation compared the temporal laser shapes of different pulses within the laser pulse train. Afterwards, measurements are presented which investigate the dependence of the temporal laser profile on the transverse position. While in the fifth part the effect of thermal lensing in the laser system is studied under various conditions, the topic of the final section is the laser spot size at the position of the inner vacuum mirror (see figure 3.10). At this position, the laser beamline has the strongest space restrictions. In addition, since there is no imaging plane, diffraction patterns occur which increase the total beam span. In case parts of these diffraction patterns are clipped one would expect a deterioration of the laser spot transverse distribution at the position of the photocathode. In

4.1 Comparison between the Optical Sampling System and the FESCA200 streak camera

In this sub-chapter, investigations of the precision of the Optical Sampling System will be presented which require another, completely independent measurement system. For this purpose, the streak camera Hamamatsu FESCA200 [Hama01] was used. At the laser wavelength of about 260 nm, this streak camera has a resolution of approx. 800 fs [Tomiz] which is comparable to the resolution of the Optical Sampling System. The advantage of the FESCA200 streak camera over the Optical Sampling System is its single-shot measurement capability. On the other hand, the measurements obtained with the streak

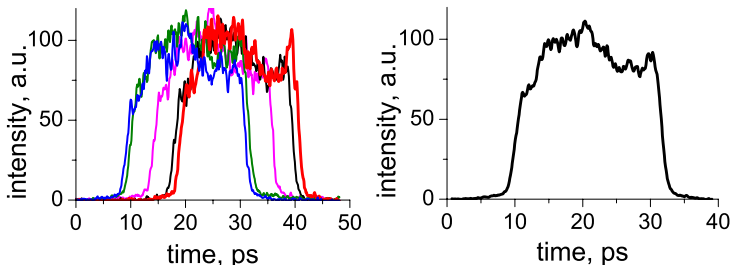

Figure 4.1: *Comparison between single shot measurements (left) and averaged data (right) using a Hamamatsu FESCA200 streak camera.*

camera have a low signal-to-noise ratio (see chapter 3.4.1). While many other streak cameras overcome this problem by applying the so-called synchroscan technique, i.e. a synchronized overlap of many single shots by the streak camera, this is not possible with the FESCA200. The reason is, that the voltage needed for the transverse deflection of the electrons is swept linearly, whereas the synchroscan technique requires a sinusoidal voltage modulation. The internal trigger jitter for the linear voltage ramp amounts to about 20 ps [Hama01]. Thus, the averaging cannot be done automatically by the streak camera, but is left to the post-processing stage. As an example, figure 4.1 shows five individual measurements and the resulting averaged signal.

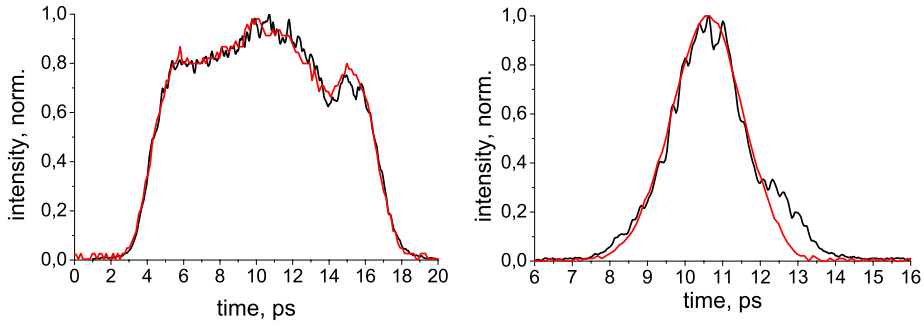

Figure 4.2: *Comparison between FESCA200 (black) and OSS (red) measurements for a 12 ps (FWHM) almost flat top pulse and a 2 ps (FWHM) Gaussian pulse, respectively. Note, that the displayed streak camera measurements were obtained by averaging five individual measurements.*

Because of the low signal-to-noise ratio of single-shot streak camera measurements, all temporal profiles presented hereafter show the average of five individual measurements. To compare the results obtained with the Optical Sampling System and the streak camera,

different temporal pulse shapes were measured using both devices. Figure 4.2 shows the results for a long pulse of about 12 ps duration (FWHM) (left) and a short Gaussian with 2 ps duration[1](FWHM) (right). Despite the small shoulder appearing in the streak camera measurement on the right-hand side, the origin of which is not clear, the results are very similar.
This leads to the conclusion, that the measurements made with the OSS are comparable to the results obtained with an independent device having a similar temporal resolution.

4.2 Invariance of the temporal laser profile upon transport through the laser beamline

The optical elements of the laser beamline (lenses, beam splitters, etc.) can have a detrimental influence on the temporal laser pulse shape. The best known effect is the linear dispersion, meaning different wavelengths contained in the laser pulse have a different phase velocity in matter leading to a deformation of the temporal laser shape. Since the spectral bandwidth of the laser pulse is very small (of the order of $\Delta\lambda_{FWHM} \approx 0.035$ nm), the expected deformation is imperceptibly small. Another possible effect is the nonlinear self-phase modulation. This, however, is a third-order nonlinearity and therefore strongly dependent on the laser pulse intensity. The laser pulse energy is too small to cause such effects. However, unexpected behavior like material imperfections of the optical elements can occur which are not known in the first place.

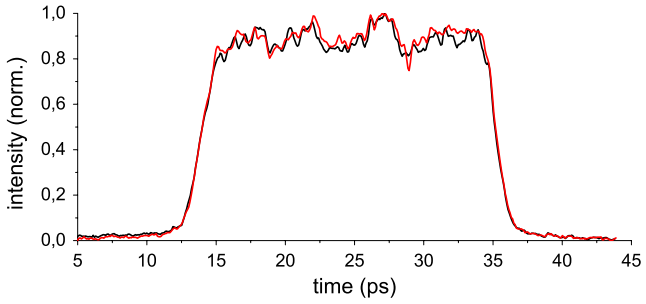

Figure 4.3: *Comparison between temporal laser pulse shapes measured in the laser hut (black) and in the tunnel (red).*

Therefore, the influence of the complete laser beamline on the temporal laser shape was investigated by performing measurements with the streak camera in the tunnel at an equivalent cathode position. The laser beamline up to the streak camera contained all elements which are also present in the actual laser beamline to the photocathode, like

[1]For this measurement the laser pulse shaper was removed

wedge plates, beam splitters, vacuum entrance window and inner vacuum mirror. Immediately after the measurement in the tunnel, the streak camera was transported to the laser hut and the output of the laser system was measured there. In figure 4.3, both measurements are displayed. Within the noise level of the streak camera, these temporal shapes are identical. The laser beamline does not affect the temporal laser distribution.

4.3 Invariance of the temporal laser pulse shape along the laser pulse train

The measurement of the temporal profile of the laser pulses using the Optical Sampling System requires long pulse trains of usually 550 pulses. All of these pulses are assumed to be identical. To prove this, the FESCA200 streak camera was used to measure individual pulses in a train of 40 pulses which is the maximum number that is usually used for emittance measurements. In addition, the lower number of laser pulses assures that the load on the photocathode of the streak camera is kept in reasonable limits.
Figure 4.4 shows the averaged temporal profiles for different pulses in the laser pulse train. Despite the noise on the temporal profiles and the fact that the intensity for the measurement of the 15th pulse is slightly lower, these temporal laser can be considered to be equal.

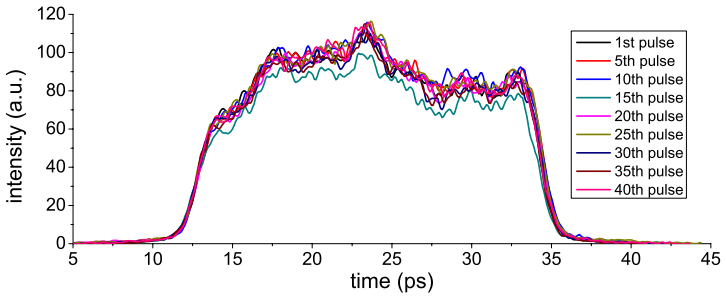

Figure 4.4: *Comparison of the averaged temporal laser pulse shapes within the pulse train measured with the streak camera at an equivalent photocathode position.*

4.4 Spatial dependence of the temporal laser shape

The temporal laser shape depends on the transverse position inside the laser beam. This behavior results, for example, from an angular dependence of the spectral acceptance during the frequency conversion process in the nonlinear crystals. To avoid detrimental effects for the extracted electron bunches, only the central part of the transverse laser

distribution is used (cutting by Beam Shaping Aperture).
In order to investigate how pronounced these effects are, measurements were done using the streak camera. To include also the effects of the laser beamline, the streak camera was placed in the accelerator tunnel at an image plane position. The entrance slit (width about 30μm) of the streak camera was used as spatially selecting element to measure the temporal shape of the laser beam at five transverse positions. The results are depicted in figure 4.5. On the left side, the transverse shape of the full beam[2] is shown as it was recorded with the streak camera in focus mode [Hama01]. The magenta lines indicate the positions at which the temporal laser shape was determined. On the right side, the corresponding temporal shapes are shown.
From the graphs depicted in figure 4.5(b) can be concluded that a transverse dependence of the temporal laser pulse shape exists. Since only the center part of the transverse distribution is used in the electron beam experiments, this dependence cannot be noticed in practice.

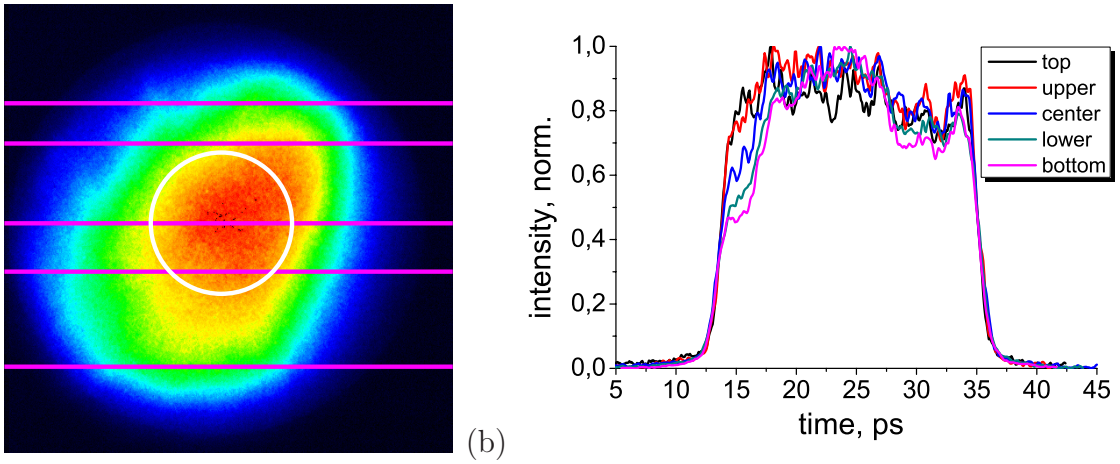

Figure 4.5: *(a) Image of the full laser beam used for the measurement. The white circle has a diameter of approx. 1.5 mm and indicates the part which is typically transmitted by the BSA.*
(b) Temporal profiles measured at the positions indicated by the magenta lines in the left figure.

[2]The Beam Shaping Aperture was removed.

4.5 Investigation of thermal lensing

Introduction to thermal lensing

Every optical material has a refractive index which not only depends on the wavelength of the light but also on the temperature of the material $n = n(\lambda, T)$. This dependence is usually expressed as a derivative $\frac{dn}{dT}$ at a given temperature. In the case of a laser material, this temperature dependence can have a negative influence on the beam propagation because the pump light used to excite the atoms is usually not transversely homogeneous. Therefore, the heat load on the crystal induced by the pump light and, as a consequence, the temperature distribution[3] has a spatial dependence. In the amplifier stages of the laser system, YAG is used as a host crystal which has $\frac{dn}{dT} = 9 \cdot 10^{-6}\mathrm{K}^{-1}$ at room temperature [Chen]. Since this value is positive, the center part of the pump light distribution has a higher refractive index and thus the velocity of light is lower than in the outer parts. Thus, the laser pulses passing this refractive index distribution in the crystal experience a focusing effect which is known as thermal lens [Koech] and illustrated by figure 4.6. The strength of the focusing changes along the laser pulse train because, within the train, the laser crystal is continuously pumped causing an increase of the temperature. After passage of the laser crystal, this leads to a change of the transverse laser beam size along the train which, in turn, can cause additional, secondary effects like, for example, a changed gain of a subsequent laser amplification stage.

To avoid the mentioned consequences for the laser pulses, the optics of the laser transport system must be designed in such a way that the image planes are placed at the positions of

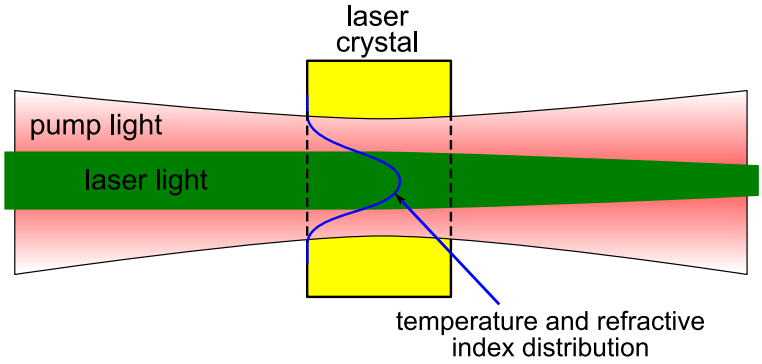

Figure 4.6: *Sketch showing the generation of the thermal lens inside a laser medium. The pump light (red) has a spatial distribution close to Gaussian which causes a corresponding distribution of the refractive index. This results in a lens-like effect which depends on the pump power and the pump duration.*

[3]The actual, transient temperature distribution depends on many material parameter, e.g. quantum defect, absorption cross section, heat capacity, heat conductivity and many more

the potential thermal lenses. In addition, the imaging from the laser to the Beam Shaping Aperture as well as the subsequent imaging on the photocathode must be carefully aligned. If this condition is fulfilled, the change of the beams divergence by the thermal lens does not affect the beam size in the next image plane. Thus, the laser pulse properties remain constant along the train. Even though the alignment of the laser beamline was done very carefully, a remaining impact of the thermal lens on the laser pulse properties at the position of the photocathode cannot be excluded.

Measurement setup

To quantify the thermal lensing effect, the PCO camera was placed at a position at which the optical path length to the photocathode and the PCO camera were identical. During the measurements, the PCO camera recorded images of the transverse laser profile (ten profiles for every tenth pulse in a pulse train of 850 pulses). These images were used to extract the laser beam position, size and intensity[4] and the corresponding variations which are shown in the graphs of figures 4.7 and 4.8 as rms error bars. In addition, the photo-multiplier tube (PMT) in the laser hut was used to measure the laser pulse energies emitted from the laser system. The PMT signals were sampled using a fast ADC. Its sampling frequency was 1 MHz which allowed to measure the energy of every pulse within the train. Since the sampling of the ADC was triggered to begin before the emission of the laser pulse train started, the first pulse appears at channel no. 699. Here, 100 measurements were taken to retrieve the average and jitter values. The error bars appear as gray band in the figures because the point density is too large to resolve them individually.
One specialty of the laser beamline must be mentioned. To spatially clean the laser pulses and thus remove imperfections from the transverse distribution, an iris of variable diameter is placed on the laser table (not at an image position). This iris as well as the Beam Shaping Aperture in the tunnel are distorting the measurements of the thermal lensing because they are cutting large parts of the distribution. In reality, this can have positive and negative effects, for example a movement of the beam before the Beam Shaping Aperture will only result in a small change of the center of gravity of the transverse distribution but at the same time the total transmitted laser energy can vary significantly.

Measurements and results

In order to analyze the influence of the mentioned laser beamline elements, the following sequence of the measurements was chosen. At first, the nominal measurement setup was used, meaning the Beam Shaping Aperture of 1.5 mm diameter was inserted and the iris in the laser hut was closed to get a good transverse profile. In the second measurement, the BSA was removed and in the subsequent, third measurement, also the iris in the laser

[4]Measured as sum of pixels

hut was fully opened. Finally, the pump light intensity of the last amplification stage and therefore the heat load on the laser crystals was reduced to see the change of the thermal lensing. This was done by decreasing the current of the pumping diodes from 24 A (nominal value) to 18 A. These measurements were performed in the short-pulse mode (the pulse shaper was removed) and the laser pulse duration was about 2.5 ps (FWHM). For the last measurement, the pulse shaper was inserted again and a 24 ps flat-top profile was produced to see the thermal lensing effect under low-emittance measurement conditions.
In figure 4.7(a), the results for the first measurement (with BSA and closed iris) are shown. The center position of the laser beam did not change significantly, the same is true for the beam sizes which change only by about 10 μm. The laser intensity, however, dropped to about 40 % from the first pulse towards the end of the laser pulse train.
Figure 4.7(b) shows the results with the BSA being removed. In this case, the position does not change significantly but the beam size increases by about 15 % along the train while the intensity drops to 60 %. This result is in agreement with the first measurement because inserting the BSA masks the effect of the increasing beam size but the drop in intensity is more severe.
In figure 4.7(c), the results are depicted for the case of an open iris. Now the laser beamline does not clip the laser pulse transversely (vignetting). The complete laser pulse energy emitted by the laser is transported to the PCO camera. This can be seen by comparing the measured intensities of the laser hut PMT and the sum of pixels from the PCO camera.
The laser pulse position does not change significantly but the beam size decreases by about 5 % in x-direction and about 10 % in y-direction. This means that the effect of thermal lensing is still present.
The last graph of figure 4.7 shows the results for the pumping diode current of the booster amplifier changed from 24 A to 18 A. The currents of the pumping diodes for the double-pass amplifier, the regenerative amplifier and the oscillator remained unchanged. This was done to reduce the heatload on the crystal and therefore the thermal lens effect. However, the change of the pumping current resulted in a rising slope of the laser pulse energy along the laser pulse train. This had to be compensated by adjusting the timing characteristics of the pump diodes of the double-pass amplifier such that the pumping of the laser crystal starts 100 μs earlier. From figure 4.7(d) it becomes evident that the consequent increase of the heat load on the laser crystal of the double-pass amplifier counteracts the reduction of the heat load on the booster amplifier. The beam size in x-direction increases by 19 % and in y-direction by 7 % while the laser intensity along the train drops by 23 %.
These results show that the thermal lens effect is present in the booster as well as in the double-pass amplifier. It cannot be reduced by simply decreasing the pumping diode output power of one of the final amplifier stages.

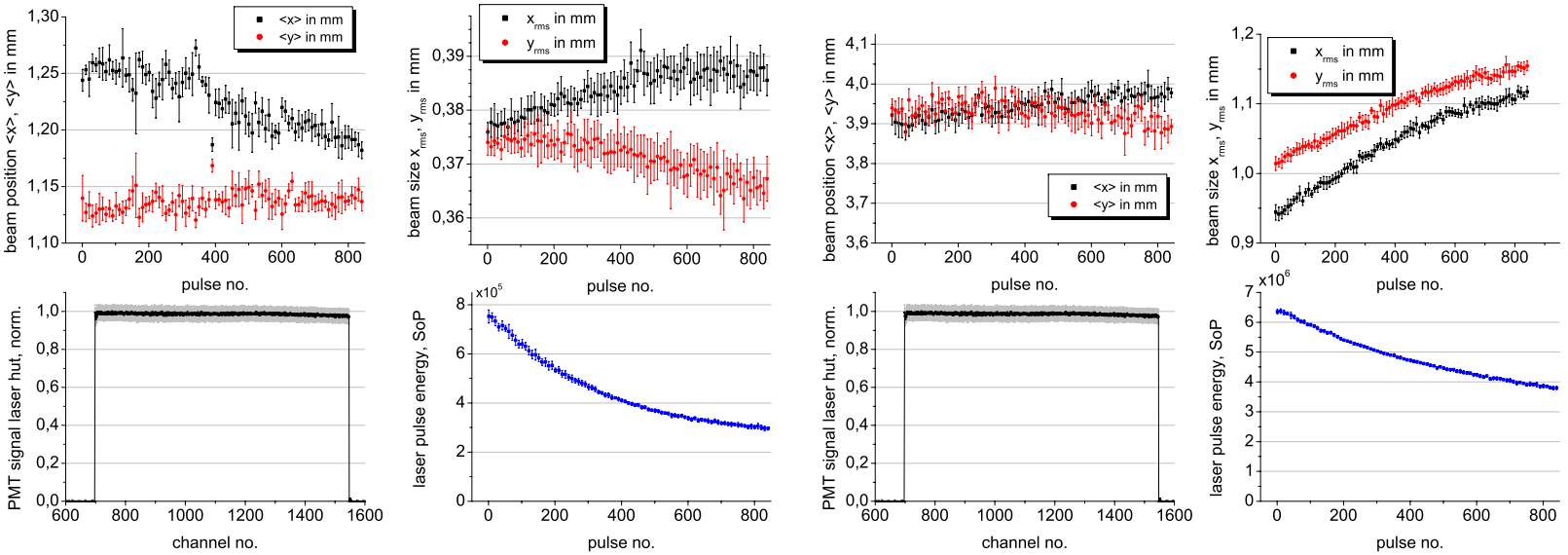

(a) *With Beam Shaping Aperture, with iris*

(b) *Without Beam Shaping Aperture, with iris*

(c) *Without Beam Shaping Aperture, without iris*

(d) *Reduced pump power, without Beam Shaping Aperture, without iris*

Figure 4.7: *Results of the measurements on thermal lensing with pulse duration 2.5 ps.*

Finally, the same measurement was performed for the nominal case of a flat-top temporal pulse shape with 24 ps duration (FWHM) and 2 ps rise and fall times. In this regime, the default setting of the pumping diode currents is 27 A. The results are depicted in figure 4.8. While the position of the laser beam remains almost the same, the beam size

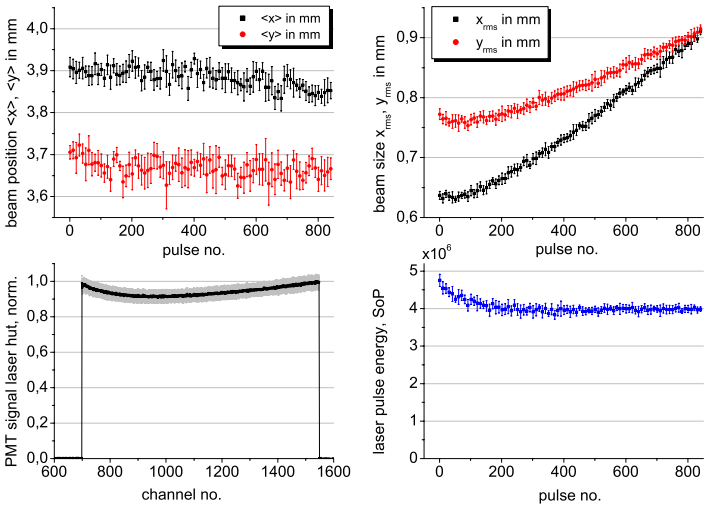

Figure 4.8: *Results of the measurements on thermal lensing with flat-top temporal shape and a pulse duration of 24 ps. The BSA was removed and the iris in the laser hut is open.*

changes significantly. In horizontal direction, the beam size increases by 44 % whereas in vertical direction the increase amounts to 20 %. Within the first 200 pulses of the train, an intensity drop can be observed on the PMT in the laser hut as well as on the PCO camera in the tunnel. However, the subsequent rise of the laser pulse intensity measured with the PMT cannot be observed with the PCO camera.

These measurements showed that the negative consequences of thermal lensing present in the laser system are not suppressed by an appropriate relay imaging between the components mentioned in the introduction. Furthermore, the effect of thermal lensing results in a change of all measured laser beam properties along the pulse train. The performed measurements did not allow to reveal which elements of the laser beam transport are not properly aligned.
In addition, the PMT measurements show that the rms laser energy jitter averaged over the whole train is 3.7 %. After installation of the laser system at PITZ, a similar measurement was done which resulted in an rms energy jitter of about 0.6 %. This might be an indication for an aging effect of the laser oscillator.

4.6 The beam size at the vacuum mirror

The measurement of the actual laser spot size at the position of the inner vacuum mirror (see figure 3.10) is of particular importance. Since this mirror is the smallest part of the whole laser beamline, parts of the laser pulse may be clipped or not reflected. This would lead to a degradation of the transverse laser profile at the photocathode. Note, that no imaging plane is located at the position of the vacuum mirror and thus, the transverse size of the laser beam is larger than the used BSA diameter due to diffraction. In figure

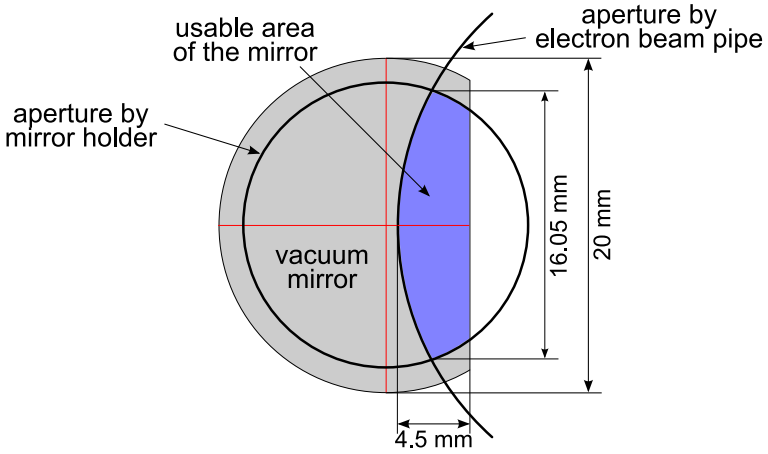

Figure 4.9: *Sketch of the inner vacuum mirror as seen from the photocathode. The actual usable area on the mirror is marked blue. Note that horizontal dimensions are projected lengths of the mirror tilted by 46 degrees. The real length on the mirror surface is about 1.41 times larger. For precise technical drawings see Appendix C.*

4.9, the actual dimensions of the vacuum laser mirror are depicted. It shows that the transverse size of the laser spot at this position must be smaller than 2 mm. This number takes into account that during measurements of quantum efficiency maps [5](QE maps) the laser beam is scanned over the whole photocathode using the wedge plates. Since the photocathode has a diameter of 5 mm, the laser beam excursion in each direction is 2.5 mm from the center. Further, the distance wedge plates - photocathode is about twice the distance wedge plates - inner vacuum mirror. Thus, about 1.25 mm need to be subtracted from the vacuum mirror size in all directions to get the maximum allowable transverse size of the laser beam at the position of the inner vacuum mirror.
The measurements were done in the accelerator tunnel close to the actual position of the vacuum mirror. Using another mirror, the laser light was directed towards a camera in front of the laser entrance view port.

[5]Measurement of the position-dependent quantum efficiency of the photocathode

In figure 4.10, the measured transverse profiles are depicted for a BSA diameter of 1.5 mm, which was used when the smallest emittance at a charge of 1 nC was measured, and for a diameter of 0.2 mm, which is the smallest size used for the QE maps. This is important because the use of small BSA openings potentially causes large diffraction patterns during the transport to the photocathode.
From these images, one can conclude that the beam size at the vacuum mirror exceeds the 2 mm limit only in the case of very small initial beam diameters. But even in this case, the pulse energy contained in the clipped parts of the laser beam is rather small. However, there is no tolerance to misalignments. For this reason, a re-design of the vacuum mirror is suggested. As an alternative solution, the last mirror in the beamline can be used together with the wedge plates to steer the laser beam on the photocathode keeping its position on the vacuum mirror constant.

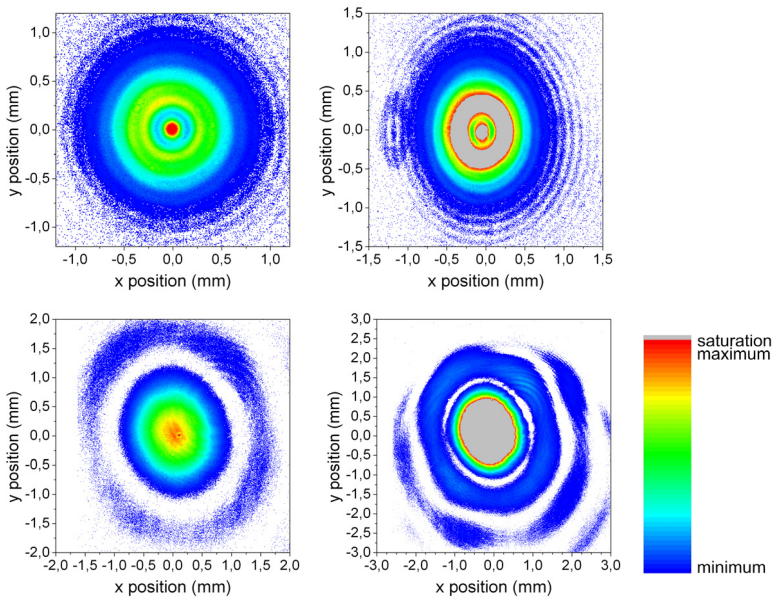

Figure 4.10: *Measured transverse laser profiles at the position of the inner vacuum mirror for two diameters of the Beam Shaping Aperture: 1.5 mm (top) and 0.2 mm (bottom). The left images show the actual profile while the right images are intentionally saturated to see the faint higher orders of the diffraction patterns. Note the different scaling of the axes in the lower right image.*

Chapter 5

The electron emission process

The main part of the emittance of an electron bunch is generated during the emission process. For this reason, the aspects associated with the emission are introduced in this chapter.
Three emission mechanisms are relevant for the electron bunch production in accelerators. These are the field emission, the thermionic emission and the photoemission.
Field emission occurs when a material is exposed to a very strong electric field which causes a lowering of the potential barrier at the surface of the material and thus an increased probability of quantum mechanical tunneling of the electrons. In RF photoinjectors, this process leads only to an unwanted current contribution (dark current). Therefore it is not further discussed. For more information on this topic see [Han].
A second process of charge production is the thermionic emission. It is based on the heating of the cathode material until a sufficiently large part of the high-energy tail of the electron density distribution inside the material exceeds the surface potential barrier. These high-energy electrons can escape into the vacuum and produce the electron beam upon acceleration. This emission process is used for example at SCSS, Japan [SCSS], or at MaxLAB, Sweden [MAXlab]. A review on thermionic emission can be found in [Modi].
The third process of charge production, which is also used at PITZ, is the photoemission. Upon light illumination, electrons inside the material are excited to energy levels which are appropriate to overcome the surface potential barrier and are therefore emitted. This process is possible in metals (e.g. copper) and semiconductors (e.g. GaAs or Cs_2Te). The electron bunch production using photoemission has proven to provide beams of highest quality so far. The main reason is the possibility to influence the electron bunch properties by changing the transverse and temporal parameters of the laser pulse which is used for the extraction. The choice of the photocathode material is influenced by several parameters, for example the quantum efficiency, cathode lifetime, robustness to poor vacuum conditions and the efforts associated with the development of a proper laser system. For

PITZ, the best compromise between the given constraints is Cesium Telluride[1].
The following sub-chapters are dedicated to the physics of the photoemission of Cs_2Te. Firstly, the emission process is described in detail. This is followed by the presentation of issues arising from two facts: The space charge fields, which are generated by the bunch itself, are not negligible during the emission and secondly, the emission can be enhanced by a strong electric field at the cathode surface.

5.1 Photoemission in Cs_2Te

According to Spicer [Spic], the photoemission can be described by a three-step model:

1. Excitation of an electron inside the material by absorption of a photon
2. Migration of the electron towards the surface
3. Electron emission across the surface potential barrier

The absorption takes place in the Cs_2Te-layer which has a thickness of 20-30 nm [Lede01] and is deposited on a Molybdenum plug. Since the photon absorption length is less than 20 nm, most of the photons promote electrons to the conduction band. These electrons move randomly inside the photocathode layer. Since the electron density in the conduction band of the semiconductor is very low, the probability of collisions between electrons is little. Therefore, the electron escape length can be of the order of μm allowing almost all electrons to escape [Han]. In addition, the movement towards the surface can be supported by an external electric field.
The time the electrons need to travel to the surface defines the photocathode response time. Due to the small absorption length, the photoelectrons are excited close to the surface. Therefore, one would expect the response time to be very short. Dedicated measurements do not exist but estimates range from 0.5 ps to less than 2 ps, which was justified by experimental observations.
To obtain a better insight into the photoemission process, the band structure of Cs_2Te as measured by Powell et al.[Pow] is depicted in figure 5.1. The excitation of electrons from the valence band to the conduction band requires photon energies of at least $E_{\text{photon}} = 3.3\,\text{eV}$ which is equal to the band gap. The density of states at the initial and final energy level is very low in this case making the transition very inefficient. Furthermore, these electrons could not escape into the vacuum because they need to overcome the surface potential barrier. This energy difference from the lower conduction-band edge to the

[1] Another widely used photocathode material is copper. Its advantage is the resistance against poor vacuum condition which makes the handling easy, but the disadvantage is the low quantum efficiency of the order of $10^{-5} - 10^{-4}$. GaAs can provide electron bunches with a very low cathode emittance (see chapter 6.2.1) but requires vacuum pressures in the range of $10^{-11} - 10^{-12}$ mbar which cannot be maintained in RF gun cavities.

vacuum level is called electron affinity and amounts to $E_A = 0.2\,\text{eV}$ in the case of Cs_2Te. For an efficient electron excitation, photon energies are used which allow the transition between the density of states maxima at -0.7 eV and 4.05 eV (indicated by a blue arrow). Thus, the photon energy must be about 4.75 eV, which corresponds to a wavelength of $\lambda = h \cdot c/E_{\text{photon}} \cong 261\,\text{nm}$.

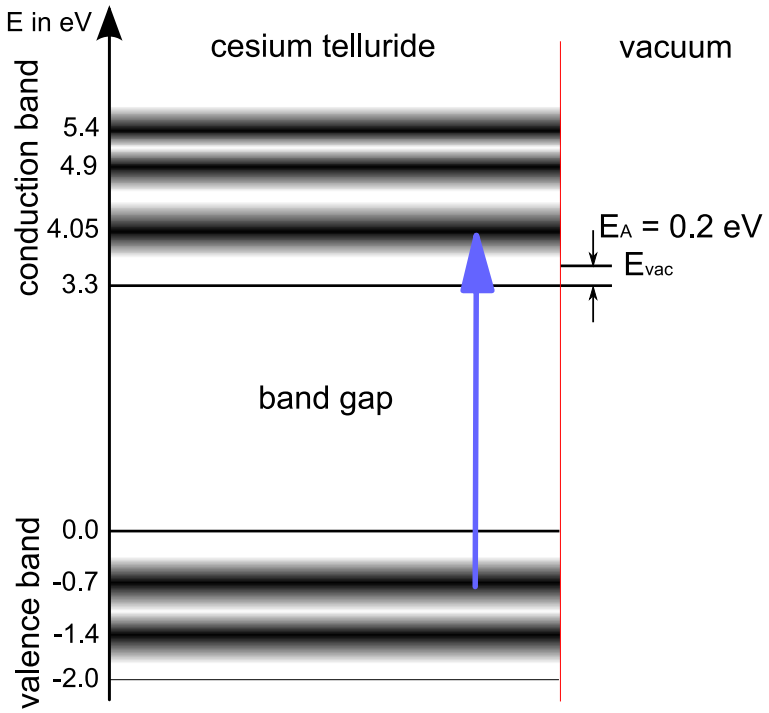

Figure 5.1: *Simplified model of the band structure of Cs_2Te as described in [Pow]*

The excited electrons migrate to the surface and escape into the vacuum. As can be seen in figure 5.1, the final kinetic energy of the electrons is $E_{kin} = 4.05\,\text{eV} - 3.3\,\text{eV} - 0.2\,\text{eV} = 0.55\,\text{eV}$. The angular distribution electron velocities in front of the photocathode give rise to the first contribution to the electron beam emittance, which will be described in detail in section 6.2.1.
Poor vacuum conditions can cause contaminants (like Oxygen or Fluorine) to change the chemical composition of the cathode surface and modify the electron affinity. This has two major effects. Firstly, a change of the kinetic energy of the emitted electrons and secondly, a changed quantum efficiency[2] (QE), which is defined as the number of emitted

[2]The quantum efficiency is between 10 % and 20 % for fresh cathodes and less than 0.5 % for contaminated cathodes

electrons per number of incident photons

$$\mathrm{QE} = \frac{n_{\mathrm{electrons}}}{n_{\mathrm{photons}}}. \tag{5.1}$$

A comparative analysis of the chemical composition of the surface of fresh (high QE) and contaminated cathodes (low QE) was performed by S. Lederer et al. using X-ray Photon Spectroscopy (XPS) [Lede02].

5.2 Field-enhanced emission

From metal cathodes it is known that strong electric fields at the surface can assist the electron emission by lowering the surface potential barrier [Scho]. In figure 5.2, the situation for the so-called Schottky effect is shown. The work function ϕ_{work} is the potential difference between the Fermi level and the vacuum level. Electrons which have energies above the vacuum level can escape the metal. Outside of the material, the electrons experience a potential which is the sum of the mirror charge[3] and the applied electric field. Therefore, the total electric potential energy can be written as

$$e\Phi = e\phi_{\mathrm{work}} - \frac{e^2}{16\pi\epsilon_0 z} - eE_0 z. \tag{5.2}$$

Here, e is the electron charge, ϕ is the potential, $\epsilon_0 = 8.854 \cdot 10^{-12}\ \frac{\mathrm{As}}{\mathrm{Vm}}$ is the permittivity of free space and E_0 is the electric field amplitude. Since the height of the effective

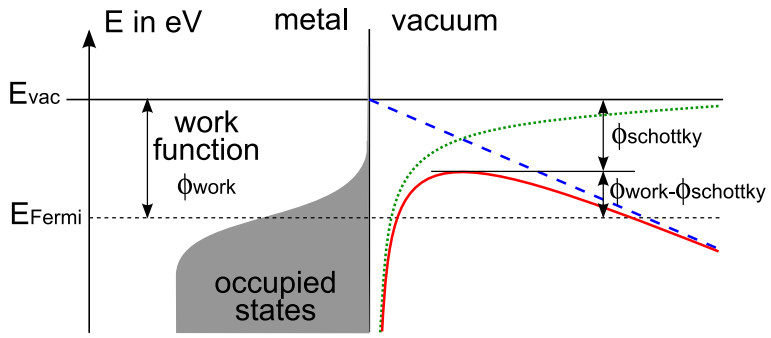

Figure 5.2: *Potential energy barrier near the cathode surface for the case of a metal. The gray area indicates the energy states occupied by electrons according to the Fermi-Dirac distribution The potential caused by the mirror charge is shown in green (dotted line), the applied external field is marked in blue (dashed line) and the resulting potential is marked in red.*

[3]The term mirror charge refers to the fact that electric field lines must be perpendicular to a conducting surface. This can be viewed as a second particle of opposite charge located behind the (planar) surface having the same distance to the surface as the electron itself.

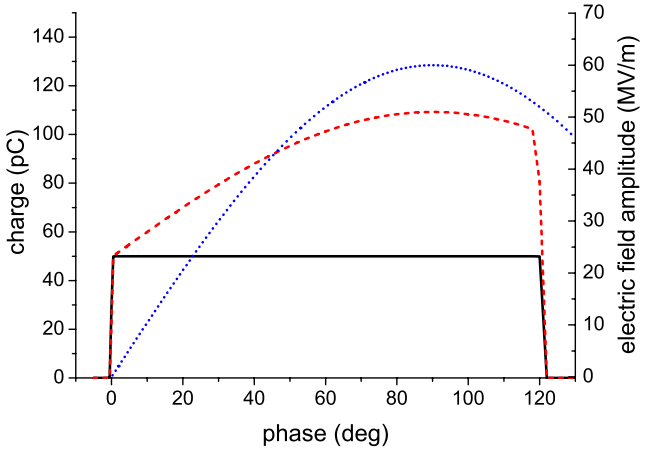

Figure 5.3: *Field-enhanced emission. The electric RF field at the cathode depends on the phase according to* $E_{\mathrm{acc}}(\phi) = 60\,\mathrm{MV/m} \cdot sin(\phi_{\mathrm{RF}})$ *(blue dotted line). The solid black curve represents the extracted charge without field-enhanced emission and the dashed red curve shows the effect of the field enhancement.*

surface potential is lower than in the case without external electric field, more electrons can escape into the vacuum. Since Cs_2Te is not a metal, this model cannot be applied directly. However, a field-assisted enhancement of the electron emission was also observed experimentally. According to [Suber], the electric field-dependent quantum efficiency QE(E) can be expressed as

$$\mathrm{QE}(E) = \mathrm{QE}_0 + k \cdot E_{\mathrm{acc}}(t). \tag{5.3}$$

$E_{\mathrm{acc}}(t)$ denotes the accelerating electric field during emission at the cathode surface which is time-dependent in the case of an RF gun cavity, QE_0 is the quantum efficiency for zero electric field and k ([k]=m/MV) is a constant of proportionality whose actual value depends mainly on the cathode surface morphology [Milt]. In figure 5.3, the influence of the field-dependent quantum efficiency on the extracted charge is shown. This graph was obtained by simulating the emission using the particle tracking code ASTRA [ASTRA]. For this simulation, a charge of 50 pC in combination with a laser spot size at the cathode of 2 mm diameter was chosen (circular flat-top). Furthermore, the laser pulse shape was Gaussian with a duration of 1 ps (FWHM) to pronounce the phase dependence[4].
In ASTRA, the electric field dependence of the quantum efficiency can be modeled by rescaling the charge of the macroparticle during emission according to the equation

$$Q_{\mathrm{macro}} = Q_{\mathrm{macro}}^{\mathrm{initial}} \cdot \left(1 + \frac{k_{\mathrm{Schottky}} \cdot E_{\mathrm{acc}}}{Q_{\mathrm{bunch}}}\right). \tag{5.4}$$

[4]For an RF frequency of $f = 1.3\,\mathrm{GHz}$ a duration of t = 1 ps corresponds to 0.47 degrees of RF phase while the nominal case of 20 ps duration would span 9.4 degrees

In this example, $k_{\text{Schottky}} = 1.0\,\text{pC}\cdot(\text{m}/\text{MV})$ was (arbitrarily) chosen. The influence of the electric field on the emitted charge can be seen from the red curve. The reason for the limited phase range is that below 0 degree the electrons are not accelerated and above 120 degrees the electrons are emitted but meet a decelerating field in the next (full) cell of the gun cavity and are therefore reflected back to the cathode.

5.3 Mirror charge and space charge-limited emission

In the previous section, the term *mirror charge* was already introduced in the context of the potential an emitted electron experiences in front of the cathode surface. This additional electric space charge field is negligible for the emission of a single electron, but at normal operating conditions a charge of 1 nC is emitted, which corresponds to about 6.24 billion electrons. In this situation, it can happen that the electric field produced by the space charge of the bunch compensates the external accelerating field. To estimate the critical charge level, one can use two approaches.

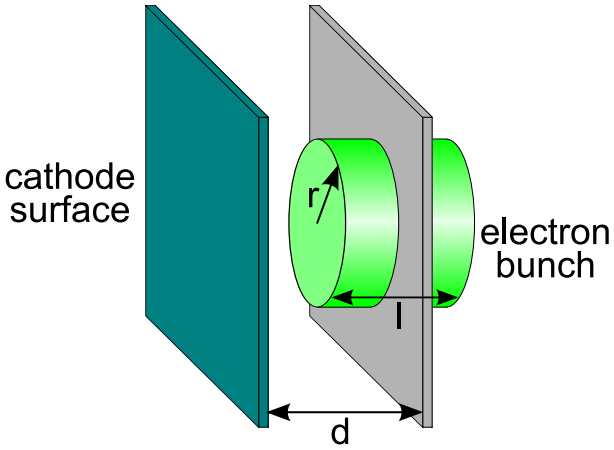

Figure 5.4: *Electron bunch after emission. In the plane sheet capacitor model the charge of the bunch is viewed as being compressed to a thin sheet (gray plane). Together with the cathode surface, it forms a capacitor whose electric field counteracts the external accelerating RF field.*

In the first approach (see Figure 5.4), it is assumed that the electron beam is thin, i.e. the longitudinal extension is much shorter than the transverse radius $l \ll r$. In this case, the emitted electron beam and the cathode surface can be viewed as a plane sheet capacitor. When the beam is close to the cathode surface $d \ll r$, fringe field effects can be ignored and the electric field is calculated using Gauss' law

$$\oint_S \vec{\mathbf{E}} \cdot \vec{\mathbf{n}}\, \mathrm{d}S = \frac{1}{\epsilon_0} \int_V \rho(\vec{r})\, \mathrm{d}^3\mathbf{r}. \tag{5.5}$$

In this equation, $\vec{\mathbf{E}}$ is the electric field vector, $\vec{\mathbf{n}}$ is the surface normal vector and S is the surface of the volume V which encloses the charge density $\rho(\vec{r})$. By integrating over the cylinder's surface one obtains

$$E_z = \frac{\sigma}{\epsilon_0}. \tag{5.6}$$

Here, σ is the surface charge density of the thin bunch. For $E_z = E_{\mathrm{acc}}(t)$, the external electric field is fully compensated and no electron will be accelerated from the cathode surface. For circular flat-top electron bunch of radius r, the maximum extractable charge Q_{max} can be estimated as

$$Q_{\mathrm{max}} = \pi \cdot r^2 \epsilon_0 \cdot E_{\mathrm{acc}}(t). \tag{5.7}$$

The second approach derives the space charge limit by assuming a constant current streaming from the cathode. The limit is expressed in terms of a maximum current density which causes, due to space charge forces, the field at the cathode to drop to zero. This is well known as the Child-Langmuir law [Reis]

$$J = \frac{4}{9} \cdot \epsilon_0 \sqrt{\frac{2e}{m_e}} \cdot \frac{\phi^{3/2}}{d^2}. \tag{5.8}$$

Here, m_e is the electron rest mass, ϕ is the potential difference between the cathode surface and a point at distance d. Please note that in the sheet capacitor model, the maximum extractable charge is proportional to the potential ϕ while in the Child-Langmuir law it scales with $\phi^{3/2}$.
Since the electron bunch is neither a flat sheet nor a constant current, both models can only give an estimate at which charge level space charge forces start to distort the emission. Typical parameters are a bunch duration of 20 ps (flat-top) which corresponds to about 6 mm length, an electron bunch radius of 0.75 mm and a maximum electric field amplitude on the cathode of 60 MV/m. For an RF emission phase of 40 deg, the plane sheet capacitor model predicts a maximum extractable charge of about $Q_{\mathrm{max}}^{\mathrm{PSC}}$=600 pC whereas the Child-Langmuir law gives about $Q_{\mathrm{max}}^{\mathrm{CL}}$=250 pC. In practice, it can be observed that with this parameter combination the space charge effects start to distort the emission at a bunch charge of about 1 nC while it is possible to extract up to about 1.5 nC.

5.4 Summary

In this chapter, the process of photoemission was introduced. It was shown that the electron yield, i.e. the bunch charge, depends not only on the number of incident photons but also on the strength of the applied electric field amplitude. In addition, the emitted charge itself causes an electric field which diminishes the external electric field at the cathode and therefore counteracts the field-enhanced emission. It sets a limit to the maximal extractable charge.

In figure 5.5, the results of a simulation of the interplay between both effects influencing the longitudinal electron beam profile are shown. The simulation was performed using th code ASTRA. The maximum gradient was chosen to be 60 MV/m and the emission took place at the RF phase of maximum mean momentum gain which was about 42 degrees from zero-crossing. The temporal laser shape was 20 ps (FWHM) flat-top with 2 ps rise and fall times and the transverse laser shape was a circular flat-top with 1.5 mm diameter. The initial charge was set to 1 nC. The curves show the longitudinal bunch profile at 25 cm downstream of the cathode, which is outside the gun cavity. For the simulation of the field-enhanced emission, k_{Schottky} was (arbitrarily) chosen to be 5.0 pC·(m/MV).
The black and the red curve show how the field-enhanced emission is increasing the bunch charge from 1 nC (black curve) to 1.16 nC (red curve). The same is true for the green (1 nC) and the blue curve (1.085 nC) but here, the mirror charge reduces the effective accelerating gradient and therefore delays the emission which appears as a longitudinal stretching of the electron beam and a lowering of the beam current.

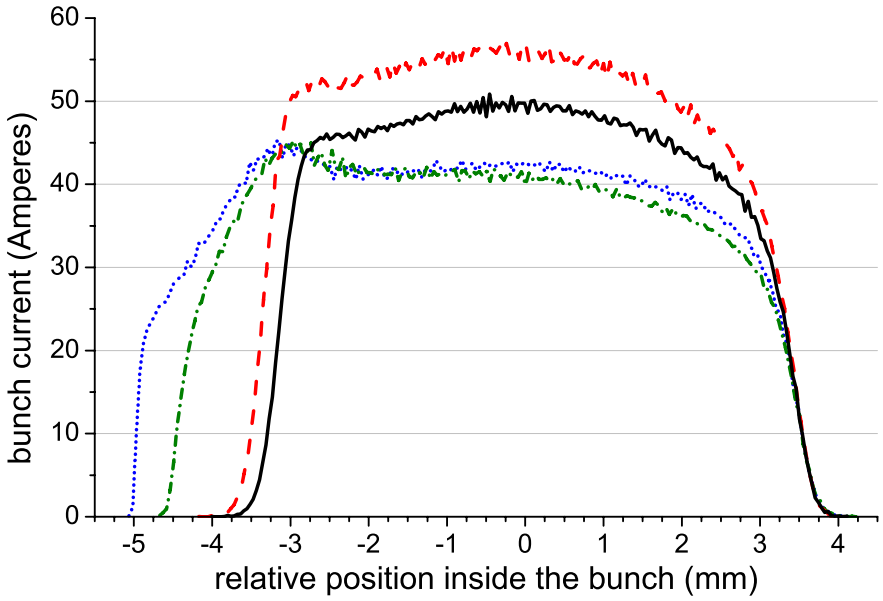

Figure 5.5: *Simulated electron bunch profiles at 25 cm downstream the cathode.*
black solid line: without mirror charge and without field-enhanced emission
red dashed line: without mirror charge and with field-enhanced emission
green dash-dotted line: with mirror charge and without-field enhanced emission
blued dotted line: with mirror charge and with field-enhanced emission

Chapter 6

Electron beam dynamics

This chapter is dedicated to a detailed description of the fundamental electron beam dynamics in a so-called split injector setup. This term refers to injector layouts which consist of a short electron gun cavity, a subsequent solenoid magnet for emittance compensation in the drift space towards the next accelerating structure [Sera]. The sources and the evolution of the transverse emittance along the electron beamline are presented together with a description of the concept of the invariant envelope, which helps to optimize the setup for lowest transverse emittance. This is followed by an introduction to the longitudinal phase space dynamics.

6.1 Phase space representation of the electron beam

The state of one single particle can be fully described by the definition of its coordinate in the six-dimensional phase space composed of the particle's position $\vec{r}$ and its momentum $\vec{p}$

$$\mathbf{u} = \mathbf{u}(\vec{r}, \vec{p}) = (x, p_x, y, p_y, z, p_z)^T. \tag{6.1}$$

During the transport along the accelerator, this particle experiences forces arising from electric and magnetic fields. Electric fields are mainly used to accelerate particles, while magnetic fields steer and focus the beam. The action of the these fields on the particle motion can be described by the Lorentz force equation

$$\vec{\mathbf{F}} = \frac{\mathrm{d}\vec{p}}{\mathrm{d}t} = q \cdot \left(\vec{\mathbf{E}} + \vec{v} \times \vec{\mathbf{B}} \right). \tag{6.2}$$

In this formula, $\vec{\mathbf{F}}$ is the force, q is the charge of the particle, $\vec{\mathbf{E}}$ and $\vec{\mathbf{B}}$ are the electric and the magnetic field strengths, respectively, and $\vec{v}$ is the particle velocity.
An ensemble of particles such as an electron bunch is better described by its six-dimensional phase space density $f_6(\vec{r}, \vec{p})$ according to

$$\mathrm{d}N = f_6(\vec{r}, \vec{p}) \mathrm{d}V_6. \tag{6.3}$$

In this equation, $\mathrm{d}N$ is the number of particles in the infinitesimally small six-dimensional hyper volume $\mathrm{d}V_6$. Alternatively, one can use $\mathrm{d}Q = \rho_6(\vec{r},\vec{p})\,\mathrm{d}V_6$ with ρ being the charge density and $\mathrm{d}Q$ the charge contained in $\mathrm{d}V_6$. If the coupling between the three different planes can be ignored, the complexity of this six dimensional representation can be reduced by defining three two-dimensional subspaces according to the three spatial directions. These are the longitudinal phase space density $f_2(z,p_z)$ and the two transverse phase space densities $f_2(x,p_x)$ and $f_2(y,p_y)$. The reduced phase space densities are, e.g. for the horizontal coordinate, defined by

$$f_2(x,p_x) = \int\int\int\int f_6(\vec{r},\vec{p})\,\mathrm{d}y\,\mathrm{d}p_y\,\mathrm{d}z\,\mathrm{d}p_z. \tag{6.4}$$

In an accelerator, the longitudinal momentum of the particles is orders of magnitude larger than the transverse momenta. Therefore, it is justified to use the paraxial approximation in connection with the divergence angles $x' = p_x/p_z$ and $y' = p_y/p_z$ instead of the transverse momenta. The new density distributions $f_2(x,x')$ and $f_2(y,y')$ are called trace space distributions.
The transverse rms emittance ε_{rms} of a bunch is defined as the rms area it occupies in trace space. For the $\{x,x'\}$-trace space, the expression for $\varepsilon_{x,rms}$ reads

$$\varepsilon_{x,rms} = \sqrt{\langle x^2\rangle\,\langle x'^2\rangle - \langle xx'\rangle^2}\ \ ,[\varepsilon_{x,rms}] = \mathrm{m}\cdot\mathrm{rad}. \tag{6.5}$$

The angular brackets indicate the central second order moments of the enclosed quantities. Assuming $\bar{x} = 0$ and $\bar{x'} = 0$, they are defined as

$$\begin{aligned}
\langle x^2\rangle &= \frac{1}{\int\int f_2(x,x')\,\mathrm{d}x\,\mathrm{d}x'}\cdot\int\int f_2(x,x')\cdot x^2\,\mathrm{d}x\,\mathrm{d}x',\\
\langle x'^2\rangle &= \frac{1}{\int\int f_2(x,x')\,\mathrm{d}x\,\mathrm{d}x'}\cdot\int\int f_2(x,x')\cdot x'^2\,\mathrm{d}x\,\mathrm{d}x',\\
\langle xx'\rangle &= \frac{1}{\int\int f_2(x,x')\,\mathrm{d}x\,\mathrm{d}x'}\cdot\int\int f_2(x,x')\cdot x\,x'\,\mathrm{d}x\,\mathrm{d}x'.
\end{aligned} \tag{6.6}$$

From the definitions of x' and y' follows that the divergence and hence the emittance scales inversely proportional to the longitudinal beam momentum p_z. By normalizing the emittances, it is possible to compare beams of different momenta

$$\varepsilon_{x,rms,norm} = \beta\gamma\cdot\sqrt{\langle x^2\rangle\,\langle x'^2\rangle - \langle xx'\rangle^2}. \tag{6.7}$$

Since all transverse emittance values given in this work follow this definition, the subscripts *rms* and *norm* are omitted from now on.
In addition to the definitions already given, the quantities transverse emittance and transverse phase/trace space distribution can be defined also for thin slices perpendicular to

the z-axis. The resulting transverse slice emittance and slice phase/trace space are important for the concept of emittance compensation described in chapter 6.3. Since the phase space of the whole bunch is a result of the projection of all slice phase spaces onto one plane, the emittance defined in equation 6.5 is also called projected emittance.

Liouville's theorem

Liouville's theorem states that in a conservative field in which the forces can be derived from a potential the six-dimensional volume of the phase space remains constant [Leje]. One consequence of this theorem is that the emittance of a particle ensemble is constant. This invariance of the emittance is a key issue in the description of the particle beam motion in accelerators. Unfortunately, this theorem is not applicable for the description of electron bunches in an injector setup. The reason is that at low beam energies, typical for injectors, the influence of the space charge forces is very strong. Since it is impossible to define a potential and thus an Hamiltonian for space charge forces, Liouville's theorem cannot be applied.
In addition, this theorem is valid for the six-dimensional phase space volume. In the case of coupling between the longitudinal and transverse subspaces, the six-dimensional phase space volume might remain unchanged, but not necessarily its projections to the two-dimensional phase spaces (equation 6.4) whose volume is usually measured.

6.2 Sources of transverse emittance

There are three main contributions to the total transverse emittance. Firstly, there is the emittance arising from disordered movement of the electrons as they escape from the cathode surface (cathode emittance[1]). The second contribution comes from the ponderomotive RF focusing forces while the third reason for emittance growth is the occurrence space charge forces. In the following sections, these contributions will be introduced.

6.2.1 Cathode emittance

As shown in chapter 5.1, the electrons emitted from the photocathode have random directions independent of their position on the cathode. Therefore, the thermal emittance has no x-x' correlation and equation 6.7 reduces to $\varepsilon_{\text{cath}} = \beta\gamma \cdot \sqrt{\langle x^2 \rangle \langle x'^2 \rangle} = \beta\gamma \cdot x_{rms} x'_{rms} = x_{rms} p_{x,rms}/(m_0 c)$. While x_{rms} is defined by the transverse laser spot size, $p_{x,rms}$ needs further consideration. Following the arguments in [Floet], the momentum of an emitted electron is mainly defined by the electron affinity of the material. Firstly, the electron

[1] The term *thermal emittance* is also frequently used even though it originally refers to the cathode emittance of thermionic emitters.

affinity influences the final kinetic energy and secondly, the momentum inside the material must have a sufficiently large component in the direction of the surface normal to overcome the surface potential barrier. Otherwise, the particle is reflected back into the bulk. This sets a limit for the maximum angle the particle momentum can have with respect to the surface normal. This angle can be calculated as

$$\varphi_{max} = \arccos \sqrt{\frac{E_\mathrm{A}}{E_\mathrm{kin}^\mathrm{inside}}}. \tag{6.8}$$

Following the calculation of $p_{x,rms}$ in [Floet], the cathode emittance reads

$$\varepsilon_\mathrm{cath} = x_{rms} \cdot \sqrt{\frac{2E_\mathrm{kin}^\mathrm{outside}}{m_0c^2}} \cdot \frac{1}{\sqrt{3}} \cdot \sqrt{\frac{2 + \cos^3\varphi_{max} - 3\cos\varphi_{max}}{2 \cdot (1 - \cos\varphi_{max})}}. \tag{6.9}$$

Here $E_\mathrm{kin}^\mathrm{outside}$ is the kinetic energy of the electron inside the material reduced by the electron affinity. Typical values for Cs_2Te are $E_\mathrm{kin}^\mathrm{inside} = 0.75\,\mathrm{eV}$ and $E_\mathrm{A} = 0.2\,\mathrm{eV}$ and for the laser beam size at the cathode $x_{rms} = 0.375\,\mathrm{mm}$. For this parameter combination, the cathode emittance amounts to 0.25 mm mrad.
One can further simplify equation 6.9 by allowing the particles to be emitted into the full half-sphere in front of the cathode (φ_{max}=90 degrees)[2]

$$\varepsilon_\mathrm{cath} = x_{rms} \cdot \sqrt{\frac{2E_\mathrm{kin}^\mathrm{outside}}{3m_0c^2}}. \tag{6.10}$$

Using this approximation, the cathode emittance for the above parameter combination is $\varepsilon_\mathrm{cath}$=0.32 mm mrad.

6.2.2 RF induced emittance

The z-component of the time-dependent electric field along the symmetry axis of the gun cavity can be expressed as

$$E_z(z,t) = E_z(z) \cdot \cos(2\pi f \cdot t + \phi_0). \tag{6.11}$$

In this equation, $E_z(z)$ is the time-independent, on-axis field distribution which is determined by the cavity's geometry, f is the RF frequency (about 1.3 GHz at PITZ) and ϕ_0 is an initial phase offset.

[2]The simulation code ASTRA which was used throughout this thesis uses this approximation to simulate the cathode emittance.

Maxwell's equations require that this one-dimensional field definition is generally accompanied by a radial electric field and an azimuthal magnetic field. The radial electric field can be calculated using the constraint $\nabla \cdot \vec{\mathbf{E}} = 0$, which results in

$$E_r(r) = -\frac{r}{2} \cdot \frac{\partial E_z}{\partial z}. \tag{6.12}$$

Correspondingly, Maxwell's equation $\nabla \times \vec{\mathbf{B}} = \frac{1}{c^2} \cdot \frac{\partial \vec{\mathbf{E}}}{\partial t}$ leads to the azimuthal magnetic field

$$cB_\theta(r) = -\frac{r}{2c} \cdot \frac{\partial \vec{\mathbf{E}}}{\partial t}. \tag{6.13}$$

Both equations are defined in cylindrical coordinates and result in a total radial force F_r exerted on particles by the accelerating field

$$F_r(r) = q \cdot \left[E_r(r) - \beta c \cdot B_\theta(r)\right]. \tag{6.14}$$

According to equation 6.11, the force a particle experiences depends on its launch phase. Because of the finite duration of the laser pulses used to extract the particles, the RF focusing force depends on the internal longitudinal bunch coordinate. This variation of the transverse momenta along the bunch causes an increase of the projected emittance.
The contribution from the RF field to the total emittance can be derived by integration of equation 6.14 to get the radial momentum. Afterwards, equations 6.5 and 6.6 can be used to calculate the emittance. Following the derivation in [Kim], the emittance contribution for a cylinder-like electron bunch with length L and initial radius R can be estimated by

$$\varepsilon_{RF} = \frac{\alpha R^2 k^3 L^2}{4\sqrt{6!}}. \tag{6.15}$$

In this equation, $k = 2\pi/\lambda_{RF}$ is the RF wave number and $\alpha = \frac{e \cdot E_0}{2 m_e c^2 k}$ is a dimensionless parameter for the strength of the accelerating field.
For typical values of L=6 mm and r=0.75 mm, the RF induced emittance amounts to ε_{RF}= 2.6·10^{-3} mm mrad.

6.2.3 Space charge-induced emittance

Electrons as charged particles produce an electric space charge-field which defocuses the electron bunch and therefore increases the emittance. According to [Kim], the strength of the transverse space charge force scales with $1/\gamma^2$

$$F_{sc} = \frac{e}{\gamma^2} \cdot E_{sc}. \tag{6.16}$$

Here, E_{sc} is the electric field caused by the charge of the electrons in the bunch rest frame. According to this equation, the influence of the space charge forces are dominant at low

beam kinetic energies, i.e. directly after the emission of electrons from the photocathode. Therefore, the influence of the space charge field on the particles momentum after emission at launch phase ϕ_0 can be estimated by [Kim]

$$\vec{\mathbf{p}} = \frac{1}{E_0 \sin\phi_0} \cdot \frac{\pi}{2} \cdot \vec{\mathbf{E}}_{sc}. \tag{6.17}$$

After introduction of the normalized electric field $\mathscr{E}(x, y, \Delta z) = \frac{4\pi\epsilon_0}{n_0} \cdot \vec{\mathbf{E}}_{sc}(x, y, \Delta z)$ with $n_0 = \int \rho(x, y, 0)\,\mathrm{d}x\,\mathrm{d}y$ being the line charge density at the bunch center, the emittance growth due to space charge can be estimated as [Kim]

$$\varepsilon_{sc} = \frac{\pi}{4} \cdot \frac{1}{\alpha k} \cdot \frac{1}{\sin\phi_0} \cdot \frac{I_p}{I_A} \cdot \mu_x(A). \tag{6.18}$$

The quantity I_p is the bunch peak current, $I_A = 17\,\mathrm{kA}$ is the Alfvén current and $\mu_x(A) = \sqrt{\langle \mathscr{E}_x^2 \rangle \langle x^2 \rangle - \langle \mathscr{E}_x x \rangle^2}$ is dimensionless transverse space charge factor, which depends on the bunch aspect ratio $A = \sigma_x/\sigma_z$ in the laboratory frame.

6.3 Transverse emittance compensation and the invariant envelope

The emittance increase due to RF focusing and space charge forces acts in good approximation as a linear defocussing lens. As in light optics, this can be compensated by a focusing lens. For electron bunches, a solenoid magnet situated downstream the gun cavity can be used as focussing element.
In figure 6.1 the principle of the emittance compensation scheme is displayed. Figure 6.1(a) shows the trace space distribution as it appears directly after emission, its rms area corresponds to the cathode emittance. As the electron bunch propagates through the gun cavity it is subject to the mentioned defocussing forces. In graph 6.1(b) the continuous growth of the beam size as well as the divergence of the particles is shown. Since the radial space charge forces are smaller at the head and the tail of the bunch than at its center, the defocussing is less pronounced (blue arrows: evolution of of the head and the tail parts of the bunch, red arrows: evolution of the longitudinal bunch center). Treating the solenoid as a thin lens, it converts the diverging beam into a converging beam, which is illustrated in figure 6.1(c). Note, that the longitudinal center of the bunch is less convergent than the head and the tail. In the subsequent drift space, the transverse beam size decreases until the focus is reached and the beam diverges again (see also figure 6.2 (red line)). Since the longitudinal bunch center experiences higher radial space charge forces, the increase of the divergence (and beam size) after the focus is faster than for the head and the tail.

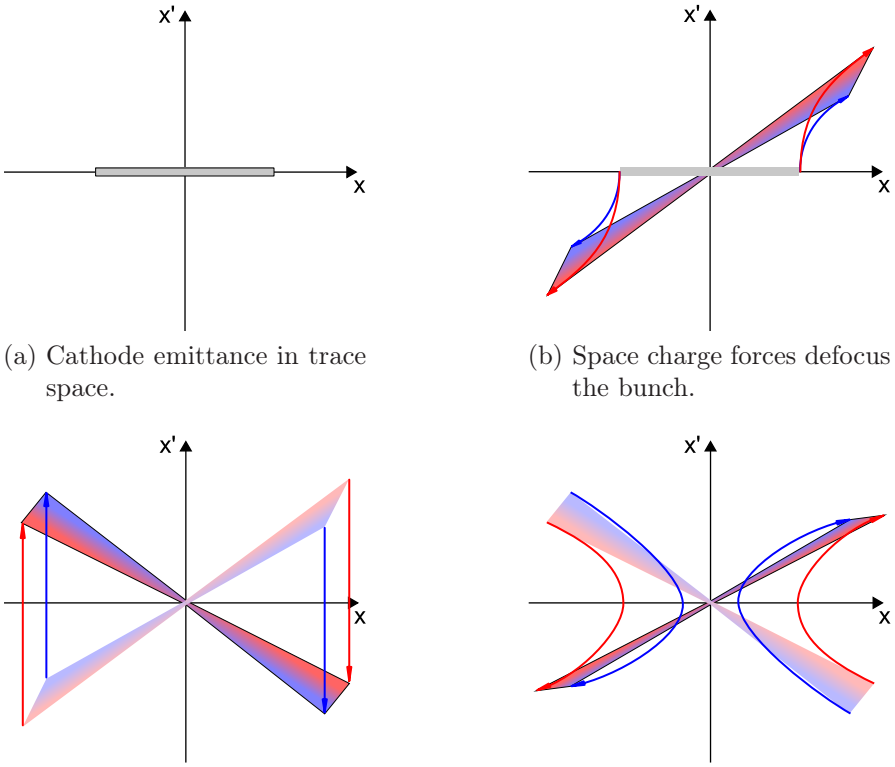

(a) Cathode emittance in trace space.

(b) Space charge forces defocus the bunch.

(c) The solenoid acts as a thin lens.

(d) The trace space distribution evolves into a emittance minimum.

Figure 6.1: *Emittance compensation process. The longitudinal bunch center which experiences higher radial space charge forces is indicated by a red area while the bunch's head and tail are displayed in blue.*

Eventually, this leads to an alignment of the trace space angles of all longitudinal parts of the bunch and thus to an emittance minimum depicted in figure 6.1(d).
To avoid a further emittance increase, the electron bunch must be accelerated very quickly (scaling of the space charge forces with $1/\gamma^2$). Conditions for the optimum acceleration can be found using the invariant envelope approach [Sera].
Before the invariant envelope is discussed, it must be stressed that the emittance compensation scheme only takes into account linear defocussing forces $F_r(r) \propto r$. Nonlinear RF- or space charge forces cannot be compensated and lead to an increase of the total emittance.
Since these nonlinear forces predominantly occur at the transverse edges of the electron beam, they tend to increase the rms trace space area and therefore the emittance even though the charge contained in these regions is low. For this reason, the emittance might be given using a cut of the transverse trace space distribution at a certain trace space

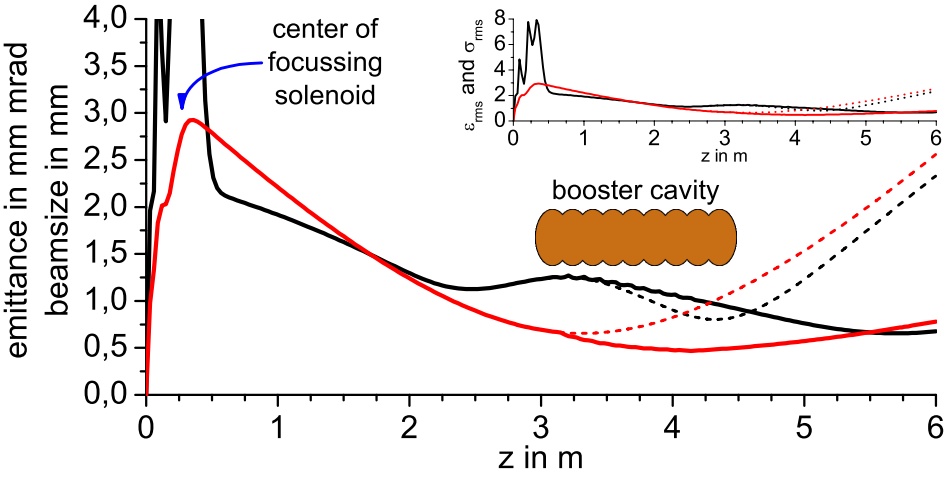

Figure 6.2: *Simulated model case for the transverse emittance (black) and transverse rms beam size (red) evolution along the electron beamline for the cases with (solid line) and without booster (dashed line). The inset shows the same graph which is scaled to see the whole emittance curve.*

intensity level [Stay].

Furthermore, since different longitudinal parts of the electron beam are launched at different RF phases of the gun cavity, a correlation between longitudinal position and momentum exists. For this reason, the projected emittance typically shows two minima in the case of an optimized setup (see figure 6.2), each representing the optimum overlap of head-and-center and center-and-tail slice trace space distributions [Kras01].

The invariant envelope

The evolution of an electron bunch along the beamline can be described in the paraxial approximation by the envelope equation [Carl, Sera]

$$\sigma'' + \sigma' \frac{\gamma'}{\gamma} + \sigma \frac{\Omega^2 \gamma'^2}{\gamma^2} = \frac{\kappa_s}{\sigma \gamma^3} + \frac{\varepsilon_n^2}{\sigma^3 \gamma^2}. \tag{6.19}$$

This model can be applied when the longitudinal momentum spread of the bunch is small so that the longitudinal slices do not mix. Here, $\sigma = \sigma(\zeta)$ is the rms beam size of a longitudinal slice as a function of the internal bunch coordinate $\zeta = z - vt$, γ is the relativistic factor and the primes at each variable indicate the derivative with respect to z. The beam perveance is denoted with $\kappa_s = I_p/2I_A$ (I_p is the peak current and I_A the Alfvén current) and ε_n indicates the normalized rms slice emittance.

Equation 6.19 describes in a general way the evolution of the beam size of longitudinal slices under the influence of a defocussing space charge (first term on the r.h.s.) and the

intrinsic emittance (second term on the r.h.s.). A dominant space charge term results in particle trajectories that do not cross due to the fact that the particles repel one another. The emittance term, on the other hand, describes random particle movement introduced, for example, by the cathode emittance. The defocussing from the space charge can be partially compensated by a linear focussing provided by a solenoid field and/or ponderomotive RF focussing. These effects are subsumed under the dimensionless focussing gradient Ω, which reads for a standing wave accelerating structure [Ferr01]

$$\Omega^2 = \left(\frac{eB_{\mathrm{sol}}}{mc\gamma'}\right)^2 + \frac{1}{8}. \tag{6.20}$$

For equation 6.19, an exact analytical solution can be found for which the angle of the trace space distribution of each longitudinal slice is the same and independent of the slice perveance $\kappa_{\mathrm{slice}} = I_{\mathrm{slice}}/2I_A$. This solution is called the invariant envelope [Sera, Ferr01]

$$\sigma_{IE} = \frac{1}{\gamma'} \cdot \sqrt{\frac{2I_{\mathrm{slice}}}{I_A(1+4\Omega^2)\gamma}}. \tag{6.21}$$

With this solution the phase space angle δ becomes $\delta = (\gamma\sigma'_{IE})/\sigma_{IE} = -\gamma'/2$ [Ferr02].
For a split photoinjector setup (like PITZ), the envelope evolution in the drift between the gun and the booster cavity needs to be carefully matched to the invariant envelope solution at the booster cavity. This is why the position of the beam waist must coincide with the booster entrance and the following condition must be satisfied [Sera]

$$\gamma'_{\mathrm{booster}} = \frac{2}{\sigma_{\mathrm{waist}}} \cdot \sqrt{\frac{I_p}{3I_A\gamma}}. \tag{6.22}$$

This equation results from plugging $\Omega^2 = \frac{1}{8}$ (only RF focussing) into equation 6.21 and solving for the normalized accelerating gradient γ'.
The emittance evolution of the electron beam for an emittance-optimized PITZ setup including the booster cavity is shown in figure 6.2 (solid lines). In comparison to the case without booster (dashed lines), the position of the emittance minimum has moved further downstream and is preserved for a longer distance. In addition, the emittance (black line) is lower due to RF focussing in the booster which causes a reduction of the transverse beam size (red line). Since the space charge forces are still dominant, an emittance growth is still observed after the emittance minimum.
To avoid this behavior, the electron beam must be accelerated until the space charge force is small compared to the emittance contribution in the envelope equation. The ratio of both contributions is called laminarity parameter Ξ

$$\Xi = \frac{I_p\sigma^2}{2\gamma I_A\varepsilon_n^2}. \tag{6.23}$$

For $\Xi < 1$, the electron beam becomes emittance-dominated. The transition occurs at $\Xi = 1$ [Ferr01]

$$\gamma = \sqrt{\frac{2}{3}} \cdot \frac{I}{I_A \varepsilon_{\text{cath}} \gamma'}. \tag{6.24}$$

For typical XFEL injector parameters ($I = 45\,A$, $\varepsilon_{\text{cath}}$=0.3 mm mrad and E_{acc}=12 MV/m) the transition takes place at a beam energy of about 157 MeV. For this reason, an injector consists of a series of accelerating cavities transferring sufficient energy to the electron beam to conserve the emittance.

6.4 The longitudinal phase space

The longitudinal phase space distribution of the electron beam is mainly characterized by the dynamics in the electron gun cavity. As it was pointed out earlier, the standard laser pulse duration at PITZ is 20 ps (FWHM) which corresponds to about 9.4 degrees

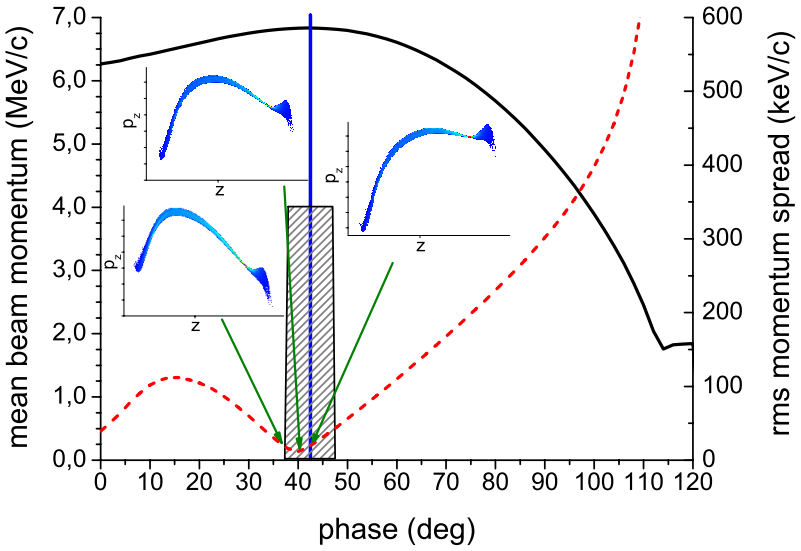

Figure 6.3: *Simulation of the launch phase dependence of the mean momentum gain (black solid line) and the rms momentum spread (red dashed line) for the case of a 20 ps (FWHM) flat top laser pulse having 2 ps rise and fall times. The reference phase ϕ_{ref} is indicated by a blue line and the laser pulse shape is represented by a striped trapezoid. The simulated longitudinal phase space distributions at 0.25 m downstream the cathode are shown for the reference phase (right), the phase of minimum momentum spread (top) and a phase at which the longitudinal phase space distribution starts to turn over (bottom).*

of RF phase. For this reason, the head and the tail of the electron bunch experience different electric field strengths during emission. In addition, part of the accelerating RF field is diminished by the electric field generated by the mirror charge of the previously emitted electrons. In order to reduce the deteriorating influence of the space charge on the transverse emittance, the electrons are usually emitted at the phase of maximum mean momentum gain (in the following referred to as reference phase ϕ_{ref}). This phase is indicated by a blue line in figure 6.3. At an emission phase close to the reference phase, the head of the bunch always experiences a lower accelerating field at the photocathode than the tail. But at any time after emission, still being in the first (half) cell, the integrated field the head of the bunch experienced is larger than that of the tail and therefore its momentum is higher. This corresponds to a positive z-p_z-correlation.
Depending on the launch phase, the head and the tail of the electron beam enter the full cell at certain phases which determine the difference in energy gain between head and tail. At the reference phase, the z-p_z-correlation remains positive (red dashed line figure 6.3). For lower launch phases $\phi < \phi_{ref}$, the correlation first vanishes, which is identical to the phase of minimum momentum spread. For even lower phases, the longitudinal phase space distribution turns over and the z-p_z-correlation becomes negative. The z-dependence of the momentum is depicted in figure 6.4 for the case that the electron beam was launched at $\phi_{ref} \cong 42$ degrees.
Since the response time of the Cs_2Te photocathode is small compared to the laser pulse duration, any modulation that is present on the flat top part of the laser pulse is translated into density modulations of the longitudinal phase space distribution. These modulations

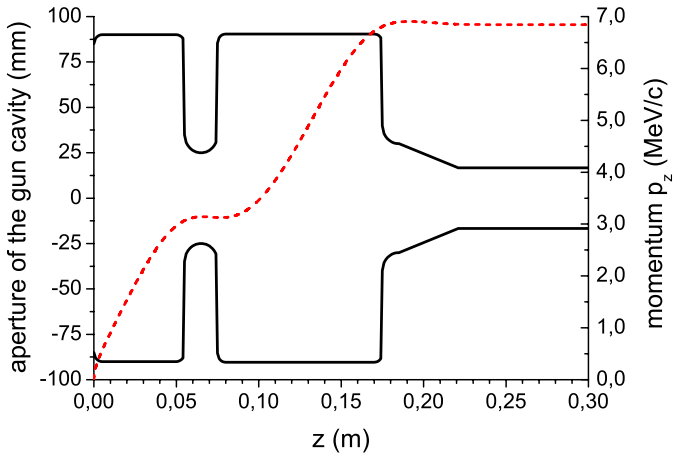

Figure 6.4: *Simulation of the electron beam mean momentum during acceleration in the electron gun cavity. The shape of the cavity is shown in black solid lines while the mean momentum is drawn as red dashed line.*

are also visible in the projections of the longitudinal phase space distribution onto the temporal and momentum axes provided that the z-p_z-correlation allows to resolve them. These effects are presented in the section 7.6.

Chapter 7

Influence of the laser pulse parameters on the electron beam properties

This chapter is dedicated to the presentation of the fundamental relations between laser pulse parameters and electron beam properties. Firstly, some general considerations will be presented including an explanation of why the default temporal laser profile was chosen to be a 20 ps (FWHM) flat-top with rise and fall times of 2 ps. Afterwards, the simulated optimum set of parameters (solenoid field strength, laser spot size on the photocathode, gun phase and booster phase) to obtain lowest transverse emittance will be discussed. In the subsequent sub-chapters, detailed simulations are presented which show how deviations from the optimum laser pulse shape act on the electron bunch properties. These simulations are accompanied by electron beam measurements.
Unless stated otherwise, all simulations were done for the PITZ setup described in chapter 2.1 using standard operating conditions summarized in table 7.1. The transverse emittance was evaluated at the position of the first Emittance Measurement System (EMSY1) which is located 5.74 m downstream of the photocathode. At this position, the measurements of the transverse emittance are performed.

Machine parameter	Value
max. electric field gun	60 MV/m
max. electric field booster	14 MV/m
nominal bunch charge	1 nC
$E_{\mathrm{kin}}^{\mathrm{initial}}$ for calculation of $\varepsilon_{\mathrm{cath}}$	0.55 eV

Table 7.1: *Summary of the standard operation conditions used in simulations and experiment unless stated otherwise.*

7.1 General considerations

The optimum laser pulse profile, temporal as well as transverse, arises from considerations of the electron bunch shape which allows for the best performance of the emittance compensation process. These considerations are presented in the following by treating the main laser pulse properties separately - the laser pulse energy, the transverse laser pulse shape and the temporal laser profile. It is assumed that the cathode response time is short enough, so that the temporal characteristics of the emitted charge corresponds to the temporal laser pulse profile.

The laser pulse energy

The laser pulse energy is the main determinant for the amount of extracted charge. In addition, the charge can be further enhanced by the electric field amplitude during emission according to equation 5.3 or diminished due to mirror charge fields (see chapter 5.3). While the first effect results in an increased bunch charge, the second one can significantly deteriorate the longitudinal phase space distribution and lead to particle loss at the cathode in case the strength of the mirror charge field compensates the external accelerating field. Despite the fact, that less than the desired bunch charge is extracted, this effect disturbs the emittance compensation process and hence leads to an increased transverse emittance. To avoid these detrimental consequences, the laser spot size on the photocathode must be increased to reduce the charge density at emission.

The transverse laser pulse shape

To further investigate the influence of the transverse laser pulse shape on the electron bunch properties, it is useful to consider the transverse size and shape of the laser pulse separately. The transverse laser spot size defines the amount of cathode emittance according to equation 6.9 and hence the lower limit of the achievable total transverse emittance. From this point of view, a smaller laser spot size is favorable. On the other hand, a smaller laser spot size leads to an increase of the transverse space charge forces and therefore the transverse emittance. For these reasons, an optimum beam size must be found which is a compromise between cathode emittance and space charge forces. As shown in the following subsection on the temporal laser shape, the transverse shape of the electron beam must be a circular flat-top. The dependencies discussed so far are illustrated in figure 7.1. Here, the dependence of the transverse emittance on the initial laser spot size is shown for a temporal flat-top laser profile having a duration of 20 ps and rise and fall times of 2 ps. In addition, the contribution from the cathode emittance and the total emitted charge are displayed. The optimum laser spot size is x_{rms}=0.425 mm, which corresponds

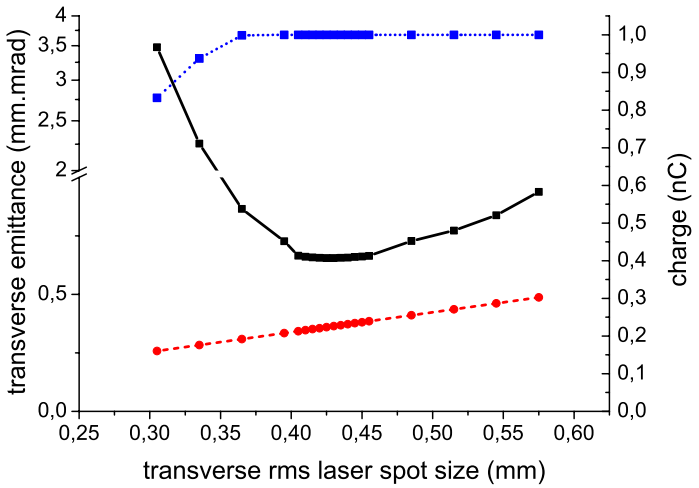

Figure 7.1: *Transverse emittance versus the transverse laser spot size. Displayed are the simulated total transverse emittance at 5.74 downstream of the photocathode (black solid line), the cathode emittance (red dashed line) and the emitted charge (blue dotted line)*

to a diameter of 1.7 mm[1]. For laser spot sizes smaller than x_{rms}=0.37 mm, the emission becomes space charge dominated and a fraction of the extracted charge cannot leave the cathode. For laser spot sizes larger than x_{rms}=0.45 mm the cathode emittance starts to dominate the total transverse emittance.

The temporal laser pulse shape

In chapter 6.3, it was shown that the emittance compensation process can counteract linear transverse defocussing forces. For this reason, it must be ensured that the transverse space charge forces are linear: $F_r(r) \propto r$. This is true for a cylindrical electron beam of radius R and an infinite longitudinal extension having a homogeneous charge density ρ. In this case, the defocussing force experienced by an electron at distance $r < R$ from the cylinder center is $F_r(r) = \frac{e\rho}{2\varepsilon_0} \cdot r$ which can be simply obtained by applying Gauss' law. Since the actual electron bunch is not infinitely long, the transverse space charge forces at the head and the tail are smaller than in the center. The required temporal laser pulse shape according to these considerations is a flat-top with short rise and fall times.
The optimal duration of the laser pulse is again a compromise between several considerations. To reduce the strength of the transverse space charge fields, a longer laser pulse duration is preferential. On the other hand, FEL operation requires large electron bunch

[1]For a transverse flat-top profile, the relation between rms size x_{rms} or y_{rms} and diameter d is $d = 4 \cdot x/y_{rms}$.

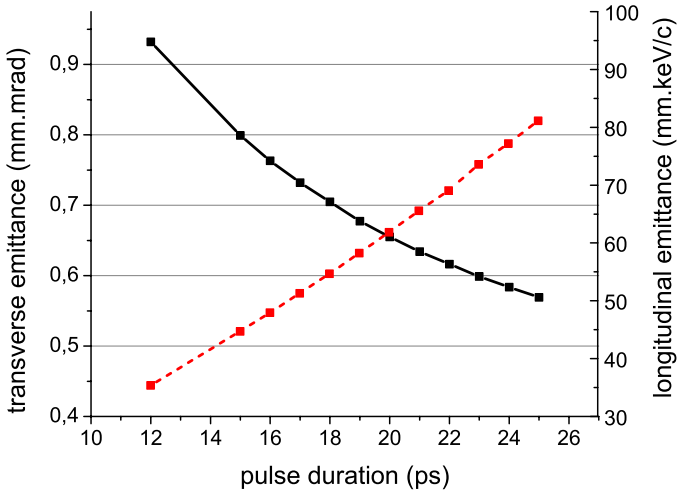

Figure 7.2: *Simulated transverse (black solid line) and longitudinal emittance (red dashed line) versus laser pulse duration. The temporal laser shape in this case was a flat-top with rise and fall times of 2 ps.*

currents, which gives rise to the need of electron bunch compression [XFEL]. This works best when the longitudinal phase space distribution has a linear correlation. Laser pulses with a long duration generate electron bunches which acquire the nonlinearity of the sinusoidal accelerating field during emission, which can be removed only partially by a third harmonic cavity [XFEL]. For this reason, short laser pulses are more beneficial.

To illustrate the described situation, the dependence of the transverse and longitudinal

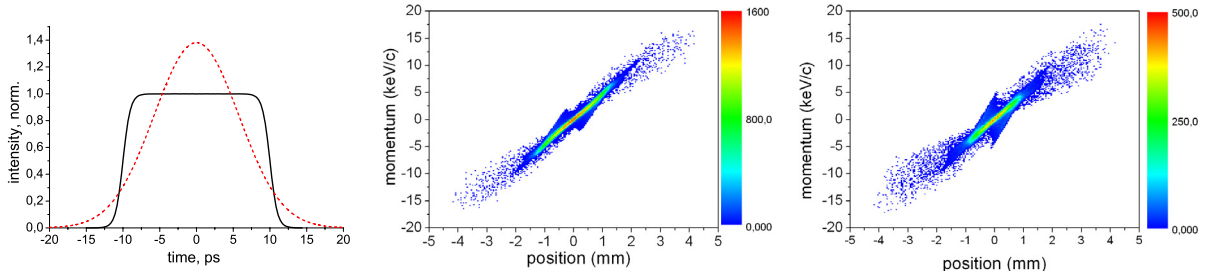

Figure 7.3: *Comparison between a flat-top (black solid line) and a Gaussian (red dashed line) temporal laser profile, both having the same rms duration. On the left side the temporal profiles are shown normalized to the same area. The center and the right graph depict the simulated transverse phase spaces for the flat-top and the Gaussian profile, respectively. The corresponding transverse emittance values are* $\varepsilon_x^{FT} = 0.66\,mm\,mrad$ *and* $\varepsilon_x^{Gauss} = 1.05\,mm\,mrad$

emittance values on the laser pulse duration are depicted in figure 7.2. The given numbers were obtained by an numerical optimization of the machine parameters for lowest transverse emittance. No constraint was given to the longitudinal emittance. As a compromise, a pulse duration of 20 ps FWHM was chosen [XFEL].
In order to demonstrate the benefits of an homogeneous charge distribution, figure 7.3 shows two simulated transverse phase space distributions. The first was obtained for a flat-top temporal profile of 20 ps (FWHM) and 2 ps rise and fall times, while for the second one a temporally Gaussian shape was used. Both temporal profiles have the same rms duration which results in a FWHM duration of 13.6 ps for the Gaussian shape. The distributions were obtained from an optimization of the machine parameters. The goal was to minimize the transverse emittance at the location of EMSY1 at 5.74 m downstream of the photocathode.
The temporal laser pulse shape described so far, also known as *beer can* shape, displays the optimum in case that changes of the temporal and the transverse characteristics of the laser pulses can be performed solely independently. Without this constraint, which was not yet possible to overcome with conventional laser systems, an electron bunch having a homogeneous charge density bounded by a three dimensional ellipsoid shows better performance. As shown in [Limb], this shape exhibits linear space charge forces in all direction making it the optimal shape for the emittance compensation process. Furthermore, this shape remains ellipsoidal under the influence of linear external forces and the internal linear space charge forces. It has been demonstrated by simulations that the initial cathode emittance can be fully recovered. In addition, the linearity of the longitudinal phase space results in the fact that a bunch compression, as it is needed in FELs, is easier to achieve [Limb].
So far, no laser system is capable of producing ellipsoidal laser pulses, but another approach has emerged. As described in [Luit], one can use instead a very short laser pulse (usually of the order of tens of femtoseconds) to extract the electrons from the cathode surface. Due to the strong space charge fields this so-called *pancake*-shaped electron bunch self-evolves into an ellipsoid. This principle was proven experimentally [Musu, Mood] but has one major limitation. Since the laser pulses are very short, the mirror charge field after extraction is very large. To stay below the threshold of space charge limited extraction, this scheme can only be applied to low-charge electron bunches.

7.2 The optimized laser pulse properties

The aforementioned considerations led to a temporal laser pulse shape of a flat-top with 20 ps (FWHM) duration and rise and fall times as short as possible. The laser system employed at PITZ is capable of producing such laser pulses with rise and fall times of about 2 ps. For this temporal profile and a transverse circular flat-top shape, an optimization of the machine parameters was performed to elaborate a baseline for further investigations on

Parameters for the simulation	
no. of macro particles	350 000
no. of radial cells	20
no. of longitudinal cells	50
no. of particles emitted in one time step	50

Table 7.2: *Fixed parameters used for the optimization of the machine parameters. For the definition of simulation parameters see [ASTRA].*

gun launch phase	-1.5 deg
booster phase	+3.0 deg
solenoid peak field	230.6 mT
rms laser spot size	0.425 mm

Table 7.3: *Optimized machine parameters for minimum transverse emittance at 5.74 m downstream of the photocathode. The temporal laser shape is a flat-top with a duration of 20 ps and rise and fall times of 2 ps. The bunch charge is 1 nC.*

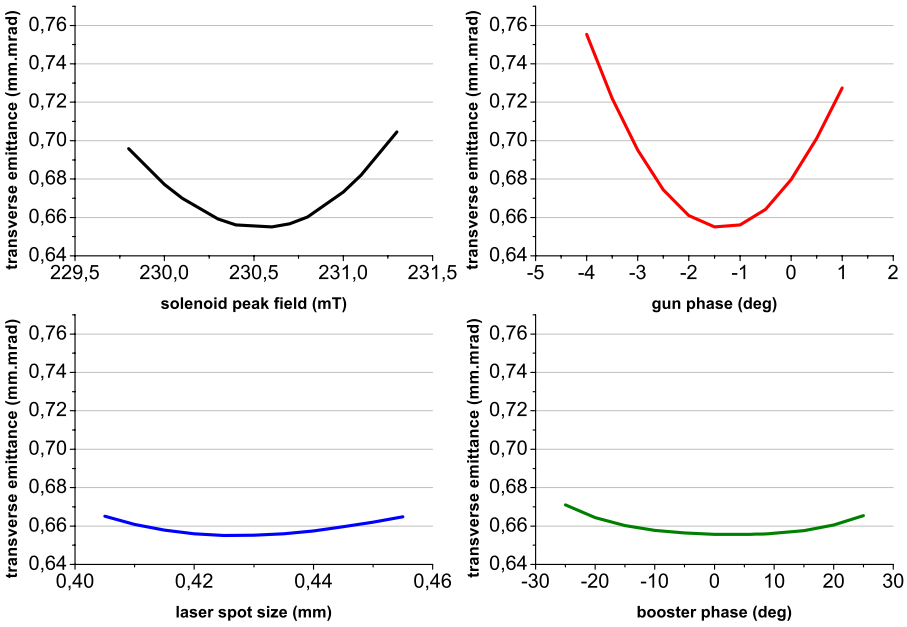

Figure 7.4: *Dependence of the transverse emittance on the optimized parameters.*

deviations from that profile. The parameters used in the simulation code are summarized in table 7.2.
The optimization resulted in an projected transverse emittance of ε_n=0.66 mm mrad for the machine parameters which are summarized in table 7.3. Note that the gun and booster phases are given relative to the phase of maximum mean momentum gain (reference phase ϕ_{ref}).
In figure 7.4, the dependence of the transverse emittance on the individual parameters is displayed. In each case, all other parameters were kept at the optimum value. For better comparability, all ordinates have the same scaling. The dependence on the booster phase is very small. For this reason and to reduce the optimization efforts, the booster phase is kept at maximum mean momentum gain for all simulations that will be presented hereafter.

7.3 Influence of the laser pulse duration

As a first step, the influence of the laser pulse duration on the transverse emittance has been investigated. The results of the simulations were shown in figure 7.2. The different temporal laser profiles, that were used in the simulations, are displayed in figure 7.5. The graphs were normalized to have the same area (or total charge).

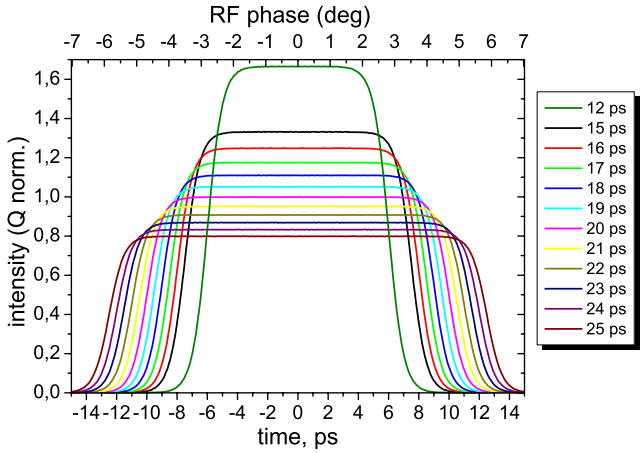

Figure 7.5: *Temporal laser profiles used for the simulations. The upper axis indicates the amount of RF-phase spanned by the laser pulse. The legend shows the corresponding pulse durations (FWHM).*

The optimized machine parameters for all profiles are displayed in figure 7.6. The solenoid peak field is almost unchanged ($B_{\mathrm{sol}} = 230.6 \pm 0.1\,\mathrm{mT}$) since it is mainly determined by the bunch momentum and the transverse space charge force. The increase of the space

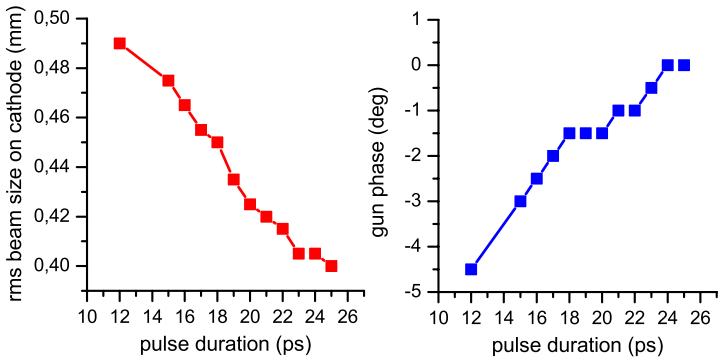

Figure 7.6: *Dependence of optimized laser spot size and gun RF-phase on the pulse duration.*

charge forces towards shorter pulse durations is compensated by larger laser spot sizes. The second graph shows the optimum launch phase, which changes towards lower values for shorter laser pulses. The reason for this behavior is the following. Shorter pulse durations lead to higher longitudinal space charge forces which result in an acceleration of the head and a deceleration of the tail of the bunch. This increases the z-p_z-correlation which is disadvantageous for the emittance compensation. Therefore, a smaller phase must be used to compensate this effect.

Experiments

In order to investigate the dependence of the transverse emittance on the laser pulse duration, the following setup was used. The gun and the booster cavities were operated at a maximum gradient of 60 MV/m and 14 MV/m, respectively. The emission phases were chosen to be 0 degrees and +6 degrees while the booster was always at on-crest phase. The BSA diameter was 1.8 mm which corresponds to measured laser spot sizes of $x_{rms} \cong 0.432$ mm and $y_{rms} \cong 0.445$ mm (see figure 7.8). For each setting, the current of the solenoid magnet was scanned to find the minimum transverse emittance.
Since the parameters used in the experiment differ from the optimum conditions found in the previous section, additional simulations were performed to be able to compare simulation and experiment. Figure 7.7 shows that the transverse emittance decreases towards longer pulse durations for both emission phases. The difference to the emittance values shown in figure 7.2 result from the not optimal laser spot size and emission phase in the gun cavity.
Using the pulse shaper described in chapter 3.2.2, the laser pulse duration was varied. The rise and fall times were kept as short as possible. The resulting temporal laser shapes together with the transverse laser shape that was used for the experiments are shown in figure 7.8 and the temporal laser pulse properties are compiled in table 7.4.

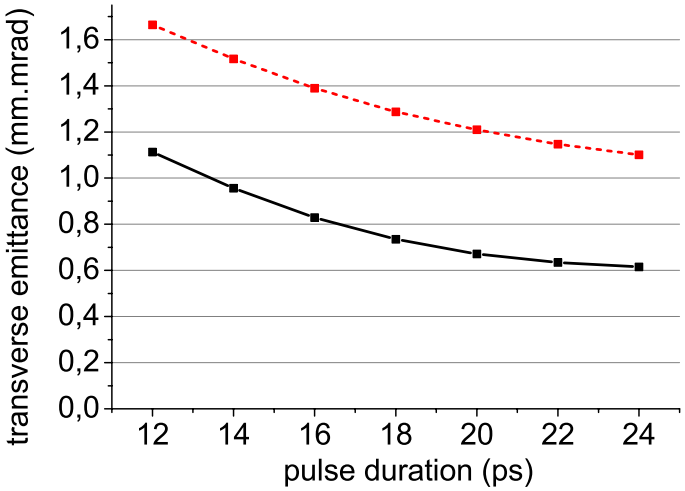

Figure 7.7: *Simulated dependence of the transverse emittance on the laser pulse duration for the specific experimental conditions and a gun launch phase of 0 degrees (black solid line) and +6 degrees off-crest (red dashed line).*

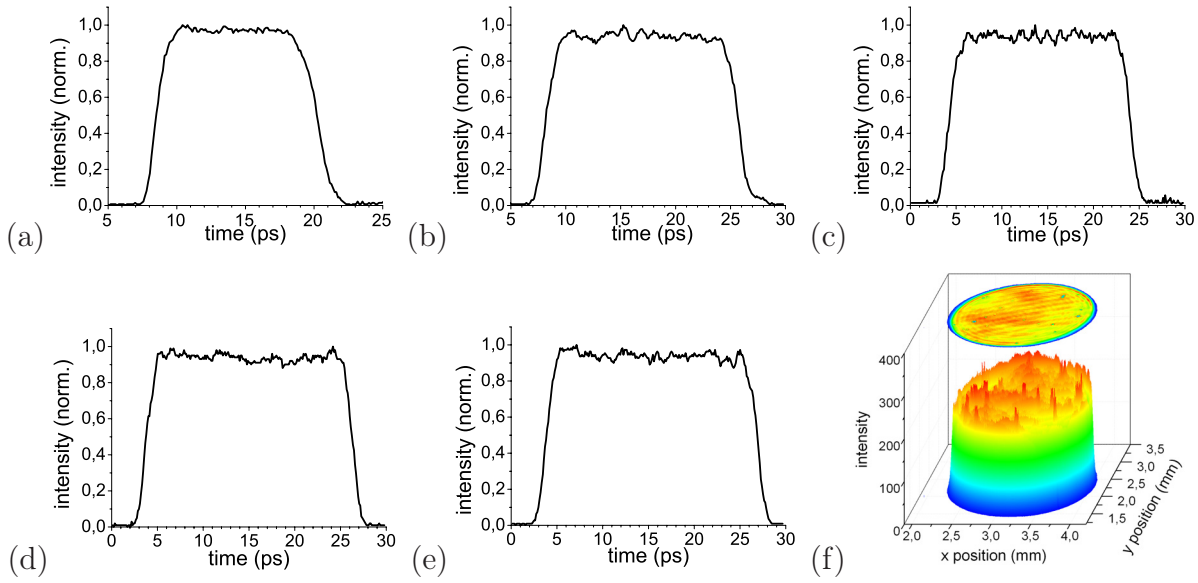

Figure 7.8: *Temporal laser shapes (a)-(e) and the transverse laser shape (f) used in the experiments. The BSA had a diameter of 1.8 mm. While the peaks in the transverse profile were caused by diffraction originating from dust particles on the CCD chip, the faint horizontal stripes were caused by interference of the laser pulse in the cover plate of the CCD.*

laser pulse profile	duration (FWHM)	rise time	fall time	modulation on flat-top
(a)	11.7 ps	1.8 ps	2.8 ps	5.8 %
(b)	17.5 ps	2.3 ps	2.4 ps	8.4 %
(c)	19.8 ps	2.4 ps	2.2 ps	8.6 %
(d)	22.5 ps	2.2 ps	2.0 ps	6.4 %
(e)	23.1 ps	2.2 ps	2.3 ps	9.2 %

Table 7.4: *Laser pulse parameters as they are obtained by applying a non-symmetric trapezoidal fit to the temporal laser shapes displayed in figure 7.8. The modulation is calculated as* $\frac{max-min}{2\,mean} \cdot 100\%$ *on the flat-top part.*

In figure 7.9, the results of the experimental investigations are shown. Displayed are the transverse emittance values in x- and y-direction measured at the first Emittance Measurement System (EMSY1) obtained after optimization of the solenoid current. In addition to the transverse emittance in both planes, the geometric average $\varepsilon_{xy} = \sqrt{\varepsilon_x \cdot \varepsilon_y}$ is shown. The transverse emittances in x-direction are in general lower than those in y-direction. We believe that this is caused by a field asymmetry which is imposed by the RF-coupler of the booster cavity.
A discussion of the error sources and the resulting error bars can be found in Appendix D. The transverse emittance is in almost all cases larger then expected from the simulations. In addition, they are lower for the off-crest gun launch phase. This behavior contradicts the predictions from simulations and found only a partial explanation in the instability

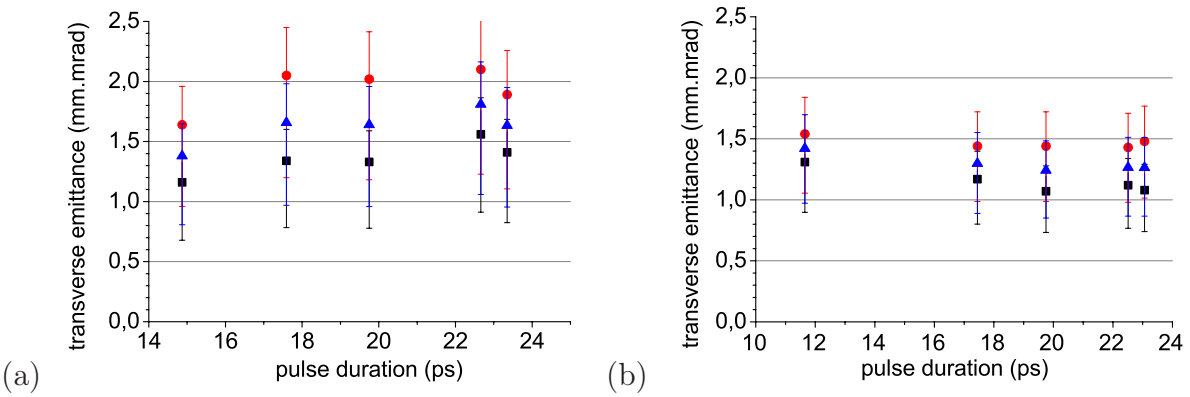

Figure 7.9: *Measurement of the dependence of the transverse emittance on the laser pulse duration. The left graph shows the results for the gun cavity operated at reference phase, while in the right graph the phase was +6 deg off-crest. For each duration value the measured transverse emittances* ε_x *(black squares),* ε_y *(red dots) and the geometrical average* ε_{xy} *(blue triangles) are shown.*

of the RF gun phase (see Appendix D).
While the emittance in the case of the on-crest emission slightly increases towards longer pulse durations, this tendency appears to be inverted for the off-crest acceleration. In simulations, the reduction in emittance amounts to about 35 % between 12 ps and 24 ps, while in the experiment this decrease is only about 12 %. In addition the emittance value at about 12 ps pulse duration is smaller than expected from the simulations.
Due to problems with RF phase stability, a final conclusion on the influence of the laser pulse duration on the transverse emittance cannot be drawn.

7.4 Influence of laser pulse rise and fall times

To retrieve the dependence of the transverse emittance on the rise and fall times, detailed simulations have been performed to optimize the machine parameter for the different values. The laser pulse duration of 20 ps (FWHM) was kept constant while the rise and fall times were varied between 0.5 ps and 8 ps. For larger rise and fall times, the laser pulse does not have a flat-top anymore. The temporal laser shapes used for the simulations are shown in the left part of figure 7.10. The right graph shows the optimized transverse emittance together with the corresponding longitudinal emittance.

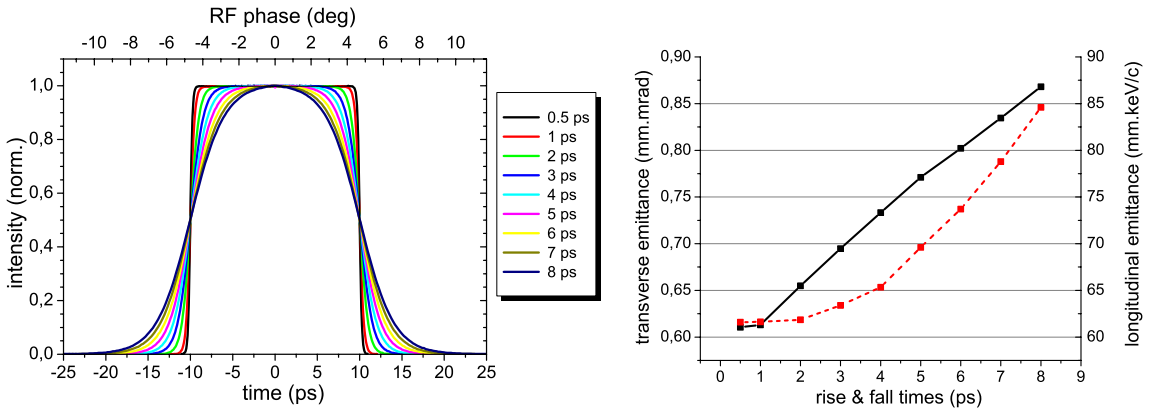

Figure 7.10: *Left: Temporal laser shapes used for the optimization. Right: Optimized transverse emittance (black, solid line) together with the longitudinal emittance (red, dashed line).*

Almost no difference in the transverse emittance can be seen for rise and fall times of 0.5 ps and 1 ps. A further increase of the rise and fall times results in an almost linear rise of the minimum achievable transverse emittance. This has basically two reasons. Firstly, the nonlinearity of the transverse space charge forces along the longitudinal axis increases and secondly, the total span of the laser pulse in terms of RF-phase grows and thus the longitudinal phase space distribution becomes more nonlinear (see longitudinal emittance

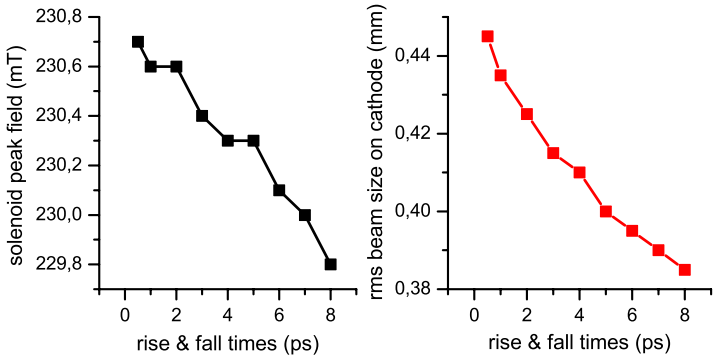

Figure 7.11: *Dependence of optimized parameters on the rise and fall times.*

in figure 7.10). These two reasons reduce the efficiency of the emittance compensation. The dependence of the optimized parameters on the rise and fall times are depicted in figure 7.11. For longer rise and fall times the preferred solenoid current decreases because the reduced average bunch current requires less focussing strength. Further, the increased bunch length allows for smaller transverse laser spot sizes. The variations in the gun phase of $\phi = -1.0 \pm 0.5$ degrees is not significant.

Experiments

During the experiments, the Beam Shaping Aperture was chosen to have a diameter of 1.5 mm, which corresponds to a laser spot size of $x_{rms} = y_{rms} = 0.375$ mm for a perfect circular flat-top. The measured laser spot sizes were $x_{rms} \cong 0.365$ mm and $y_{rms} \cong 0.368$ mm (see figure 7.13). The gun launch phase was $+6$ degrees off-crest and the magnetic field strength of the solenoid was optimized experimentally. The results of the simulations reflecting the specific experimental conditions are depicted in figure 7.12.
The linear increase of the transverse emittance for longer rise and fall times which was found earlier is only true for the case of on-crest acceleration, whereas for the case of $+6$ degrees gun launch phase, the transverse emittance is slightly smaller for 2 ps rise and fall times, but remains constant for all other cases at about 1.33 mm mrad. Besides this finding, the transverse emittance for $+6$ degrees gun phase is in general larger than for the on-crest case.

The experimentally used temporal laser shapes are shown in figure 7.13. For some values of the rise and fall times, the transverse emittance was measured several times. In these cases, only one measured temporal profiles is shown even though, the temporal shapes were recorded each time. The laser pulse parameters for all measurements are compiled in table 7.5. In figure 7.14, the experimentally measured transverse emittance values are displayed. The main results are, that the transverse emittances are almost constant within the error bars but about 0.2 mm mrad lower than expected from the simulations. The

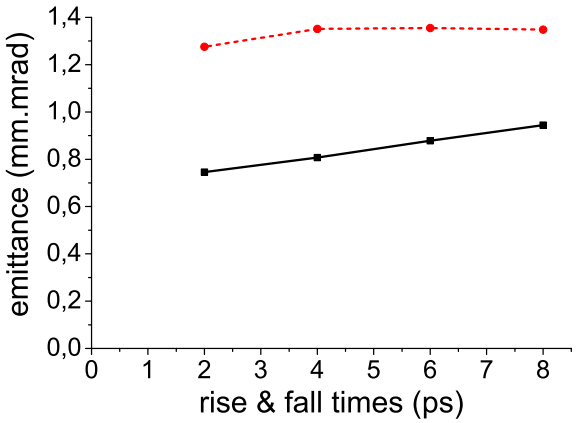

Figure 7.12: *Simulated transverse emittance for the experimental conditions. Even though the measurements were only performed for a gun launch phase of +6 degrees (red, dashed line), the simulation results for the on-crest (black, solid line) case are also displayed.*

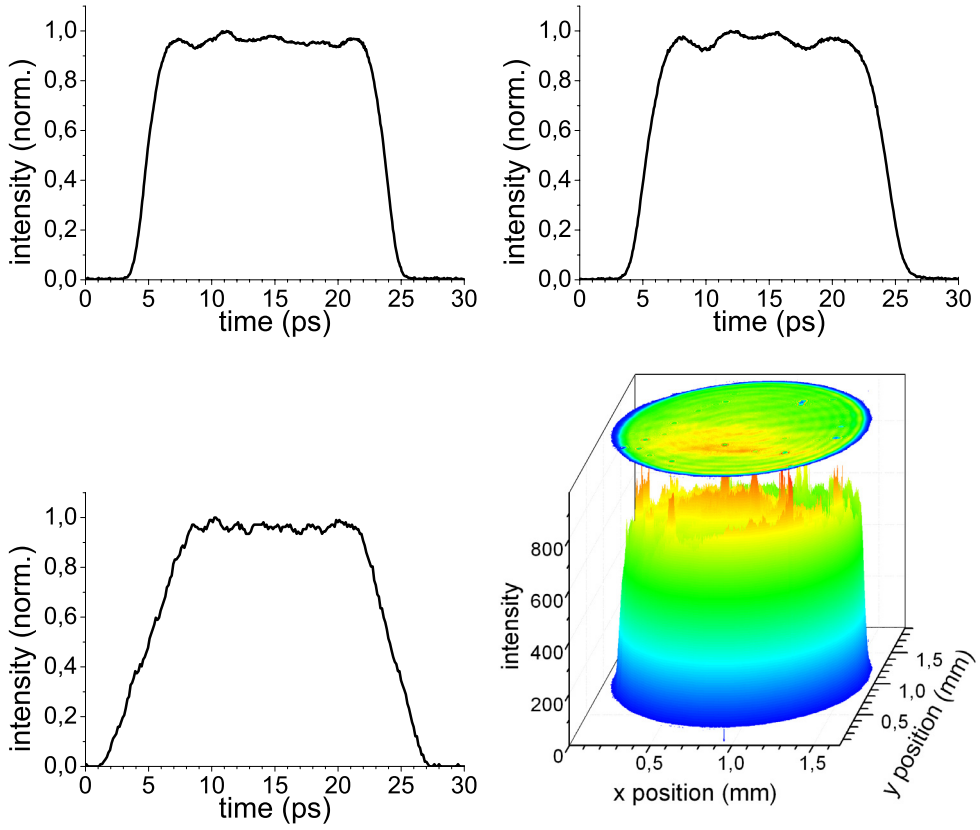

Figure 7.13: *Temporal and transverse laser shapes used for the measurements.*

laser pulse profile	duration (FWHM)	rise time	fall time	modulation on flat-top
1.	18.8 ps	2.5 ps	2.6 ps	5.6 %
2.	19.3 ps	2.4 ps	2.6 ps	5.7 %
3.	19.6 ps	2.5 ps	2.5 ps	5.3 %
4.	18.9 ps	3.0 ps	3.5 ps	6.3 %
5.	19.5 ps	3.0 ps	3.4 ps	4.9 %
6.	19.8 ps	7.1 ps	5.5 ps	3.1 %
7.	19.4 ps	6.8 ps	5.1 ps	3.4 %

Table 7.5: *Parameters of the temporal laser pulse shapes used in the experiments.*

first finding corresponds to the expectations from the simulations, while the second result cannot be explained straightforwardly. One possible explanation is that the transverse shape of the laser pulses is not perfectly flat-top. Instead, it has a slight maximum which can lead to a lowering of the transverse emittance. This effect will be discussed in detail in section 7.8.

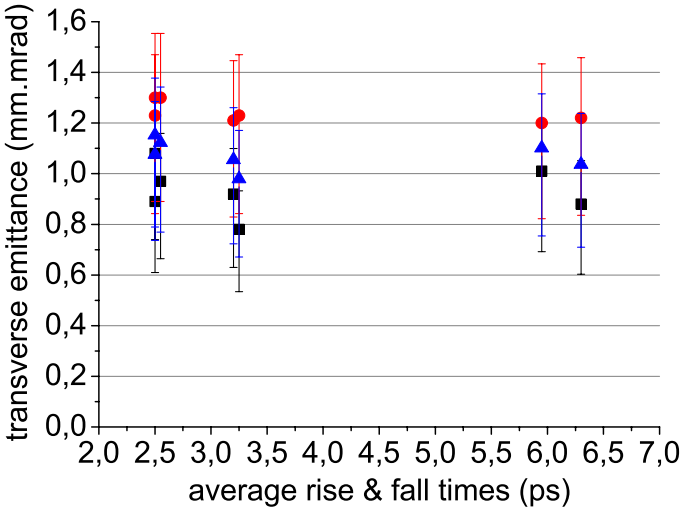

Figure 7.14: *Results of the emittance measurements at +6 degrees gun launch phase. Depicted are ε_x (black squares), ε_y (red dots) and their geometric average ε_{xy} (blue triangles).*

7.5 Influence of modulations on the flat-top

The next subject that has been investigated is the influence of modulations on the flat-top of the temporal laser pulse profile on the transverse emittance. Before the measurements were done, detailed simulations were performed for sinusoidal modulations on the flat-top part having two, three, four and five peaks of various heights as shown in figure 7.15. Different to the other sections, the modulation depth is defined here as the percentage by which the intensity drops in the valleys of the profiles compared to the peak value. For all temporal profiles, an optimization was performed and the resulting transverse emittance values are depicted in figure 7.16. The dependence of the transverse emittance on modulations on the flat-top is very weak in a large range of modulation depths and is more pronounced for a larger number peaks.

Two main reasons are responsible for the weak dependence. Firstly, during the emittance compensation process, the alignment of the different longitudinal slices in the transverse phase space is almost independent from the slice perveance. And secondly, at a charge level of 1 nC, the longitudinal space charge forces reduce small modulations.

For two maxima, the transverse emittance decreases for a modulation depth in the range of 0 % - 50 % and has a minimum at about 33 %. As described earlier, the reason is that the transverse space charge force is not constant along the longitudinal axis. It has a maximum at the center and decreases towards the head and the tail of the electron

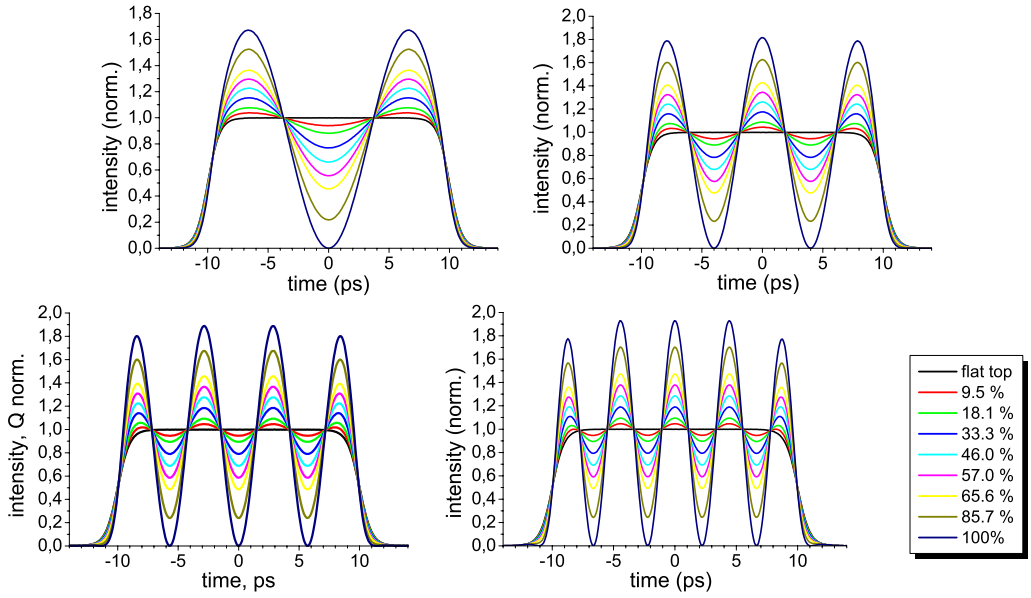

Figure 7.15: *Temporal laser profiles used for the simulations. The profiles were rescaled to have the same area. In the legend, the modulation depth according to the definition in the text is given.*

bunch. By reducing the charge at the center of the bunch, this variation of the transverse space charge forces can be balanced which leads to a better emittance compensation.
In figure 7.17, the resulting optimized parameters are depicted. The optimum laser spot size decreases for larger modulation depths. The reason is that the longitudinal parts of the electron bunch having a maximum of charge density repel each other. This causes an increase of the bunch length and therefore a decrease of the average bunch current. Thus, a smaller transverse electron beam size is preferred. This effect is supported by an additional delay of the emission induced by the intensified mirror charge effect at the photocathode caused by higher charge densities in the peaks.

The optimum solenoid field strength remains almost constant up to a modulation depth

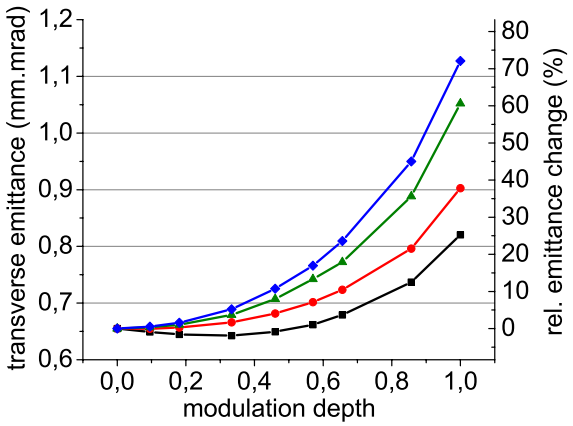

Figure 7.16: *Optimized transverse emittances for the temporal laser profiles shown in figure 7.15. The color code is: 2 peaks - black squares, 3 peaks - red dots, 4 peaks - green triangles and 5 peaks - blue diamonds.*

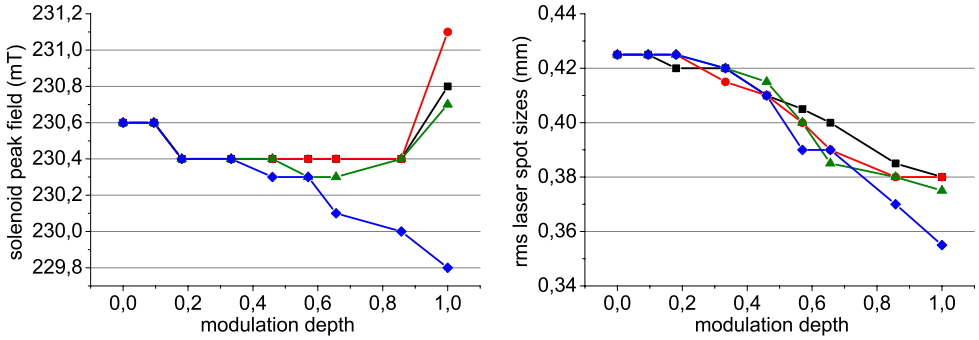

Figure 7.17: *Optimized solenoid peak field and laser spot size on the cathode while the optimum gun launch phase remained unchanged. The color code corresponds to that of figure 7.16.*

of approximately 60 %. For stronger modulations, the beam dynamics changes to a sort of multi-particle regime in which the optimum solenoid current increases for 2-4 maxima due to the high space charge density in the peaks. For five modulations the space charge density is so high, that a fraction of the charge gets lost at the cathode due to the mirror charge effect and the optimum solenoid current decreases. The optimum emission phase in the gun cavity remains almost unchanged between -2.0 and -1.5 degrees.

laser pulse profile	gun phase	duration (FWHM)	rise time	fall time	modulation depth
2 peaks					
small modulation	on-crest	20.3 ps	2.1 ps	2.4 ps	25 %
	off-crest	19.8 ps	2.0 ps	2.4 ps	27 %
medium modulation	on-crest	20.7 ps	2.4 ps	2.3 ps	28 %
	off-crest	19.4 ps	2.4 ps	2.4 ps	43 %
large modulation	on-crest	21.1 ps	2.4 ps	2.4 ps	65 %
	off-crest	20.6 ps	2.1 ps	2.0 ps	56 %
3 peaks					
small modulation	on-crest	19.3 ps	2.5 ps	3.0 ps	15 %
	off-crest	18.6 ps	2.5 ps	3.1 ps	20 %
medium modulation	on-crest	19.7 ps	2.1 ps	2.6 ps	30 %
	off-crest	19.0 ps	2.0 ps	2.5 ps	42 %
large modulation	on-crest	20.0 ps	1.8 ps	2.4 ps	46 %
	off-crest	19.8 ps	1.6 ps	2.0 ps	57 %
4 peaks					
small modulation	on-crest	18.7 ps	1.2 ps	2.5 ps	13 %
	off-crest	18.0 ps	1.3 ps	2.3 ps	35 %
medium modulation	on-crest	19.3 ps	1.3 ps	2.2 ps	36 %
	off-crest	18.6 ps	1.2 ps	2.3 ps	42 %
large modulation	on-crest	20.3 ps	1.5 ps	1.1 ps	75 %
	off-crest	19.8 ps	1.4 ps	1.3 ps	77 %

Table 7.6: *Laser pulse parameters for the temporal laser shapes used in the experiments. Note that the given numbers were obtained by a non-symmetric trapezoidal fit to the measured temporal profile. The modulation depth is the percentage by which the laser intensity drops in the valleys compared to the peaks.*

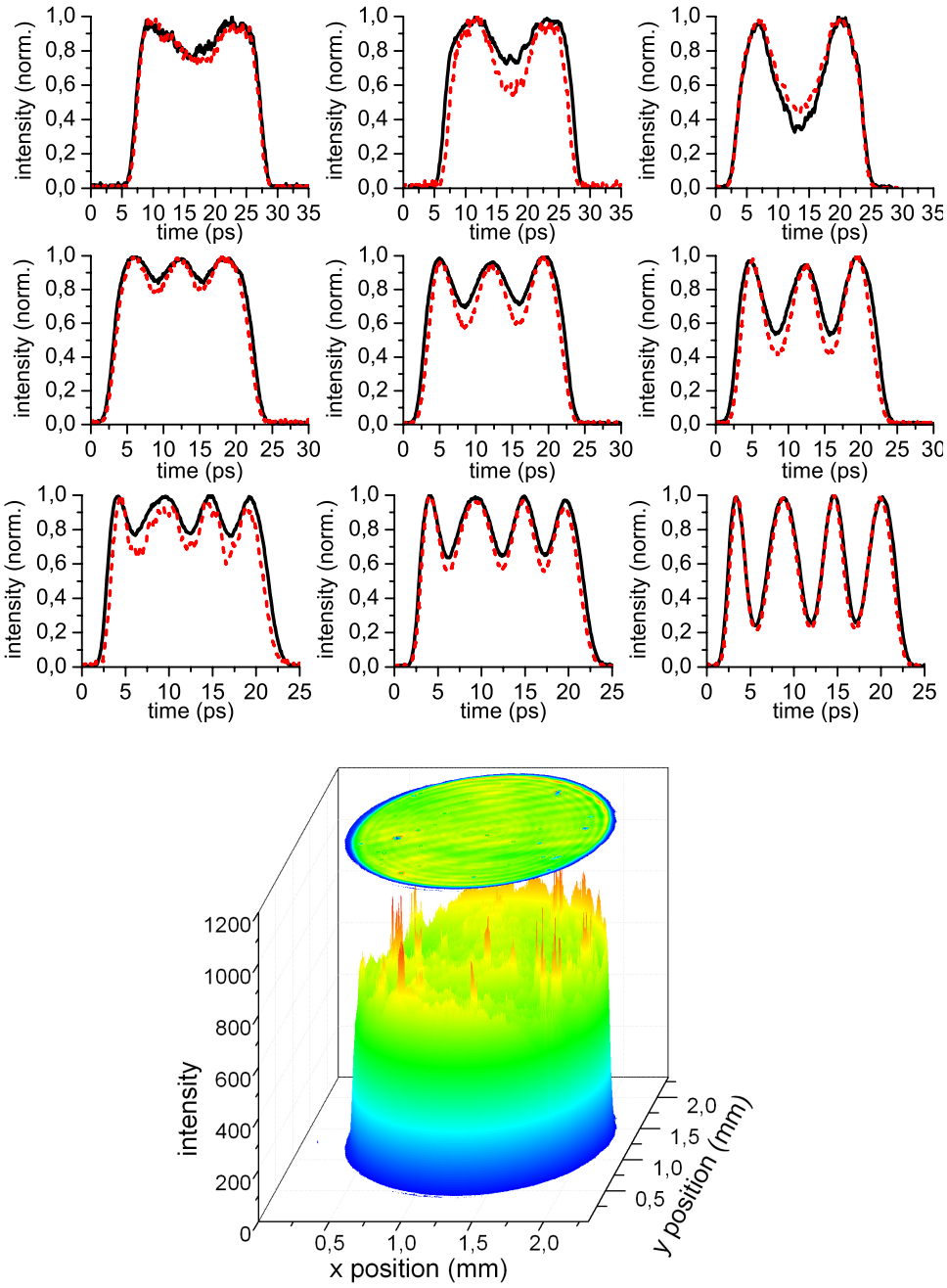

Figure 7.18: *Temporal and transverse laser profiles used for the measurements. The temporal profiles were recorded before the on-crest (black, solid line) and before the +6 degrees off-crest (red, dashed line) measurement, respectively. The transverse profile was kept constant.*

Experiments

The temporal laser shapes generated using the pulse shaper are shown in figure 7.18. Depicted are the measurements obtained before the on-crest and before the off-crest measurements of the transverse emittance. The slight differences are due to the warming-up effect of the Optical Sampling System (see section 3.4.1).
The experimental results together with the simulations of the experimental conditions are depicted in figure 7.19. The obtained transverse emittance values do not show a tendency to increase for larger modulation depths[2]. The increase of the transverse emittance expected from the simulations is very small and within the error bars of the measurement. Besides the differences in the absolute numbers obtained by simulations and experiment which was already discussed before, these measurements demonstrate that the influence of modulations on the flat-top part of the laser pulses is currently too small to be detected.

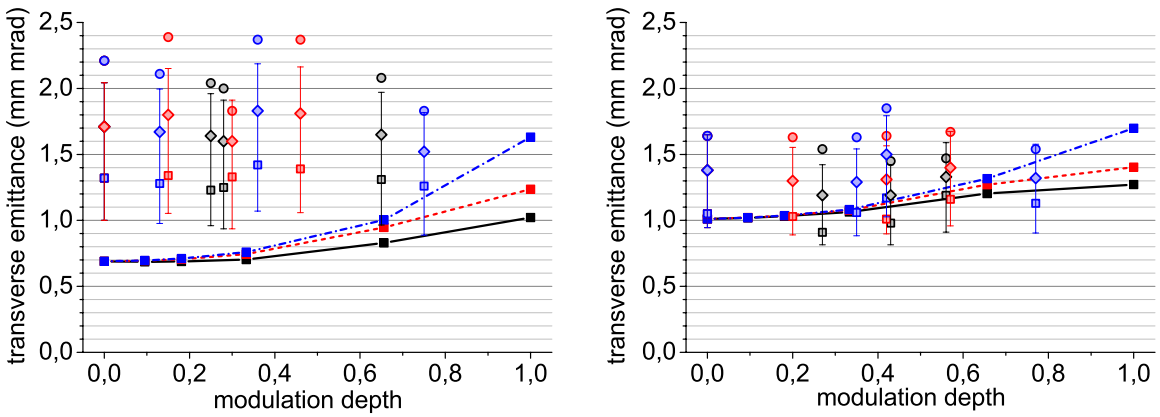

Figure 7.19: *Experimental results together with simulations. Left: Results for the gun cavity operated on-crest, right: gun cavity operated +6 degrees off-crest. The lines show the simulation results for two peaks (black, solid line), three peaks (red, dashed line) and four peaks (blue, dash-dotted line). The dots represent the measurement results using the same color code. Depicted are ε_x (squares), ε_y (circles) and ε_{xy} (diamonds). For better visibility the error bars for ε_x and ε_y are omitted.*

The fact that longitudinal space charge forces can reduce the modulations in the longitudinal phase space distribution is not valid anymore for low charges. For this reason, modulations which are imprinted in the longitudinal electron bunch density during emission caused by a modulation of the laser pulse temporal profile remain. In the case of a proper tilt of the longitudinal phase space distribution, this modulation also occurs in the momentum distribution of the electron bunch. This momentum modulation can give rise

[2]Please note, that in the simulated experiment of the 2-peak case no minimum of the transverse emittance can be found as it was the case for a fully optimized setup (see figure 7.16).

to Coherent Synchrotron Radiation (CSR) in bunch compressors and to a microbunching instability in the FEL process [Sald01]. Hence, this subject was studied in detail and is presented in the next sub-chapter.

7.6 Modulations of the momentum distribution caused by distortions on the laser pulse

When the laser system is operated as described in chapter 3, residual modulations of the flat-top part of the temporal profile cannot be avoided. This is a result of the stacking of short, mutually delayed Gaussian pulses to obtain the long flat-top profile. Since the response time of the cathode is small, the temporal shape of the laser pulse is imprinted in the longitudinal phase space distribution as a modulation of the bunch current. At high bunch charges, these modulations in the longitudinal phase space distribution can be reduced by the longitudinal space charge forces.

In figure 7.20, the dependence of the modulation depth in the momentum spectra on the bunch charge measured downstream of the booster cavity is shown [Haen]. The gun and booster cavities were operated at 60 MV/m and 14 MV/m, respectively. Both cavities were run at +10 degrees off-crest to provide an elongation of the longitudinal phase space distribution along the energy axis. This was necessary to match the modulation frequency in the momentum spectra to the resolution of the momentum measurement system. For 1 nC, almost no modulation is visible whereas for 500 pC and 250 pC these modulations are clearly present.

To reduce the modulations on the flat-top part of the temporal laser profile, a Lyot-filter can be inserted in the regenerative amplifier of the laser system. Depending on the filter properties, it reduces the spectral bandwidth of the laser pulses which leads to a flattening

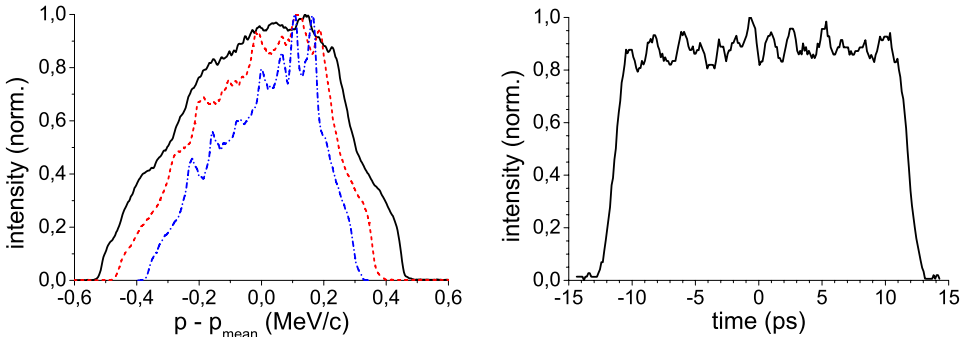

Figure 7.20: *Momentum distributions for 1 nC (black solid line), 500 pC (red dashed line) and 250 pC (blue dash-dotted line) measured downstream of the booster cavity. The right graph shows the used temporal laser profile.*

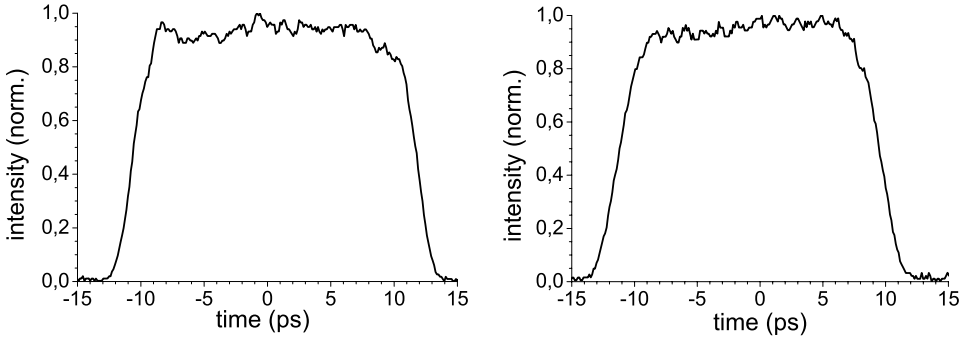

Figure 7.21: *Temporal laser pulse profiles obtained with inserted Lyot filters. Left graph: medium bandwidth filter, Right graph: small bandwidth filter.*

of the flat-top but also increases the rise and fall times. The resulting temporal profiles which are obtained after insertion of two different Lyot-filters are depicted in figure 7.21 (the Lyot-filters were named after the bandwidth they transmit). The temporal laser profile without application of a Lyot-filter was already shown in figure 7.20 (right). The corresponding pulse properties are summarized in table 7.7.

filter type	duration (FWHM)	rise time	fall time	modulation on flat-top
no Lyot-filter	23.3 ps	2.0 ps	1.8 ps	11.8 %
medium bandwidth filter	22.3 ps	3.2 ps	3.0 ps	9.8 %
small bandwidth filter	20.7 ps	4.1 ps	3.9 ps	7.0 %

Table 7.7: *Laser pulse parameters for the temporal laser shapes used in the experiments. The modulation is calculated as* $\frac{max-min}{2\,mean} \cdot 100\%$ *on the flat-top part.*

Using these temporal laser profiles, the momentum spectra were measured downstream of the gun cavity and after the booster cavity. For best detection of the modulations a bunch charge of 250 pC was used. The gun was operated at a maximum field at the cathode of 64 MV/m and the booster cavity at 14 MV/m, the phase was chosen to be +10 degrees off-crest for both cavities. The BSA had a diameter of 1.5 mm.
In figure 7.22 the measurement results are shown. Again, the modulations in the momentum distribution are present for the case in which no filter is applied. For the medium bandwidth filter, the modulations are suppressed to a large extent and with the small bandwidth filter applied no modulations are detectable anymore. This is true for the measurements downstream of the gun cavity as well as after the booster cavity.

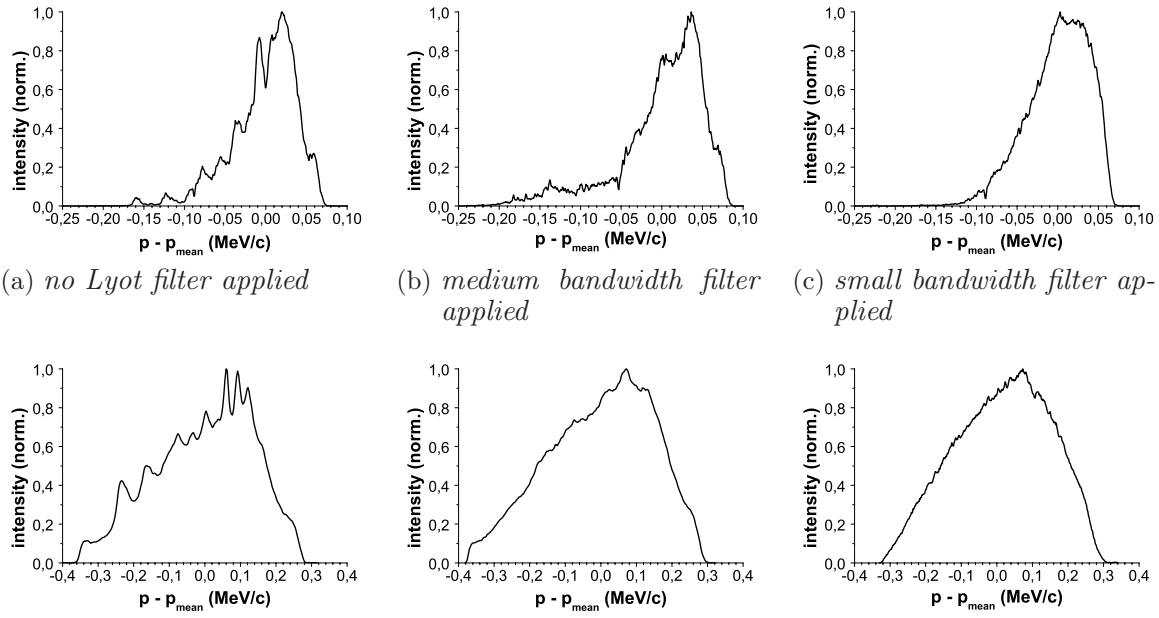

(a) *no Lyot filter applied* (b) *medium bandwidth filter applied* (c) *small bandwidth filter applied*

(d) *no Lyot filter applied* (e) *medium bandwidth filter applied* (f) *small bandwidth filter applied*

Figure 7.22: *Momentum distributions measured downstream of the gun cavity (top row) and downstream of the booster cavity (bottom row).*

To get further insight, simulations were performed based on a flat-top temporal laser pulse profile with a duration of 20 ps (FWHM) and 2 ps rise and fall times. On the flat-top part of the profile, sinusoidal modulations were introduced with depths much smaller than in the previous section. The bunch charge was 250 pC and transverse laser pulse shape was a circular flat-top with a spot size of $x_{rms} = y_{rms} = 0.34\,\mathrm{mm}$. The machine parameters are equivalent to those described earlier in the experimental part. The solenoid magnetic field strength was set to $B_{\mathrm{peak}} = 0.224\,\mathrm{mT}$ in order to transport the electron bunch up

temporal profile	duration (FWHM)	rise time	fall time	modulation on flat-top
no modulation	20.0 ps	2.0 ps	2.0 ps	0.0 %
small modulations	20.0 ps	2.4 ps	2.3 ps	4.7 %
medium modulations	20.0 ps	2.0 ps	1.9 ps	6.1 %
large modulations	19.9 ps	1.5 ps	1.6 ps	9.9 %

Table 7.8: *Laser pulse parameters for the temporal laser shapes used in the simulations. These values were obtained using the same algorithm that was used for the laser profiles in the experiments.*

to the momentum measurement station downstream of the booster cavity. The temporal laser profiles which have been used for the simulations are shown in figure 7.23 and the laser pulse parameters are summarized in table 7.8. The results of the simulations are shown figure 7.24.

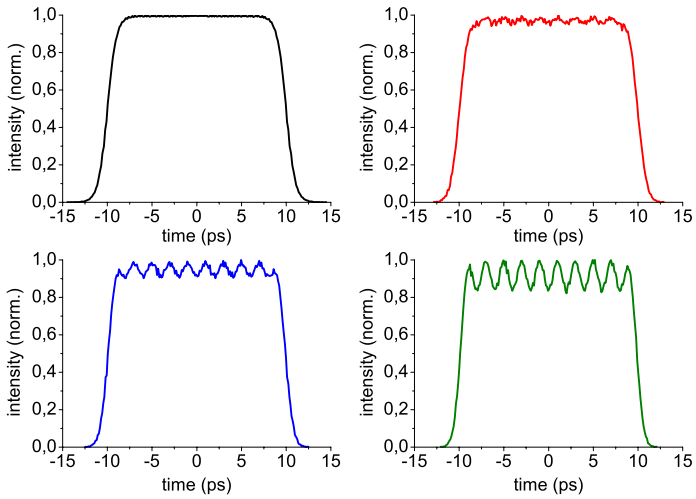

Figure 7.23: *Temporal laser profiles used in the simulations. These profiles are histograms of the particle distributions used for the simulations. The residual fluctuations on the profiles is due to numerical noise.*

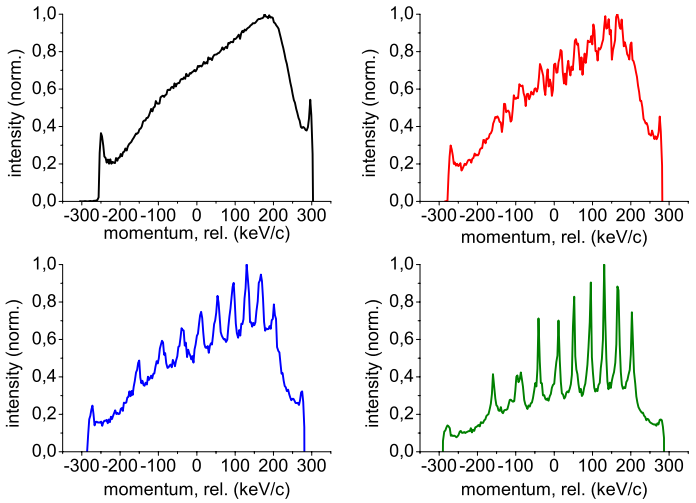

Figure 7.24: *Momentum distributions downstream of the booster cavity obtained by simulations. The color code corresponds to that of figure 7.23.*

Even for very small modulations on the temporal laser profile, significant modulations on the momentum distribution can be observed. Note that the modulation depths of the measured case without Lyot filter and the simulated case with the largest modulation are very similar. Convoluting the simulated momentum distribution with the response function of the momentum measurement device, which is a Gaussian distribution with a width of 8 keV/c (FWHM), results in a distribution which is in good agreement with the measured one, as it can be seen in figure 7.25.

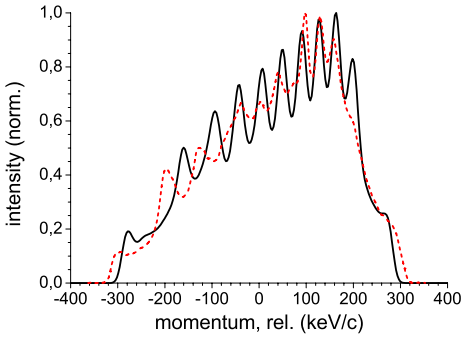

Figure 7.25: *Comparison of the simulation (black solid line) and the measured momentum distribution (red dashed line)*

In summary, the modulations of the flat-top of the temporal laser profiles are translated into a corresponding structure on the longitudinal phase space distributions. Depending on the bunch charge, these modulations can be reduced due to longitudinal space charge forces. At low bunch charges, these modulations remain and can be observed experimentally. Due to the limited resolution of the measurement system, the longitudinal phase space distribution could not be measured directly.

7.7 Transverse laser spot size on the cathode

As presented at the beginning of this chapter, the optimum transverse laser spot size is a compromise between transverse space charge forces and the cathode emittance. The strength of the transverse space charge forces is depending on the bunch charge and the presented simulated optimal value of $x_{rms} = y_{rms} = 0.425\,\text{mm}$, which corresponds to a diameter of 1.7 mm, is only valid for a bunch charge of 1 nC. For lower charges, the transverse space charge forces are reduced and hence the optimum laser spot size is smaller. For the standard operating conditions, see table 7.1, optimizations were done for bunch charges of 100 pC, 250 pC and 500 pC. In figure 7.26, the resulting optimum laser spot sizes are shown together with the corresponding transverse emittance values for the different charges. This optimization was performed for laser pulse durations of 20 ps and

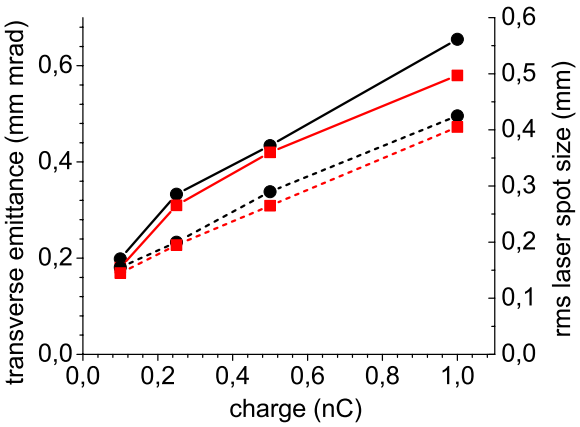

Figure 7.26: *Simulated optimum transverse emittance values (solid line) and the corresponding laser spot sizes on the cathode (dashed lines) as function of the bunch charge. Shown are simulations for a laser pulse duration of 20 ps (black curves with dots) and 24 ps (red curves with squares).*

24 ps individually, both having 2 ps rise and fall times. The reason for choosing both duration is, that the nominal pulse duration is 20 ps but the experiments were done with laser pulses having a duration of about 24 ps. The minimum transverse emittance as well as the optimized laser spot sizes are smaller for a laser pulse duration of 24 ps, because the longitudinal space charge density is smaller in this case.
In the experiments, the laser spot size was optimized by measuring the transverse emittance for the available Beam Shaping Apertures at a given bunch charge. During these measurements, a temporal flat-top laser shape with a duration of about 24 ps and rise and fall times of about 3 ps was used. The gradient in the gun cavity was about 60 MV/m and the gun phase was set to +6 degrees off-crest. The booster cavity was run on-crest at a peak electric field of 14 MV/m for 1 nC bunch charge and 10.4 MV/m for lower charges. The reason is, that lower gradients in the booster cavity allow for longer RF-pulse durations, which were needed to transport a sufficient number of electron bunches for a good signal-to-noise ratio on the observation screen during the emittance measurements. The results are shown in figure 7.27. In the top part of the graph, the diameter (in mm) of the available Beam Shaping Apertures is indicated.
For small bunch charges, the transverse emittance as well as the value of the optimal laser spot size decrease. The absolute values differ from the simulation for the following reasons. Firstly, the RF gun phase was fixed at +6 degrees and secondly, the transverse laser beam size could only be varied in steps indicated in the graph. The depicted values are the minimum transverse emittance found by a scan of the solenoid current for a given laser spot size and bunch charge. The error bars are those which were derived in Appendix D for a bunch charge of 1 nC even though they might not be straightforwardly applicable

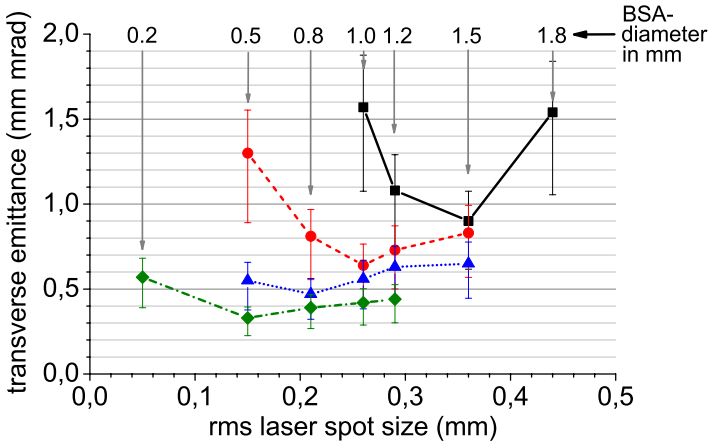

Figure 7.27: *Geometric average* $\varepsilon_{xy} = \sqrt{\varepsilon_x \varepsilon_y}$ *of the transverse emittance versus laser spot size on the cathode for different bunch charges. The measurement was done for bunch charges of 1 nC (black solid line), 500 pC (red dashed line), 250 pC (blue dotted line) and 100 pC (green dash-dotted line).*

for lower bunch charges.
A more detailed description of the electron beam dynamics at low bunch charges can be found in Appendix E.

7.8 Transverse laser pulse shape

In this section, simulations will be presented which were performed to investigate how modulations on the transverse profile of the laser pulses influence the transverse emittance. Experimental studies could not be performed, because the current setup of the laser beamline does not allow to intentionally change the shape of the transverse laser profile in a required way.
The conditions for the performed simulations are very different to those presented so far for the following reasons:

1. The computer code, that was used for the simulations [ASTRA], assigns the macroparticles to rings around the longitudinal bunch center. All of these rings are subdivided into the same number of longitudinal slices[3]. The calculation is quasi-two dimensional and assumes, that the particle distribution in the bunch is cylindrically symmetric. If this is not the case, one can also choose a three-dimensional tracking routine, which distributes the particles in cells arranged on a three-dimensional grid. This algorithm, however, has the disadvantage, that it does not support the

[3]The number of rings and longitudinal slices can be specified by the user.

simulation of the emission from the cathode. Thus, the particle tracking was split into two parts for those transverse shapes which are not cylindrically symmetric. The emission was simulated using the 2D-routine until the calculation of the mirror charge forces is stopped[4]. This happens approximately at the position of the first iris in the gun cavity (z=7.5 cm). Starting from this point, the tracking is continued with the three-dimensional code. The transverse shapes which are cylindrically symmetric were completely simulated using the 2D-code. Both approaches result in slightly different transverse emittance values. For this reason, only the relative changes of the transverse emittances compared to the case without modulation will be presented.

2. Some of the transverse shapes have modulations with a rather high spatial frequency. To properly simulate these shapes, a large number of cells is needed. In addition, each cell must contain a sufficient number of macroparticles to keep the statistical noise within reasonable limits. Therefore, the simulations were run with one million macroparticles.

3. Since the simulations are very time consuming, the evolution of the transverse emittance was calculated without booster cavity and no optimization was performed. The machine parameters were kept at the optimum values which were obtained for the case of no modulation. They are summarized in table 7.9.

Different models of transverse modulations were used in the simulations. For each of the models, the charge of the macroparticles was scaled ($q^* = q \cdot f(x, y)$) to obtain charge density variations. Afterwards, the total bunch charge was adjusted to be again 1 nC.
In the first approach, radially symmetric rings were introduced according to the formula

$$q^* = q \cdot [1 + d \cdot \cos(k \cdot r)] \tag{7.1}$$

$$k = f_s \cdot \frac{2\pi}{D}. \tag{7.2}$$

Here, d is the modulation depth, $r = \sqrt{x^2 + y^2}$ is the distance from the bunch center, D is the laser spot diameter (D=1.9 mm) and f_s is a spatial frequency which is defined as the number of oscillation along the diameter of the laser spot. A maximum at the center is obtained by choosing $d > 0$. Conversely, $d < 0$ produces a minimum at the center. The transverse laser shapes resulting from this model are shown in figure 7.29 for $d > 0$: Radial I and $d < 0$: Radial II.
The following models introduce a regular two-dimensional pattern on the transverse laser

[4]This is done automatically by the computer code when the influence of the mirror charge has become negligible.

Parameter	Value
Peak electric field in gun cavity	60 MV/m
Gun launch phase w.r.t. ϕ_{ref}	0 degree
Temporal laser shape	flat-top
Laser pulse duration	20 ps
Laser pulse rise and fall times	2 ps
Transverse laser shape	circular flat-top
Initial kinetic energy	E_{kin}=0.55 eV
Optimized values	
Solenoid peak field	234 mT
Laser spot diameter	1.9 mm ($x/y_{rms} = 0.45$ mm)
Transverse emittance (2D&3D)	0.95 mm mrad @ z=3.29 m
Transverse emittance (only 2D)	0.86 mm mrad @ z=3.24 m

Table 7.9: *Machine parameters used for the simulation and optimized values. Note that the emittance values are larger than in the previous chapters because the simulations were performed without booster cavity.*

profiles. The formulas used for the generation of these profiles are

$$q^* = q \cdot [1 + d \cdot \cos(k \cdot x)] \cdot [1 + d \cdot \cos(k \cdot y)] \quad \text{and} \tag{7.3}$$

$$q^* = q \cdot [1 + d \cdot \sin(k \cdot x)] \cdot [1 + d \cdot \sin(k \cdot y)] \,. \tag{7.4}$$

The result of the first formula is sensitive to the choice of the sign of d, while this is not true for the second expression. Here, the transverse profiles produced by opposite signs of d can be translated into each other by a rotation of 180 degrees. Since, the external forces occurring in the simulations are rotationally symmetric, both distributions give equivalent results.
The transverse shapes are shown in figures 7.28 (a)-(d) for the sine-like modulation (Sine) as well as (e)-(h) and (i)-(l) for the cosine-like modulation with $d > 0$ (Cosine I) and $d < 0$ (Cosine II), respectively.
In addition, figure 7.30 illustrates the different modulation depths used for the simulations. The results of the simulations are shown in figure 7.31 (Sine and Cosine shapes) and figure 7.32 (radially symmetric shapes). From these graphs, the following conclusions can be drawn. For larger modulation depths, the change of transverse emittance is more pronounced. In general, the transverse emittance increases except for those modulation models which produce one single maximum of charge density in the center of the transverse profile (Cosine I and Radial I with $f_s = 0.5$). In these cases, the transverse emittance is reduced by about 15 % at modulation depths in the range of 20-30 %. There are several reasons for this behavior.

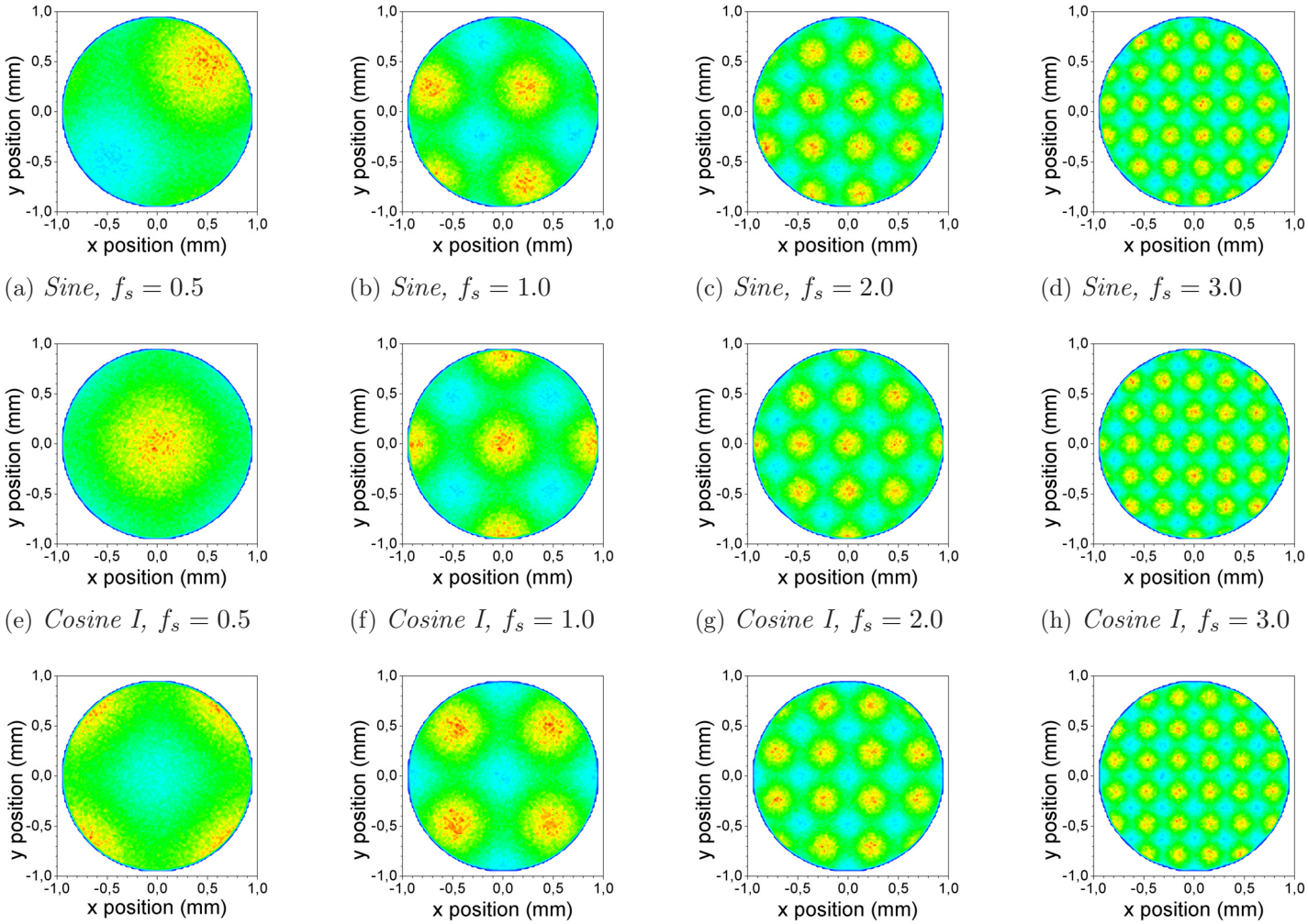

(a) *Sine*, $f_s = 0.5$ (b) *Sine*, $f_s = 1.0$ (c) *Sine*, $f_s = 2.0$ (d) *Sine*, $f_s = 3.0$

(e) *Cosine I*, $f_s = 0.5$ (f) *Cosine I*, $f_s = 1.0$ (g) *Cosine I*, $f_s = 2.0$ (h) *Cosine I*, $f_s = 3.0$

(i) *Cosine II*, $f_s = 0.5$ (j) *Cosine II*, $f_s = 1.0$ (k) *Cosine II*, $f_s = 2.0$ (l) *Cosine II*, $f_s = 3.0$

Figure 7.28: *Transverse laser shapes used in the simulations. First row: sine-like modulations, second row: cosine-like modulation with maxima at the center, third row: cosine-like modulation with minima at the center. In all cases, a modulation depth of 0.3 was used.*

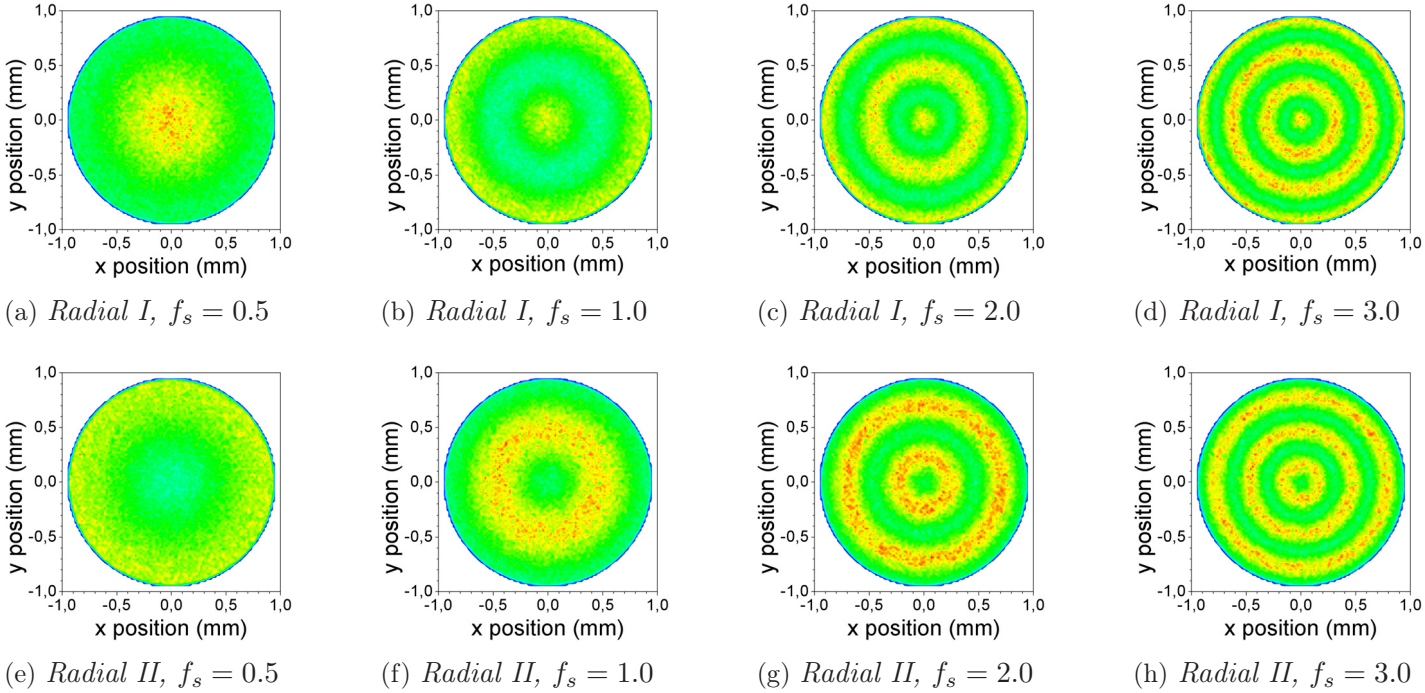

(a) *Radial I,* $f_s = 0.5$ (b) *Radial I,* $f_s = 1.0$ (c) *Radial I,* $f_s = 2.0$ (d) *Radial I,* $f_s = 3.0$

(e) *Radial II,* $f_s = 0.5$ (f) *Radial II,* $f_s = 1.0$ (g) *Radial II,* $f_s = 2.0$ (h) *Radial II,* $f_s = 3.0$

Figure 7.29: *Transverse laser shapes used in the simulations. First row: radially symmetric cosine-like modulation with maxima at the center, second row: the same with minima at the center. A modulation depth of 0.3 was used.*

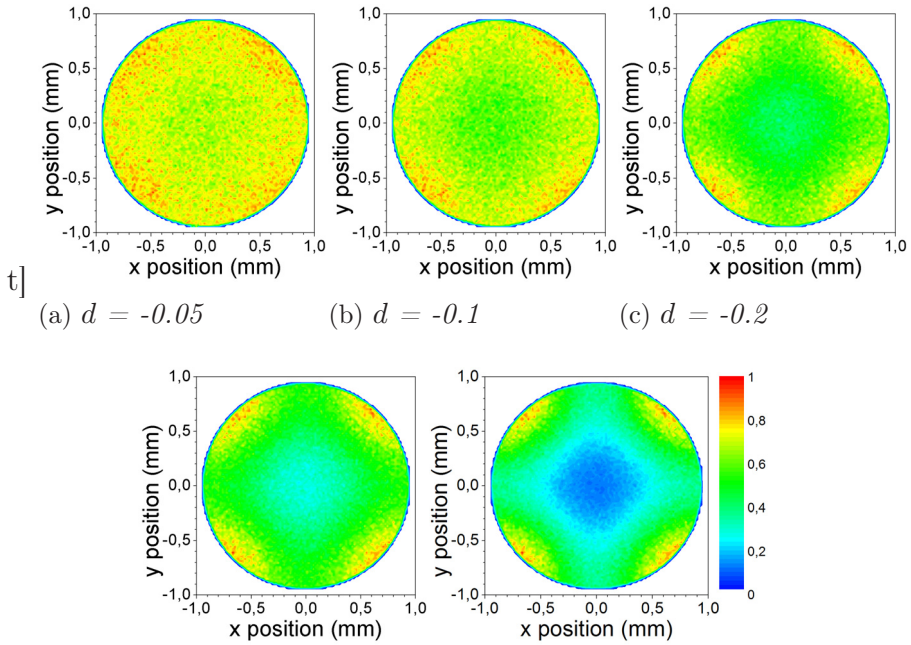

t]

(a) d = *-0.05* (b) d = *-0.1* (c) d = *-0.2*

(d) d = *-0.3* (e) d = *-0.5*

Figure 7.30: *Modulation depths that were used in the simulations. As an example the cosine-like modulation with f_s=0.5 was chosen.*

Firstly, the transverse shapes with a maximum in charge density at the center correspond to smaller transverse laser spot size. This reduces the contribution of the cathode emittance. Secondly, even though the maximum at the center imposes nonlinearities in the transverse space charge forces, this - usually detrimental effect - is compensated by the fact that more charge is located close to the bunch center and therefore, the rms transverse emittance becomes smaller. Furthermore, towards larger modulation frequencies, the increase in transverse emittance becomes less pronounced. This is an effect of the transverse space charge forces which tend to reduce the high-frequency modulations. Furthermore, the emittance increase becomes almost equal for similar transverse shapes (the sine/cosine-shapes on one hand as well as the radially symmetric shapes on the other hand) at high modulation frequencies. And finally, the highest value of transverse emittance increase can be observed for transverse shapes which are deviating most from the cylindically symmetric shapes and/or in which the maxima of the charge density distribution are located away from the center.

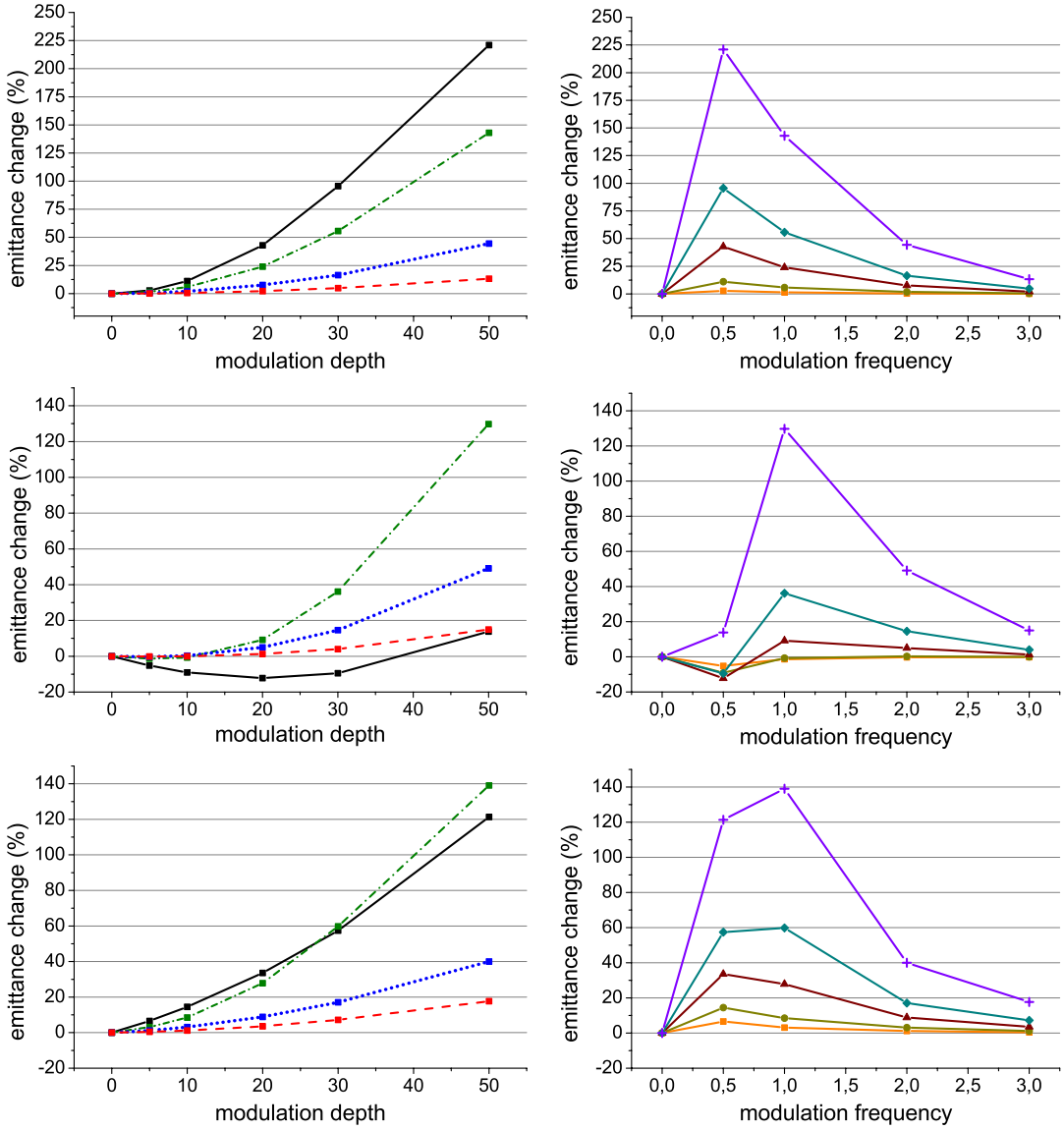

Figure 7.31: *Results of the simulations for the non-radially symmetric modulation types Sine (top row), Cosine I (middle row) and Cosine II (bottom row). Depicted is the percentage of emittance change depending on the modulation depth (left) and the modulation frequency (right). In the left graphs, the modulation frequencies* $f_s = 0.5$ *(black solid line),* $f_s = 1.0$ *(green dash-dotted line),* $f_s = 2.0$ *(blue dotted line) and* $f_s = 3.0$ *(red dashed line) are shown. The right graphs display the modulation depths of* $d = 0.05$ *(orange squares),* $d = 0.1$ *(gold circles),* $d = 0.2$ *(brown triangles),* $d = 0.3$ *(cyan diamonds) and* $d = 0.5$ *(violet crosses).*

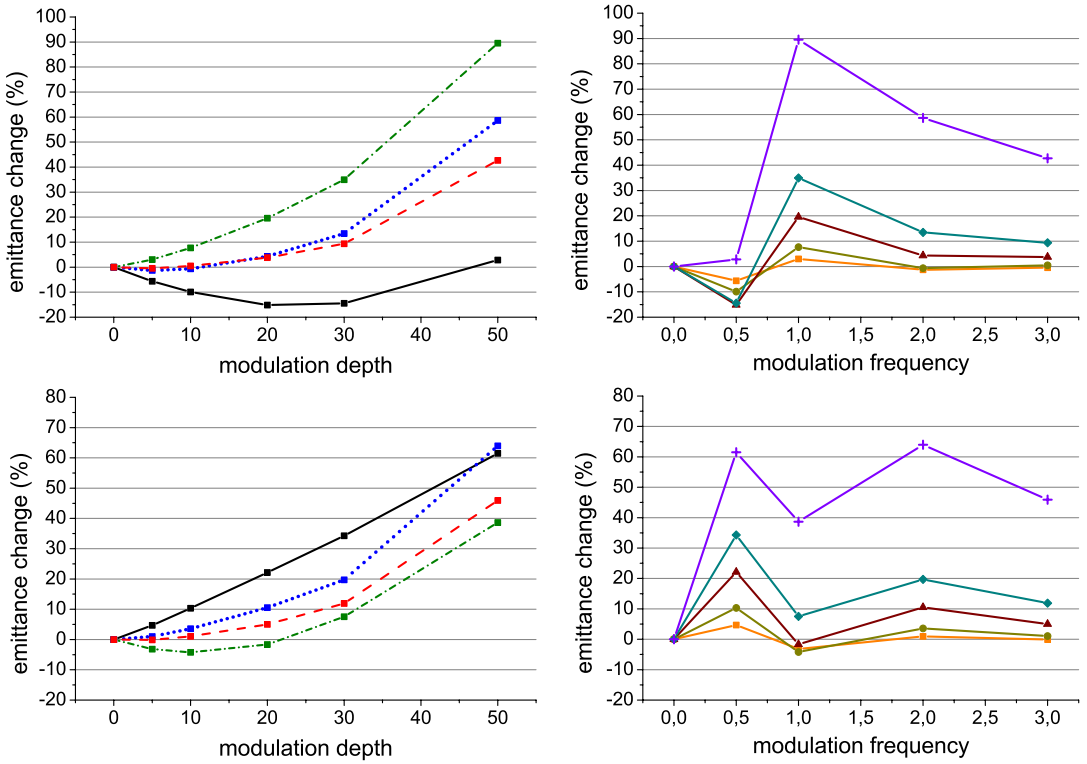

Figure 7.32: *Results of the simulations for the radially symmetric modulation types Radial I (top row) and Radial II (bottom row). The graphs and color codes correspond to those of figure 7.31.*

In summary, the increase of the transverse emittance is most sensitive to transverse shapes in which the center of gravity of the charge density distribution is not the geometric center of the bunch. Furthermore, transverse shapes should be avoided in which the charge density has maxima away from the bunch center.
The presently used scheme of cutting a Gaussian transverse laser distribution by a hard edged circular hole has proven to be beneficial over the perfect flat-top shape. And finally, the diffraction patterns shown in figure 3.12, which occur when the photocathode is not exactly placed in the image plane, have a spatial frequency which is too high to cause a significant increase of the transverse emittance. On the other hand, the fact that the geometric center of the transverse laser shape does not coincide with the center of gravity is much more severe.

Chapter 8

Summary and outlook

The successful operation of Free Electron Lasers such as FLASH in Hamburg and especially the future European XFEL require electron sources which are capable of producing electron bunches of very high quality. One of the key components of the electron bunch production is the photocathode laser system since it allows to influence the electron bunch properties by adjusting the temporal and spatial characteristics of the laser pulses used to extract the photoelectrons. For this reason, the first part of the thesis was dedicated to a thorough investigation of the laser system which is currently installed at PITZ (built by MBI Berlin) including the laser beam transport system. The results are briefly summarized as follows:

- The temporal laser shapes measured with the Optical Sampling System are in good agreement with the measurements using an independent device (streak camera Hamamatsu FESCA200) having a comparable temporal resolution. It was also shown that this level of precision requires the Optical Sampling System to be adjusted very accurately (see chapter 3.4.1).

- The influence of the laser beam transport system on the temporal laser shape is negligible.

- Within a train of 40 pulses, no difference between the temporal shapes of the laser pulses could be detected.

- A dependence of the temporal laser profile on the transverse position in the pulse was found. Since only the center part of the whole beam is transmitted through the Beam Shaping Aperture, the remaining variation is small.

- The laser material which is used in the current laser system shows the effect of thermal lensing. This effect can be reduced by proper imaging of the laser pulses in the laser system itself as well as in the laser beam transport system to the photocathode. Even though strong efforts were made to provide optimum imaging conditions, it

was found that the effect of thermal lensing still causes a change of the laser pulse properties along the pulse trains. Operation with long laser pulse trains in which each laser pulse has the same properties appears to be impossible with the current setup. On the other hand, this did not compromise the measurement of transverse emittance since it requires only short pulse trains with less than forty pulses.

- Finally, the importance of accurate alignment of the laser pulses on the inner vacuum was demonstrated.

In the second part of the thesis, the influence on the laser pulse parameters on the electron bunch properties was investigated. This is of great importance, since the results define which laser pulse properties are the most critical and therefore give a baseline for future photocathode laser developments. The findings were:

- Simulations showed that the transverse emittance should decrease for longer laser pulse durations while the longitudinal emittance increases. Experimentally, this behavior could be observed only in the case of an RF emission phase of +6 degrees whereas for on-crest acceleration the transverse emittance increased. The reason for this behavior is not yet fully clear but there is evidence that the observed low RF phase stability had a strong impact on the measurement results.

- Optimizing the machine parameters to get minimal transverse emittance for laser pulses with different rise and fall times led to the result, that for rise and fall times larger than 1 ps the increase of the transverse emittance is almost linear. On the other hand, the simulation of the specific measurement conditions resulted in an almost constant transverse emittance which was also found experimentally.

- The influence of modulations on the flat-top part of the laser pulses was investigated. Simulations show that the increase of the transverse emittance is less than 10 % for a modulation depth of less than 40 % for up to five peaks. Because of the large error in the measurement of the transverse emittance due to th RF phase instabilities, these small changes could not be identified in the measured values.

- In case of small bunch charges, modulations on the temporal flat-top of the laser pulse which are translated into modulations on the longitudinal phase space distribution during emission cannot be reduced by longitudinal space charge forces. These modulations remain during transport of the electron beam and can be detected as modulation of the momentum distribution. This could be confirmed experimentally.

- The tendency that for low bunch charges the optimum transverse emittance and the corresponding transverse laser spot size decrease was found in simulations and confirmed experimentally. For example, at a bunch charge of 1 nC the minimum transverse emittance was measured to be $\varepsilon_{xy}^{1\mathrm{nC}}$=0.9 mm mrad using a laser spot size

of x/y_{rms}=0.36 mm mrad while at 250 pC the minimum was found to be $\varepsilon_{xy}^{250\mathrm{pC}}$= 0.47 mm mrad for a laser spot size of x/y_{rms}=0.21 mm mrad. The given values were obtained without applying a charge cut.

- Detailed simulations were performed to investigate the dependence of modulations of the transverse laser profile on the transverse emittance. It was found that a single maximum of the charge density at the center of the transverse laser distribution which naturally occurs in the current laser beamline setup, can result in a reduction of the transverse emittance of up to 15 %. Higher modulation frequencies cause less increase in transverse emittance and hence the diffraction patterns which occur when the photocathode is not exactly in the image plane are not causing a significant increase of the transverse emittance. This is valid only when the geometric center and center of gravity of the transverse laser pulse shape are identical.

Outlook

The next step is to repeat the measurements of the transverse emittance with an improved RF phase stability in the gun cavity. This would allow to decide which tolerances in the photocathode laser pulse properties are acceptable for the operation of ax X-ray free electron laser such as the future European XFEL.
Furthermore, measuring the transverse emittance with additional experimental techniques leads to a better understanding of the underlying processes. At the moment, several new techniques are under development at PITZ, e.g. tomographic reconstruction of the transverse phase spaces as well as slice emittance measurement methods.
In the mid-term future, it is planned to install a transverse deflecting cavity in the PITZ beamline. Together with a dispersive section, the longitudinal phase space can be measured with a much higher precision than possible so far. This new tool would allow to get a better insight into the longitudinal electron beam dynamics at low bunch charges.

Appendix A

The transverse laser pulse shape near the image plane

The following images show the transverse profiles of the laser beam at different distances before and behind the imaging plane (denoted as nominal position which should actually be the photocathode). The transverse distribution at the imaging plane shows the sharp edges from the beam shaping aperture as well as the cut transverse Gaussian distribution from the laser which is slightly shifted to the lower left edge in this case. The change of the transverse distributions before and behind the imaging plane are symmetric and the expected diffraction patterns are clearly visible as rings around the center. For larger distances from the imaging plane the number of the rings decreases and the modulation depth becomes large also in the center.
Note, that the scaling of the color code is different for each image. The speckles which are visible on some of these images result from dust on the cover glass of the camera. The used Beam Shaping Aperture had a diameter of 1.5 mm. This laser spot size was chosen because it was used during the measurements of the lowest transverse emittance. The horizontal and vertical axes range from -1.2 mm to +1.2 mm.

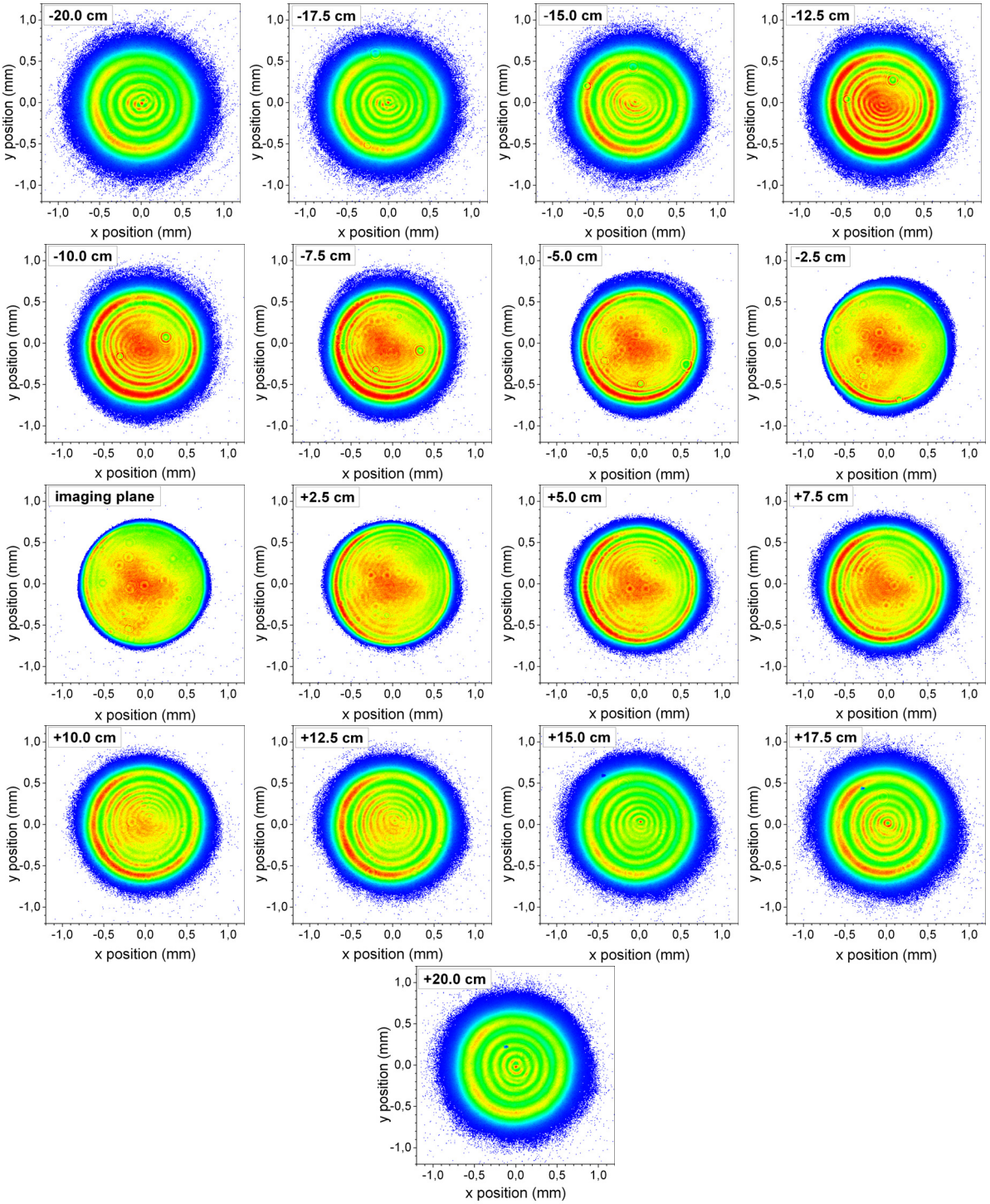
-20.0 cm
-17.5 cm
-15.0 cm
-12.5 cm
-10.0 cm
-7.5 cm
-5.0 cm
-2.5 cm
imaging plane
+2.5 cm
+5.0 cm
+7.5 cm
+10.0 cm
+12.5 cm
+15.0 cm
+17.5 cm
+20.0 cm
x position (mm)
y position (mm)
1,0
0,5
0,0
-0,5
-1,0

The next set of images displays the same for a Beam Shaping Aperture of 0.2 mm diameter which is the smallest available laser spot size. Here the change of the profile is more pronounced. From the image at the nominal position one can see that the small Beam Shaping Aperture hole contains some dirt. Here the axes range from -0.55 mm to +0.55 mm.

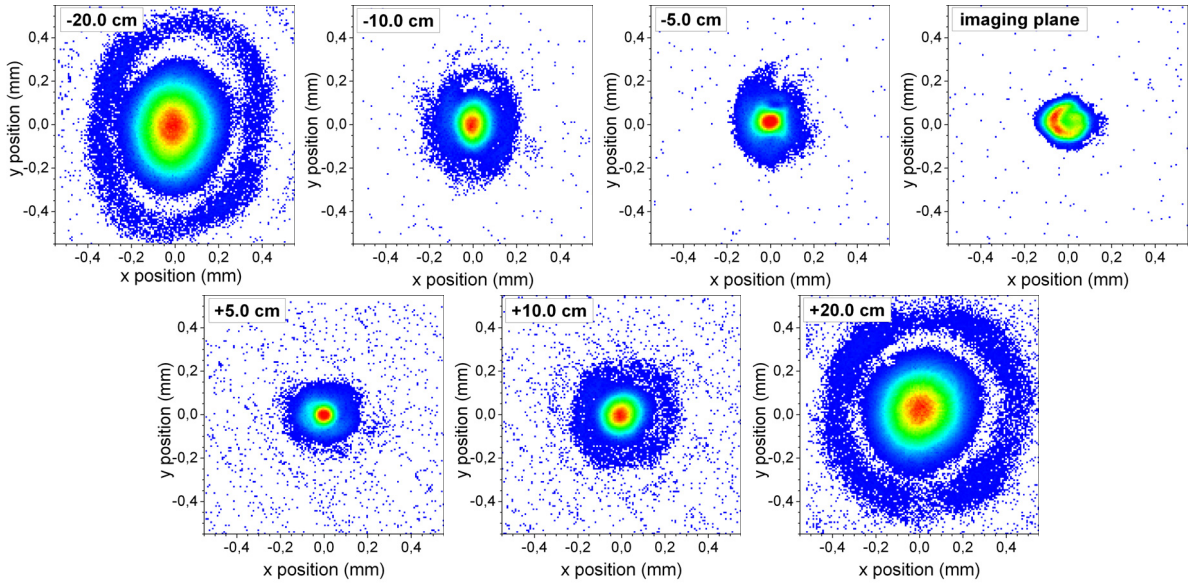

Appendix B

Signal decay under UV light exposure at Jai M10SX cameras

When using non UV-capable cameras the actual transverse laser pulse profile can be overlayed by another contribution coming from an decay mechanism, which is most likely fluorescence in the protection cover plate, caused by the UV light exposure. In the case of the analog cameras formerly used at PITZ this contribution was measured. For this purpose the shutter opening time of the camera was chosen as short as possible. According to the camera manual this gate time is 1.03 μs. Subsequently the camera trigger was scanned over the impinging laser pulse and the sum of pixels (SoP) versus trigger time was recorded. The result can be seen in figure B.1(a). On the left graph one can identify

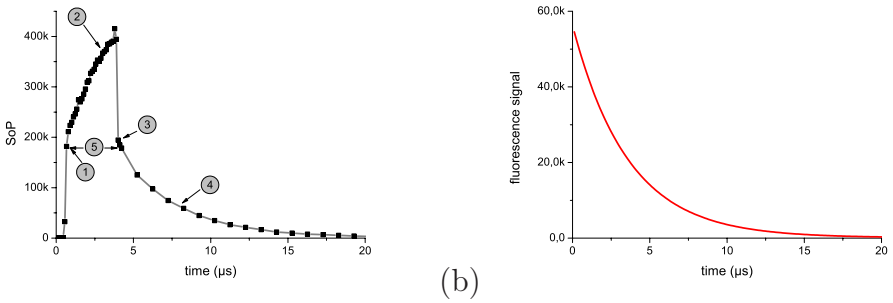

(a) (b)

Figure B.1: *(a) The sum of pixels vs. the trigger time, (b) Extracted fluorescence signal.*

three different regions. Beginning from time (1) the laser pulse is detected. Point (2) marks the region in which more and more fluorescence light is accumulated in addition to the laser pulse signal. At the time (3) the laser pulse is not inside the gate of the camera and in region (4) only fluorescence light can be detected. Furthermore one can conclude from this graph (see (5)) that the actual shutter time (gate) is about 3.2 μs in contrast to

the expected value.
Subtracting the signal from the laser pulse and deconvoluting the remaining data with the gate function one can derive the pure fluorescence light signal which is depicted in figure B.1(b) Please note the different scaling of the y-axis. This exponential decay has a characteristic time $\tau = 3.6\mu$s. Integration of the fluorescence curve gives a total SoP caused by the fluorescence of 200 600 whereas the SoP from the laser spot itself is 194000. In figure B.2 one can see the recorded transverse profiles for different timings. The first image was taken using a timing that allowed to record only the laser pulse (point (1) in figure B.1(a)). The second image shows the transverse distribution at the time of maximum Sum of Pixels (close to (2) in figure B.1(a)) and the last image was taken at time (3) when only the fluorescence contribution could be detected. The measured laser spot sizes are strongly affected by the fluorescence. While the beam size in the left image is determined to be $x_{rms} = 107\,\mu$m and $y_{rms} = 95\,\mu$m the beam size in the middle picture is significantly larger: $x_{rms} = 142\,\mu$m and $y_{rms} = 246\,\mu$m. In addition the fluorescence shows an asymmetry which is not understood.

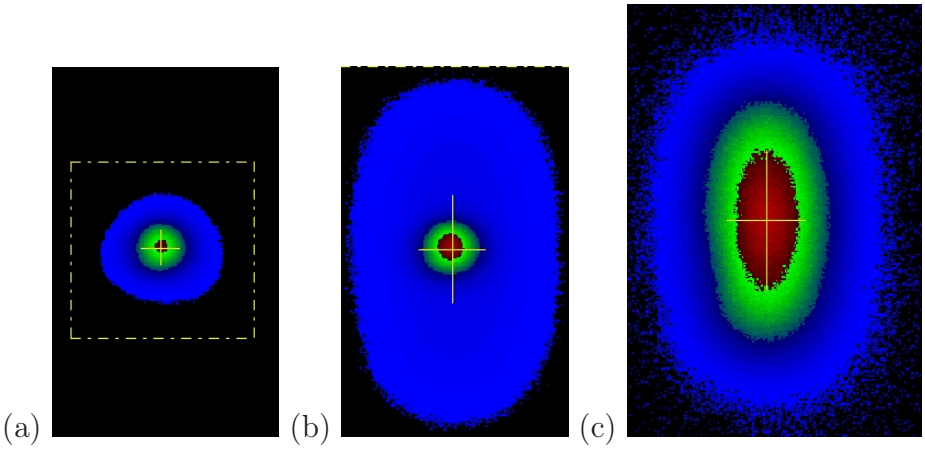

Figure B.2: *(a) only laser pulse, (b) laser pulse + fluorescence, (c) only fluorescence. Note that in (a) and (b) the color code is the same, while in (c) the color scale has been adjusted to better see the shape of the fluorescence light*

Appendix C

Technical drawings of the laser vacuum mirror

The following technical drawings show the spatial restrictions leading to the limited usable area of the vacuum inner mirror. Figure C.1 shows a view from the side into the laser entrance viewport and figure C.2 shows a view downstream from the position of the photocathode.

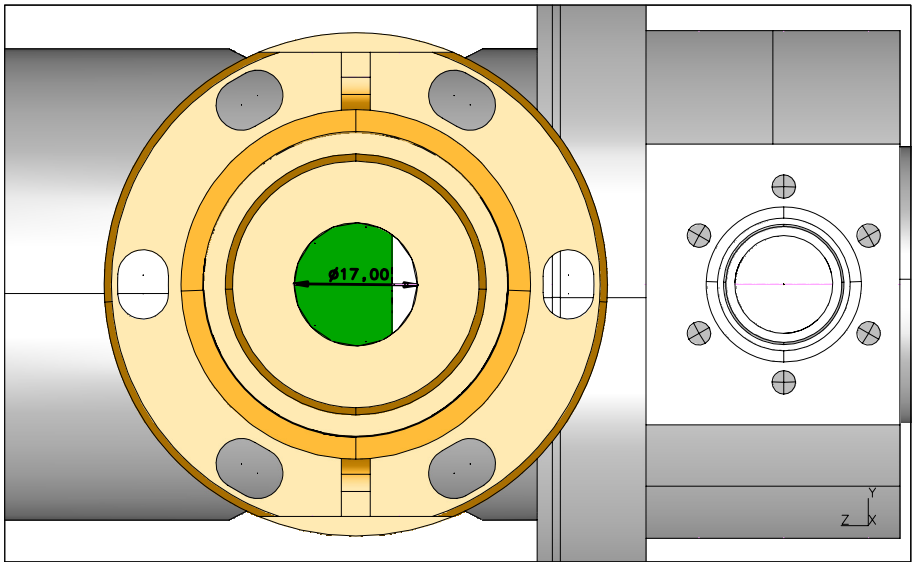

Figure C.1: *View from the viewport at which the laser beam enters the vacuum. Parts of the vacuum mirror (green) are hidden by the mechanical mounting. Only the right part of the mirror can be used for reflection to the cathode (see next Figure) which is to the right of this image.*

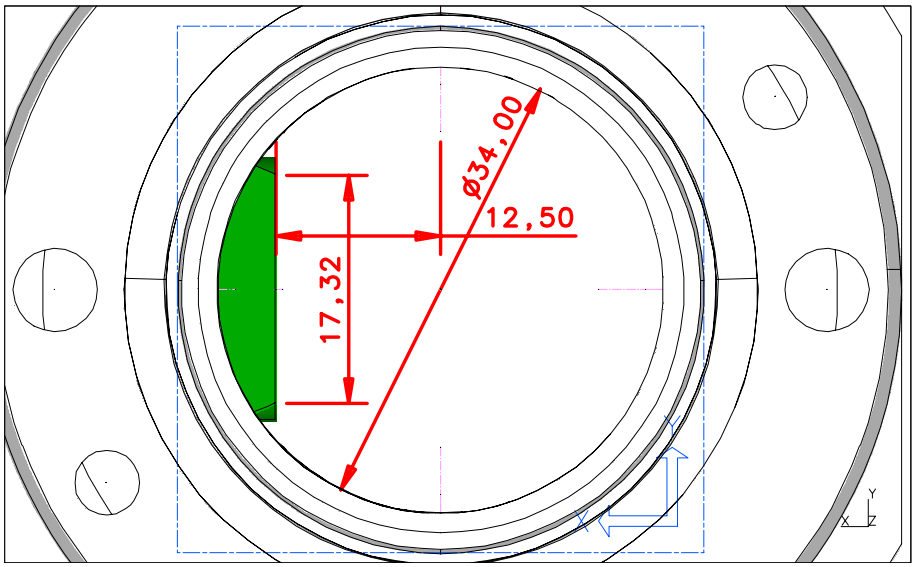

Figure C.2: *View from the cathode downstream towards the inner vacuum mirror - solid model. The area of the mirror is hidden to a large extent by the electron beam pipe.*

Appendix D

Error sources during the measurement of the transverse phase space distribution

This appendix summarizes the error sources which occurred during the measurement of the transverse emittance. These errors define the error bars that are shown in the graphs containing the measurement results.

Measurement procedure

During the measurement of the transverse emittance using the slit scan technique several error sources lead to an uncertainty of the measurement result. These are, for example:

- Uncertainty of the determination of the bunch mean momentum which is needed to calculate the relativistic scaling factor $\beta\gamma$ in equation 6.7.
- Uncertainties associated with the measurement of transverse electron bunch distribution which is needed for the determination of the transverse sizes of the whole electron bunch as well as those of the beamlets, see chapter 2.2.4:
  - Granularity of the observation screen material (usually YAG powder).
  - Resolution of the camera used to record the image of the observation screen.
  - Dynamic range of the camera.
  - Quality of the optical imaging system between screen and camera.
- Precision of the slit machining and its positioning in the beamline.

These and other error sources have been investigated in detail in [Stay, PITZ02]. It was shown that the systematic error is less than 10 % in a wide range of machine parameters.

RF phase instability

During the measurement period, it was observed that the RF phase stability in the gun is rather low. Since the gun cavity is not equipped with an RF pick up sensor, the instantaneous RF phase was calculated using the signals of the directional couplers installed in each of the two waveguides which are connected to the T-combiner of the gun cavity (see figure D.1). Each directional coupler measures the vectors of the electric field of the forward (to the gun cavity) and the reflected wave (from the gun cavity), respectively. Then, the amplitude and the phase of the electric field in the gun cavity is calculated from the vector sum of the four contributions

$$\vec{\mathbf{E}}_{\text{gun}} = \vec{\mathbf{E}}_1^{\text{forw}} + \vec{\mathbf{E}}_2^{\text{forw}} - \vec{\mathbf{E}}_1^{\text{refl}} - \vec{\mathbf{E}}_2^{\text{refl}}. \tag{D.1}$$

In figure D.1 (right) an example of a phase read back during an RF pulse is depicted. It shows that the RF phase has a slope of approx. -5 degrees/40μs. In addition to this linear dependence, the whole phase distribution had an rms jitter of about 2-4 degrees (indicated by red dotted lines in figure D.1 (right)) which could be correlated to electron beam properties like the transverse beam size or the momentum.

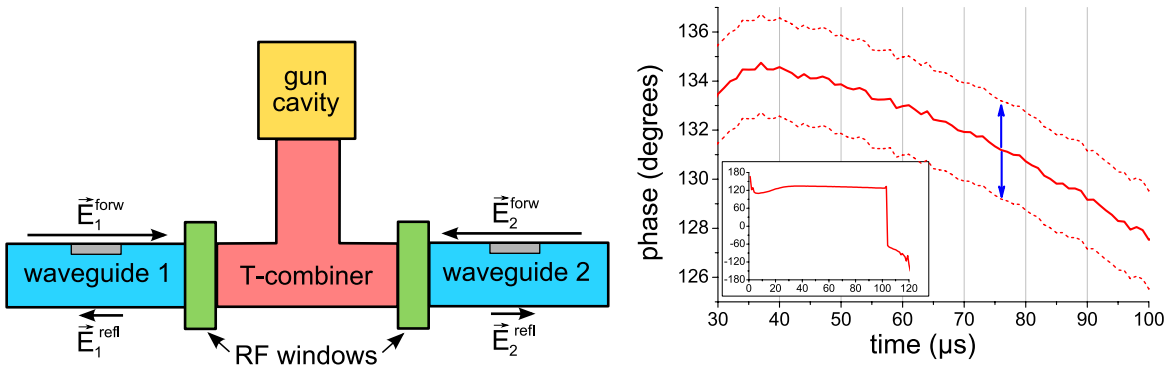

Figure D.1: *Left: Measurement of the RF amplitude and phase in the gun cavity. The electric field waves approaching in the two waveguides* $\vec{\mathbf{E}}_1^{forw}$ *and* $\vec{\mathbf{E}}_2^{forw}$ *are combined by the T-combiner and propagate to the gun cavity. Depending on the resonance conditions, the gun cavity reflects a part of the electric field. The forward and reflected waves are detected by the directional couplers in the waveguides (gray). The RF windows separate the waveguides, which are filled with* SF_6*, from the T-combiner which is under vacuum. Since these windows can transmit only up to 5 MW power, two of them must be used to reach the required power level of approx. 6.6 MW in the gun cavity. Right: Example of a phase measurement. The RF pulse has a duration of 60 µs and the electron bunch train is emitted starting from 40 µs in this graph. The inset shows the overall phase dependence during the filling time of the cavity, the plateau part and the end of the RF pulse.*

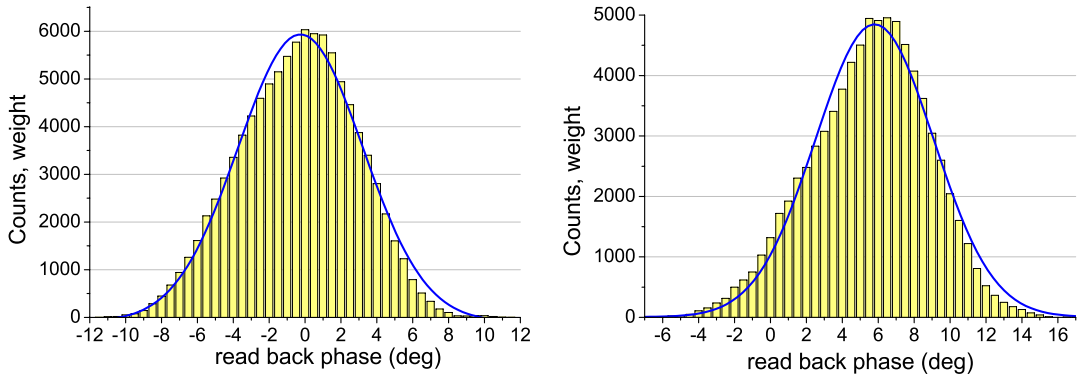

Figure D.2: *Histograms of the phase distributions for on-crest RF phase (left) and +6 degrees off-crest RF phase. By fitting a Gaussian curve, the widths were determined to be* $\sigma_\phi^{oncrest}$*=3.5 degrees and* $\sigma_\phi^{+6\,degrees}$*=3.3 degrees, respectively.*

To further investigate the influence of these phase fluctuations, the RF phase distributions, as shown in figure D.1 (right), were recorded during one measurement of the transverse emittance. Since in this measurement a train of 20 electron bunches was used, the time window between 40 μs and 60 μs was selected. From this data, phase histograms were created for two different gun RF phases. Firstly, the phase of maximum mean momentum gain (on-crest phase) was chosen because simulations predict that this results in almost the smallest transverse emittance. Secondly, the phase of +6 degrees from the on-crest phase was investigated. This phase was the experimentally found optimum. The results can be seen in figure D.2. As a next step, the measurement conditions were simulated using the

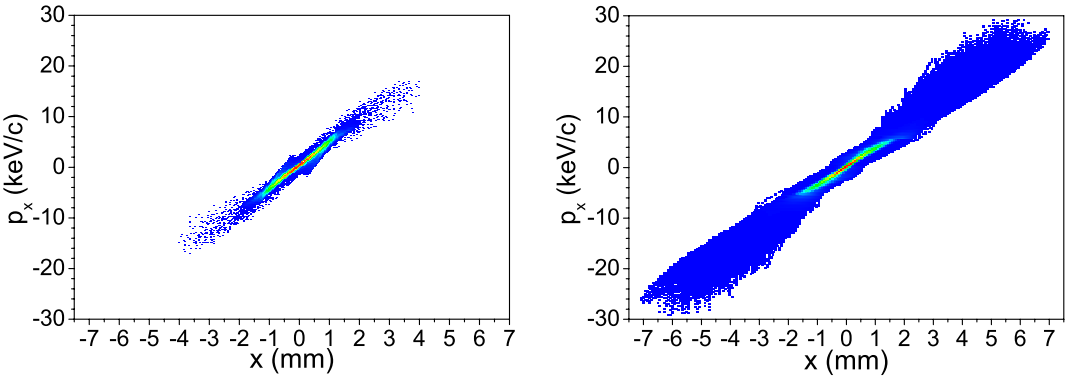

Figure D.3: *Left: Simulated transverse phase space for the emission phase of maximum mean momentum gain. The transverse emittance is* ε_x*=0.69 mm mrad. Right: Overlap of transverse phase spaces for different emission phases weighted according to the phase histogram of figure D.2 (left). The resulting transverse emittance is* ε_x*=0.89 mm mrad.*

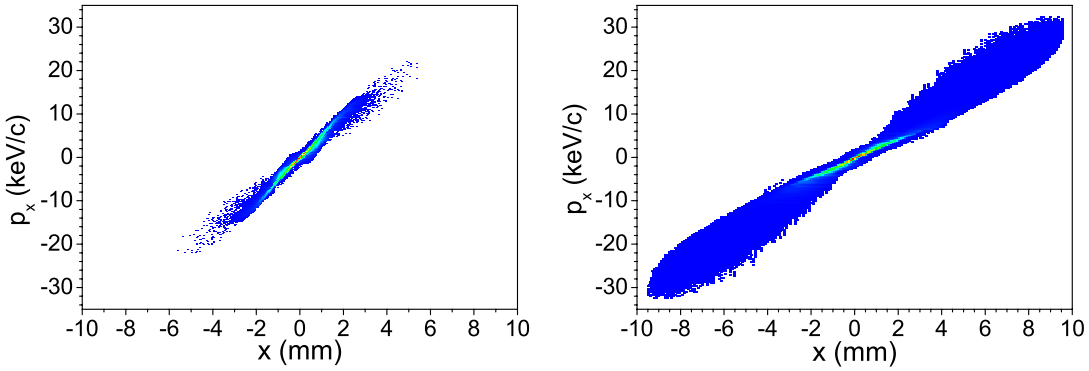

Figure D.4: *Left: Simulated transverse phase space for the emission phase of +6 degrees off-crest. The transverse emittance is ε_x=1.23 mm mrad. Right: Overlap of transverse phase spaces for different emission phases weighted according to the phase histogram of figure D.2 (right). The resulting transverse emittance is ε_x=1.39 mm mrad.*

code ASTRA. The temporal laser shape was a flat-top with a duration of 20 ps (FWHM) and rise and fall times of 2 ps, the maximum electric field in the gun cavity was set to 60 MV/m while for the booster cavity 14 MV/m was chosen. The RF phase of the booster cavity corresponds to the phase of maximum mean momentum gain. The transverse laser shape was a circular flat-top with a diameter of 1.7 mm. The simulated transverse phase spaces at the position of the first emittance measurement station obtained for different emission phases were overlapped according to the weights given by the measured phase histograms. The results are shown in figure D.3 and D.4.
The main conclusion of these investigations is that the relative increase of transverse emittance in the case of on-crest emission is about 29 % while for an emission at +6 degrees off-crest phase the increase is only about 13 %.
These findings may partially explain why the smallest transverse emittance was found at +6 degrees emission phase instead of the predicted -1.5 deg.
Finally, it must be mentioned that the phase instability does not only increase the area of the transverse phase space distribution. It also causes difficulties in the determination the phase of maximum mean momentum gain and in the measurement the transverse beam size of the electron bunch. Further, since the the phase fluctuations cause changes in the electron bunch momentum, the action of steerer magnets on the electron bunch varies. This leads to a transverse position jitter of the electron beam. These effects cause further uncertainties which are not discussed here.

Cathode emittance

The cathode emittance derived in chapter 6.2.1 depends on the transverse laser spot size and the initial kinetic energy of the electrons escaping from the photocathode into the vacuum. While the first parameter can be varied, the initial kinetic energy of the electrons

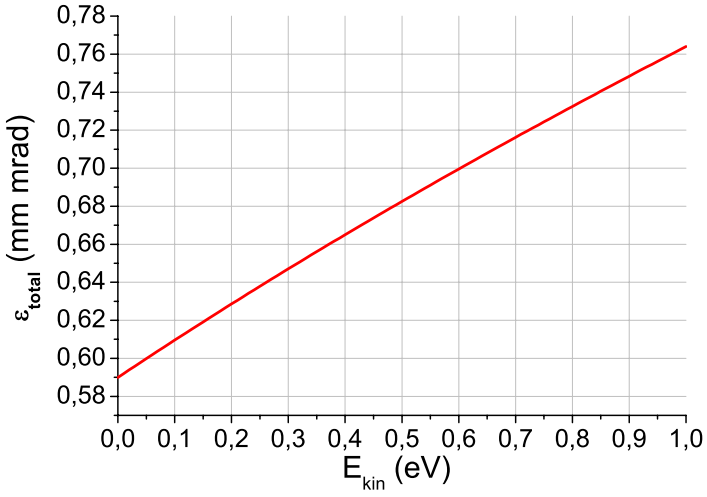

Figure D.5: *Dependence of the total transverse emittance on the initial kinetic energy of the electrons leaving the photocathode.*

is determined by the properties of the photocathode material. In section 5.1 was shown that for Cs_2Te the kinetic energy is approx. 0.55 eV. This value can be altered by surface impurities which are in general unknown.
The influence of a different initial kinetic energy on the total transverse emittance $\varepsilon_{\text{total}}$ can be roughly estimated by using equation $\varepsilon_{\text{total}} = \sqrt{\varepsilon_{\text{cath}}^2 + \varepsilon_{other}^2}$. Here, ε_{other} summarizes all contributions to the total emittance other than the cathode emittance, e.g. space charge or RF-induced emittance. As a model case, the simulation presented in the previous sub-section will be used (on-crest case). In this simulation, the total emittance was $\varepsilon_{\text{total}}$=0.69 mm mrad while the cathode emittance amounts to $\varepsilon_{\text{cath}}$=0.36 mm mrad for a circular flat-top shape of width σ_x=0.425 mm and an initial kinetic energy of 0.55 eV. Graph D.5 shows the dependence of the total transverse emittance on the initial kinetic energy for this case. The actual value of the kinetic energy is unknown. However, it is reasonable to assume that the maximum value does not exceed E_{kin}=1 eV. For this kinetic energy range, the maximal relative increase of transverse emittance is about 10 %.

Summary

In this appendix, the error sources occurring during the measurement of the transverse emittance were summarized.
Firstly, the systematic error of the measurement which amounts to 10 % at maximum.
Secondly, the measurements of the transverse emittance were compromised by RF phase fluctuations in the gun cavity. The estimation of this effect showed an increase of the transverse emittance of 29 % in the case of on-crest emission and 13 % for an emission at +6 degrees off-crest phase. This results in the fact that the actual value of the trans-

verse emittance is lower than the measured one by about 22 % and 12 % for the on-crest and off-crest phase respectively. The last uncertainty could originate from the unknown amount of cathode emittance. It was estimated that an initial kinetic energy of the emitted electrons of 1 eV instead of 0.55 eV used in the simulations leads to an increase of the total transverse emittance of 10 %. This means that the actual value is about 9.5 % lower than the measured value.
While the first and the third error source can increase and decrease the measured emittance compared to the simulated one, the phase instability can only increase the measured emittance. For this reason, the error bars are +19.5 %/-41.5 % and +19.5 %/-31.5 % for the on-crest and +6 degrees off-crest measurements, respectively.

Appendix E

Electron beam dynamics at low bunch charge

While the main subject of this thesis was the investigation of the dependence of the electron bunch properties on the laser pulse parameters at a charge level of 1 nC, this chapter is dedicated to a brief overview of the electron beam dynamics at low charge of some tens of pC. The differences in the longitudinal and transverse electron beam dynamics will be discussed separately.

Longitudinal dynamics

At high charge densities[1], the longitudinal dynamics of the electron bunch is mainly determined by three factors. Firstly, the instantaneous RF field at which each longitudinal slice is emitted defines its energy gain while being accelerated in the gun cavity. Secondly, the longitudinal space charge forces will cause an acceleration of the head and a deceleration of the tail part of the electron bunch. And finally, the mirror charge effect at the cathode influences the longitudinal dynamics at emission. In the low charge density case the second and third contributions are negligible. This behavior was simulated and is shown in figure E.1. For these simulations a maximal electric field in the gun cavity of 60 MV/m was chosen, the emission took place at phase of maximum mean momentum gain, the transverse laser shape was a circular flat-top of 1.7 mm diameter and the temporal laser shape was a flat-top with a duration of 20 ps (FWHM) and 2 ps rise and fall times.

In addition to the mentioned effects, high space charge forces cause an increase of the slice energy spread. This is in general accompanied by a reduction of modulations in the longitudinal phase space introduced by modulations in the laser pulse temporal profile

[1] Note that here the differences in charge density are discussed rather than the total bunch charge since the charge density mainly determines the electron bunch dynamics.

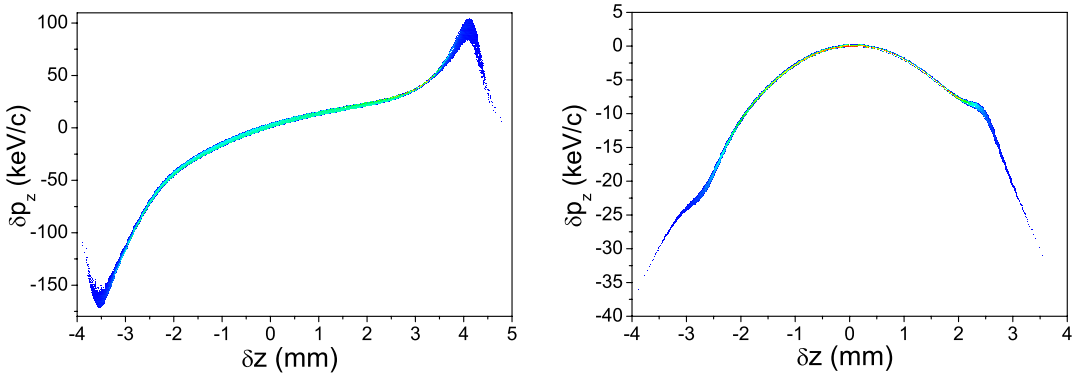

Figure E.1: *Simulated longitudinal phase space distributions downstream of the gun cavity for a bunch charge of 1 nC (left) and 20 pC (right). Except the bunch charge all simulation parameters were identical. Note the differences in the bunch length and different scales of the momentum axes. The mean momentum is about 6.84 MeV/c in both cases.*

(see chapter 7.6). This fact relaxes the requirements on the quality of the laser pulse temporal flat-top in the high charge density case. For low charge densities, these modulations remain and can cause problems due to CSR effects in the bunch compressors of an FEL [Sald01].
Finally, as mentioned in section 7.1 the choice of 20 ps laser pulse duration is a compromise between the need for low charge densities (favoring long durations) and the limited acquisition of RF field nonlinearities (favoring short durations). For low bunch charges, and therefore low charge densities, the optimum laser pulse duration is shorter.

Transverse dynamics

The optimal transverse shape was found to be a circular flat-top. The reason was the linearity of the transverse space charge forces. This finding does not change in the case of low bunch charges. On the other hand, the charge density is much smaller. This reduces the contribution of the transverse space charge to the total transverse emittance. In addition, it allows for smaller transverse laser spot sizes resulting in a reduction of the cathode emittance, see section 7.1. The dependence of the optimized transverse emittance and the corresponding laser spot size on the bunch charge were shown in simulation and experiment already in section 7.7. Further, for larger radial electron bunch dimensions the accelerating electric field might not be homogeneous anymore.
Also here, higher space charge densities can reduce modulations of the transverse electron bunch profile introduced by imperfections of the transverse laser profile.

Bibliography

[ASTRA] *http://www.desy.de/~mpyflo*

[Berg] http://www.bergoz.com , ICT-178-2-XXX-X

[Boyd] Robert W. Boyd, Nonlinear Optics, Second edition, Elsevier 2000

[Carl] B.E. Carlsten and D.T. Palmer Enhanced emittance compensation in a high-frequency RF photoinjector using RF radial focusing, NIM A, **425**, 37-50, 1999

[Chen] S. Chénais et al., Diode-pumped Yb:GGG laser: comparison with Yb:YAG, Optical Materials **22** 99-106, 2003

[Eins] A. Einstein, Zur Theorie der Strahlung, Mitteilungen der Physikalischen Gesellschaft Zürich. Nr. 18, 1916

[FEL] P. Schmüser, M. Dohlus, J. Rossbach, Ultraviolet and Soft X-Ray Free-Electron Lasers: Introduction to Physical Principles, Experimental Results, Technological Challenges, Springer Berlin Heidelberg, 2008

[Ferr01] M. Ferrario et al., Recent advances and novel ideas for high brightness electron beam production based on photo-injectors, The Physics and Application of High Brightness Electron Beams, World Scientific Publishing Co. Pte. Ltd., 2003

[Ferr02] M. Ferrario, Emittance Compensation in High Brightness RF Photoinjectors: an introduction with some application, talk at CASA seminar, Jefferson Lab, 2003

[FLASH] W. Ackermann et al., Operation of a free-electron laser from the extreme ultraviolet to the water window, Nature Photonics, Vol. 1, 336-342, 2007

[Floet] K. Flöttmann, Note on the thermal emittance of electrons emitted by Cesium Telluride photo cathodes, TESLA-FEL internal note 97-01, 1997

[Fran] P.A. Franken et al., Generation of optical harmonics, PRL **7**, No. 4, 118-119, 1961

[Goul] E. Goulielmakis et al., Single-Cycle Nonlinear Optics, Science **320**, 1614, 2008

[Haen] M. Hänel et al., Electron Bunch Momentum Distribution Modulations at PITZ, Proc. of FEL09, FEL 2009, Liverpool, UK

[Hafer] H. Haferkorn, Optik, 4^{th} edition, WILEY-VCH, 2003

[Hama01] Homepage of Hamamatsu Photonics,
http://sales.hamamatsu.com/de/produkte/system-division/ultra-fast/streak-systems/part-c6138.php

[Hama02] Homepage of Hamamatsu Photonics,
http://sales.hamamatsu.com/assets/pdf/hpspdf/Guidetostreak.pdf

[Hama03] Homepage of Hamamatsu Photonics,
http://sales.hamamatsu.com/assets/applications/ETD/pmt_handbook/pmt_handbook_complete.pdf

[Han] J.-H. Han, Dynamics of Electron Beam and Dark Current in Photocathode RF Guns
PhD thesis at PITZ, 2005

[Hodg] Norman Hodgson and Horst Weber, Optical Resonators, Fundamentals - Advanced Concepts - Applications, Springer Berlin, 1997

[Ivan01] Y. Ivanisenko, Photo Injector Cathode Laser Beam Intensity and Position Monitoring System
Master thesis at PITZ, 2007

[Ivan02] Y. Ivanisenko, Slice Emittance Measurement Using an Energy Chirped Beam in a Dispersive Section at PITZ, Proc. of FEL 2008, Gyeongju, South Korea, 2008

[Kim] K.-J. Kim, RF and Space-charge Effects in Laser-driven RF Electron Guns, NIM A **275**, 201-218, 1989

[Koech] W. Koechner, Solid-State Laser Engineering, Sixth Revised and Updated Edition, Springer, 2006

[Kras01] M. Krasilnikov, private communication

[Kras02] M. Krasilnikov, Photo injector optimization: PITZ-1.7 experience, Talk at the PITZ collaboration meeting, December 2009, Zeuthen

[Lede01] S. Lederer, private communication

[Lede02] S. Lederer et al., XPS Studies of Cs_2Te Photocathodes, Proc. of FEL 2007, Novosibirsk, Russia, 2007

[Leje] C. Lejeune and J. Aubert, Emittance and Brightness: Definitions and Measurements, Advances in Electronics and Electron Physics, Supplement 13A, Academic Press Inc., 1980

[Limb] C. Limborg-Deprey, P.R. Bolton, Optimum electron distributions or space charge dominated beams in photoinjectors, NIM A, **557**, 106-116, 2006

[Luit] O.J. Luiten et al., How to Realize Uniform Three-Dimensional Ellipsoidal Electron Bunches, Phys. Rev. Letters **93**, No. 9, 2004

[Lyot] B. Lyot, Optical apparatus with wide field using interference of polarized light, C. R. Acad. Sci. (Paris) 197, 1593, 1933

[Maim] T.H. Maiman, Stimulated optical radiation in ruby, Nature, **187**, 493-494, 1960

[MAXlab] B. Anderberg et al., The design of a 3 GHz thermionic RF-gun and energy filter for MAX-lab, NIM A **491**, 307-313, 2002

[Milt] V. Miltchev, Investigations on the transverse phase space at a photo injector for minimized emittance,
PhD thesis at PITZ, 2006

[Modi] A. Modinos, Theory of thermionic emission, Surface Science **115**, 469-400, 1982

[Mood] J.T. Moody et al., Longitudinal phase space characterization of he blow-out regime of rf photoinjector operation, PRST AB **12**, 070704, 2009

[Musu] P. Musumeci et al., Experimental Generation and Characterization of Uniformly Filled Ellipsoidal Beam Distribution, Proc. of EPAC08, Genoa, Italy, 2008

[Oppe] A. Oppelt et al., Status and first results from the upgraded PITZ facility, Proc. of FEL 2005, Stanford, USA, 2005

[PITZ01] F. Stephan et al., Photo Injector Test Facility under Construction at DESY Zeuthen, Proc. of FEL 2000, Durham, North Carolina, USA, 2000

[PITZ02] F. Stephan et al., Detailed characterization of electron sources yielding first demonstration of European X-ray Free-Electron Laser beam quality, PRST AB **13**, 020704, 2010

[Pow] R. A. Powell et al., Photoemission studies of Cesium Telluride, Phys. Rev. B **8**, 3987-3995, 1973

[Reis] M. Reiser, Theory and design of charged particle beams, Wiley Series in Beam Physics and Accelerator Technology, 1994

[Roen] J. Rönsch, Investigations on the longitudinal phase space at a photo injector, PhD thesis at PITZ, 2009

[Ros01] , J. Rossbach et al., Fundamental limitations of an X-ray FEL operation due to quantum fluctuations of undulator radiation, NIM A **393**, 152-156, 1997

[Sald01] E.L. Saldin et al., Longitudinal space charge-driven microbunching instability in the TESLA Test Facility linac, NIM A **528**, 355-359, 2004

[Sald02] E.L. Saldin et al., The physics of free electron lasers, Springer, 2000

[Scho] W. Schottky, Über die kalte und warme Elektronenentladungen, Zeitschrift für Physik A, **14** 1 63-106, 1923

[SCSS] K. Togawa et al., CeB_6 electron gun for the soft X-ray FEL project at SPring-8, NIM A **528**, 312-315, 2004

[Sera] L. Serafini and J.B. Rosenzweig, Envelope analysis of intense relativistic quasilaminar beams in rf photoinjectors: A theory of emittance compensation, Phys. Rev. E, **55**, 6, 7565-7590, 1997

[SLAC] B. McNeil, First light from hard X-ray laser, Nature Photonics, Vol. 3, 375-377, 2009

[Šolc] Ivan Šolc, Birefringent Chain Filter, J. Opt. Soc. Am., **55**, 17, 1965

[Spes01] R. Spesyvtsev, Transverse Beam Size Measurement Systems at Photo Injector Test Facility in Zeuthen
Master thesis at PITZ, 2007

[Spic] W. E. Spicer, Photoemissive, Photoconductive, and Optical Absorption Studies of Alkali-Antimony Compounds, Phys. Rev. **112**, 114-122, 1958

[Stay] L. Staykov, Characterization of the transverse phase space at the photo-injector test facility in DESY, Zeuthen site
PhD thesis at PITZ, 2008

[Suber] G. Suberlucq, Development and Production of Photo Cathodes for the CLIC Test Facility, Proc. of FEL 1996, Rome, Italy, 1996

[Tomiz] Hiromitsu Tomizawa (Spring8), private communication

[Treb] R. Trebino, Frequency resolved optical gating, the measurement of ultrashort laser pulses, Kluwer Academic publishers, Boston, Dordrecht, London, 2002

[Weis] S. Weisse et al., Tine Video System: Proceedings on Redesign, Proc. of ICALEPCS 2009, Kobe, Japan, 2009

[Will01] I. Will, G. Klemz, Generation of flat-top picosecond pulses by coherent pulse stacking in a multicrystal birefringent filter, Optics Express **16**, 19, 2008

[Will02] I. Will, G. Koss, I. Templin, The upgraded photocathode laser of the TESLA Test Facility, NIM A **541** 467-477, 2005

[Wolf] Emil Wolf (editor), Progress in Optics, Volume IX, North Holland Publishing Company, Amsterdam, London, 1971

[XFEL] M. Ferrario et al., Conceptual Design of the XFEL Photoinjector, 2001

[XTDR] M. Altarelli et al., The European X-Ray Free-Electron Laser - Technical design report, July 2007

[Yang] Yaguang Yang, Analytic Solution of Free Space Optical Beam Steering Using Risley Prisms, J. Lightwave Technol. **26**, 3576-3583, 2008

Acknowledgements

I would like to express my thankfulness to many people who contributed morally and scientifically to the success of this thesis:

Prof. Shaukat Khan, Prof. Jörg Roßbach, Dr. Frank Stephan, Dr. Jürgen Bähr and Dr. Mikhail Krasilnikov for thoroughly proof-reading my thesis and giving me useful comments and advice.

All the colleagues at PITZ who were always willing to discuss different topics related to the presented work, especially Dr. Juliane Rönsch-Schulenburg and my office mates Yevgeniy Ivanisenko, Grigorii Vashchenko and Dr. Marek Otevrel.

Furthermore, the presented results of the electron beam measurements might fit on a few pages but they required many weeks of measurements. These measurements were done on shift by the members of the PITZ group who I want to express my gratitude.

Dr. Guido Klemz for ginving me insight into the specialties of the laser system at PITZ and the long discussions about laser physics in general.

Dr. Siegfried Schreiber who always was a source of motivation and for his support during the measurements of the laser pulse properties.

All mechanical and electronic engineers, programmers and technical staff at DESY who supported me during the commissioning of new components: Hartmut Lüdecke, Gerald Koss, Jochen Bienge, Mario Pohl, Jörg Schultze, Bagrat Petrossyan, Stefan Weisse and others.

Most of all, I would like to thank my family Jana and Sontje Könnemann who supported me during the long time of creating this thesis.

Thank you all !